CHALMERS
UNIVERSITY OF TECHNOLOGY

Validating a Sea Ice Drift Retrieval Algorithm Through Remote Sensing and In-Situ Buoy Comparisons.

Master's thesis in Complex Adaptive Systems

THIBAULT DESJONQUÈRES

DEPARTMENT OF SPACE, EARTH AND ENVIRONMENT
CHALMERS UNIVERSITY OF TECHNOLOGY
Gothenburg, Sweden 2025
www.chalmers.se

Master's thesis 2025

THIBAULT DESJONQUÈRES

CHALMERS
UNIVERSITY OF TECHNOLOGY

Department of Space, Earth and Environment
Geoscience and Remote Sensing
Chalmers University of Technology
Gothenburg, Sweden 2025

THIBAULT DESJONQUÈRES

Supervisor : Leif Eriksson, professor in radar remote sensing at the Department of Space, Earth and Environment at Chalmers University of Technology, Sweden.

Co-supervisor: Malin Johannsson, associate professor in Earth Observation at the Department of Physics and Technology at The Arctic University of Norway (UiT), Norway.

Examiner: Leif Eriksson

Master's Thesis 2025
Department of Space, Earth and Environment
Geoscience and Remote Sensing
Chalmers University of Technology
SE-412 96 Gothenburg
Telephone +46 31 772 1000

Cover: Sentinel-1A image of sea ice west of Svalbard, May 30th, 07:22:07 am.

Typeset in LaTeX
Printed by Chalmers Reproservice
Gothenburg, Sweden 2025

THIBAULT DESJONQUÈRES
Department of Space, Earth and Environment
Chalmers University of Technology

Abstract

This Master's thesis validates a sea ice drift retrieval algorithm developed at Chalmers (referred to as the Chalmers algorithm) using in situ buoy data collected during the ARTofMELT 2023 cruise in the Fram Strait from May to June 2023.

The ARTofMELT 2023 expedition aimed to document melt onset in the Arctic Ocean, collecting extensive data on sea ice dynamics near the Marginal Ice Zone (MIZ) with seven OpenMETbuoys and three SIMBA buoys. These buoys were deployed on first-year ice floes, with detailed measurements of horizontal motion, rotation, deformation, wave action, and temperature. This deployment enabled analysis of ice floe movement, convergence, divergence, and the interaction between these dynamics and SAR imagery.

Low-noise Radarsat Constellation Mission (RCM) and Sentinel-1A SAR images, captured in dual polarization (HH+VV or HH+HV), were acquired to match the study area both spatially and temporally. Integrating in situ weather data, wave measurements, sea ice concentration, and weather reanalysis with satellite imagery observations of ice conditions around the buoys enabled a thorough interpretation of drift patterns, floe decay, and wave signatures associated with the buoys.

The Chalmers drift algorithm was successfully applied to two pairs of RCM images, each with a 10 m resolution, out of eight total image pairs. These pairs were chosen based on criteria including a time gap of 1-24 hours between images, identical resolution, and a maximum 5-minute time gap between the buoy and the images. The remaining six pairs contained Sentinel-1A images with a resolution of 100-150 m.

Although the drift estimates from the Chalmers algorithm were not statistically significant, they demonstrated the algorithm's capability to produce coherent and realistic drift estimates, evidenced by the alignment of drift vector azimuths with actual buoy drift and realistic sea ice drift distances. To better assess the algorithm's performance, future work should test it on a larger dataset, including the six remaining Sentinel-1A image pairs. Additionally, exploring the effects of increased time gaps between buoy and satellite images, and between the two satellite images, would provide further insights into the algorithm's capabilities.

Keywords: sea ice, sea ice drift, wave and ice interactions, remote sensing, SAR, S1A, RCM, Chalmers drift algorithm, marginal ice zone.

Acknowledgements

I would like to express my sincere gratitude to Leif Eriksson and Malin Johannsson for their exemplary supervision throughout this project. Their support enabled me to conduct my studies in Tromsø during the course of this Master's thesis, allowing me to benefit from the exceptional education provided by both Chalmers and UiT in Complex Adaptive Systems and Earth Observation. Their collaboration also permitted my establishment in Tromsø, a place I now proudly consider home, for which I am profoundly thankful. Furthermore, I am deeply appreciative of the flexibility they offered, allowing me to study and take exams remotely during challenging times with my family. Their understanding and accommodation during this period were invaluable. I was very happy to have the opportunity to benefit from their expertise in the fascinating field of sea ice remote sensing, both as teachers and supervisors. It is thanks to them that I was able to meet and engage in discussions with other researchers in the field, which greatly enriched my experience, such as at the EGU Conference 2024.

Additionally, I am immensely grateful to Denis Demchev for generously sharing his extensive Earth Observation-related programming and tools, developed throughout his distinguished research career. His high-quality sea ice data processing resources provided invaluable insights and were instrumental to this project. The field of sea ice SAR imagery processing was new to me, and these resources greatly contributed to my learning.

I would like to thank Jean Rabault (Norwegian Meteorological Institute) for his support. Working with the buoys was a lot of fun, and it was exciting to observe the extensive research opportunities enabled by these sensors, especially as I explored the topic of wave-ice interactions.

I would like to extend my sincere thanks to Tanguy Genthon for generously offering to read my Master's thesis and provide valuable feedback.

I would like to thank everyone who organized and participated in the AoM23 cruise, as well as the Swedish Polar Research Secretariat and Environment and Climate Change Canada (ECCC). I am especially grateful to Alex Komarov (ECCC) for his collaboration, which permitted the availability of the RCM data.

Thibault Desjonquères, Gothenburg, September 4, 2025.

List of Acronyms

Below is the list of acronyms that have been used throughout this thesis listed in alphabetical order:

AMSR-E	Advanced Microwave Scanning Radiometer for Earth Observing System
AoM23	Art of Melt 2023
AVHRR	Advanced Very High Resolution Radiometer
C3S	Copernicus Climate Change Service
CARRA	Copernicus Arctic Regional Reanalysis
EM	Electromagnetic
ERA	European Re-Analysis
EUMETSAT	European Organisation for the Exploitation of Meteorological Satellites
EW	Extra Wide Swath mode
FFT	Fast Fourier Transform
FYI	First Year Ice
GNSS	Global Navigation Satellite Systems
GPS	Global Positionning System
HH	Polarisation Horizontal-Horizontal
HV	Polarisation Horizontal-Vertical
IST	Ice Surface Temperature
IW	Interferometric Wide
LARA	Least Average Residual Algorithm
LIDAR	LIght Detection and Ranging
MIZ	Marginal Ice Zone
MODIS	Moderate Resolution Imaging Spectroradiometer
MYI	Multi-Year Ice
NIR	Near-infrared
NSIDC	National Snow and Ice Data Center

PRF	Pulse Repetition Frequency
PSD	Power Spectral Density
R/V	Research Vessel
RADAR	RAdio Detection And Ranging
RAR	Real Aperture Radar
RCM	Radarsat Constellation Mission
S1A	Sentinel-1A
SAR	Synthetic Aperture Radar
SIMBA	Sea Ice Mass Balance Apparatus
SSM/I	Special Sensor Microwave/Image
SSMIS	Special Sensor Microwave Imager Sound
SWIM	Surface Wave Investigation and Monitoring
VV	Polarisation Vertical-Vertical
WM	Wave Mode
WS	Weather Station

Nomenclature

Below is the nomenclature of indices, sets, parameters, and variables that have been used throughout this thesis.

Variables

$\mathbf{E}$	Electric field
ρ	Charge density
$\mathbf{B}$	Magnetic field
ε_0	Vacuum permittivity
$\mathbf{J}$	Current density
μ_0	Vacuum permeability
ε	Permittivity in matter
ε_r	Relative permittivity (dielectric constant) of the material
μ	Permeability in matter
μ_r	Relative permeability of the material
c	Speed of light in matter
p_j	Active power injection at bus j
p_{ji}	Active power flow from bus j to bus i
v_i	Square of voltage magnitude at bus i
P_r	Received power [W]
P_t	Transmitted power [W]
G_t	Transmitted antenna gain
G_{rs}	Receiving antenna gain
σ	Radar cross-section
R_t	Target-radar transmitter distance [m]
R_r	Target-radar receiver distance [m]
A_r	Effective aperture of the radar antenna [m^2]

A_{rs}	Effective receiving area of the target [m^2]
p_a	Absorption fraction
X_{az}	Azimuth resolution in RAR [m]
L	Antenna length [m]
θ	Incidence angle [°]
λ	Wavelength [m]
f, ν	Frequency [Hz]
v	Speed
x	Position [m]
y	Position [m]
u	Horizontal velocity component [m/s]
v	Vertical velocity component [m/s]
$1, 2, 3$	Indices of the buoys in the triangular grid
A	Area of the triangle spanned by buoys 1, 2, and 3 [m^2]
divergence	Rate of change of sea ice area, indicative of stretching or compression [s^{-1}]
shear	Rate of deformation due to shearing motion [s^{-1}]
Tot. deformation	Overall measure of deformation, combining divergence and shear [s^{-1}]
rotation	Rotation rate of the sea ice [s^{-1}]

Contents

List of Figures

List of Tables

1

Introduction

Sea ice plays a significant role in various fields of study and practical applications such as navigation, materials science (focusing on the relationship between the structure and properties of sea ice), climatology, meteorology, oceanography, marine biology, and offshore structural engineering [1].

From a human and societal perspective; numerous indigenous populations rely on sea ice as a mean of transportation, or as a hunting ground. Changes in sea ice extent and thickness result in indigenous populations having to change their travel routes and impact their hunting strategies. Interviews conducted in Illulissat, Greenland [2] have shown that fishermen adapt to changing sea ice conditions by, for example, fishing on boats instead of the traditional approach using dogsleds, raising concerns about the potential overexploitation of some fish species, since the use of boats increases the fishing efficiency compared to dogsleds. Another study conducted in Igloolik (Nunavut region, Canada) [3] listed different adaptive strategies employed by hunters under various sea ice changes that are to be expected to occur more frequently under climate change. For instance, if the state of the sea ice prevents access to hunting areas, hunters may adapt by hunting closer to their village. However, alternative solutions, such as having food flown in from another location, or buying food at the local store pose greater challenges for those with limited income.
In terms of infrastructure and maritime activities, offshore constructions and ships are particularly vulnerable to sea ice forcing [4]. Maritime shipping in the Arctic has been observed to increase along with the retreat and thinning of sea ice [5]. Furthermore, it is anticipated that the opening of the Northwest Passage and Northern Sea Route will lead to a surge in maritime traffic in the Arctic [6].

From a broad climate perspective; the thermal and optical properties of sea ice impact the ocean atmosphere exchanges of heat and gas. Thick sea ice restricts these exchanges, whereas melting and the breakup of sea ice creates regions of open water, enhancing heat and gas transfers [7]. Sea ice is highly influential in the atmospheric circulation, which is driven by the temperature gradient between the ocean and the atmosphere. Sea ice also affects the thermohaline circulation, as freezing and thawing modify the vertical density gradient [8]. In terms of biological aspect, sea ice serves as a habitat for numerous biological organisms [9]. Arctic sea ice is the habitat for species of planktons, which are the base of the Arctic food chain. The thinning and the earlier retreat of the sea ice affects the timing and the amount of primary production [10]. Phytoplankton bloom have been reported to occur earlier, and to be more intense, which has consequences on the higher trophic levels [11].

More specifically, regarding sea ice drift and waves/sea ice interactions; sea ice is a highly dynamic material, it is constantly drifting and changing. At the regional scale, Arctic sea ice drift patterns are as follows: ice circulates within the Beaufort Sea Gyre and is mainly transported out of the Arctic through the Fram Strait by the Transpolar Drift Stream [12]. The Fram Strait is the main gateway for sea ice export, with an area of 800 km^2. The mean yearly sea ice exports through the Fram Strait have been reported to reach 2,400±640 km^3 [13]. Furthermore, it was estimated that 90% of the export of Arctic sea ice occurs through the Fram Strait [14]. Since 1979, there has been a consistent decline in the extent of pan-Arctic sea ice throughout the year [15], and the mean sea ice drift speed has been reported to have substantially increased as a result of thinning ice cover. Furthermore, thinner sea ice has a weaker material strength [16], therefore sea ice breaks up more easily by the action of the wind and the waves [17]. The increase of the extent of the open water areas at the edge of the sea ice allows greater fetch, allowing the formation of larger waves, breaking more sea ice [18].

Given the importance of sea ice, and its rapid evolution in the context of climate change, understanding and modelling sea ice accurately is crucial to improve climate models, scientific mission planning, climate adaptation policies for indigenous populations and maritime traffic safety. Particularly, this justifies the need for investigating sea ice drift, and waves/sea ice interactions, given that sea ice drifts faster, becomes thinner, with a weaker material strength, and diminishes in extent. Elaborating sea ice motion algorithms by applying image processing and computer vision methods to satellite images in the visible, infrared, and microwave ranges presents a valuable solution to this challenge. Today, there exist several sea ice motion products derived from satellite imagery. This comparative study [19] presents eleven such products that utilize various computer vision methods and various individual sensors or combinations of sensors including; passive microwave radiometers, optical sensors, active microwave scatterometers, and Synthetic-Aperture Radar (SAR). Drift products differ in spatial and temporal resolution, which is inherent to the sensor and the data processing methodology.

The aim of this Master's thesis is to validate and enhance a sea ice drift algorithm developed at Chalmers University of Technology, in Sweden [20] (referred to as the Chalmers algorithm in this work). It relies on the analysis of subsequent high resolution SAR satellite images. The validation process leverages in situ sea ice dynamics data collected by ten buoys (seven OpenMET [21], three SIMBA [22]) deployed on four ice floes in the Fram Strait (see Figure 3.1), during the ArtOfMelt 2023 (AoM23) expedition in May-June 2023. These buoys measure sea ice drift speed and direction, which are then compared with those derived from the Chalmers algorithm using SAR data collected during the cruise from the Radarsat Constellation Mission (RCM) and Sentinel-1A (S1A). In addition to providing sea ice drift speed and direction measurement, the OpenMET buoys measures wave spectra, which helps in quantifying the wave action against the ice floe, and describing the state of the ice floe as it drifts.

2

Theory

2.1 Basics of electromagnetic waves theory

Electromagnetic (EM) waves serve as the conduit through which information is transmitted from a target to the sensor in remote sensing applications. In vacuum, EM waves propagate at the speed of light. EM waves are characterised by their wavelength (or frequency), phase, intensity, and polarization. The polarization of an EM wave describes how it oscillates with respect to its direction of motion. Radiations can be unpolarized, partially polarized, linearly polarized, circularly polarized, or elliptically polarized. If a radiation does not have a clearly defined polarization, like the sun, it is said to be unpolarized. The EM spectrum spans over a wide range of wavelengths, with those between the gamma and radio ranges represented in Table 2.1.

Table 2.1: The EM spectrum, presented in frequency and wavelength.

Band	Spectral range	Wavelength	Frequency
Gamma rays		<0.01 nm	>30 EHz
X-rays		0.01 nm - 10 nm	30 PHz - 30 EHz
UV		10 nm - 400 nm	750 THz - 30 PHz
Visible Light		400 nm - 780 nm	385 THz - 750 THz
Near Infrared		750 nm - 1.4 µm	214 THz - 400 THz
Short Wavelength Infrared		1.4 µm - 3 µm	100 THz - 214 THz
Mid Wavelength Infrared		3 µm - 30 µm	10 THz - 100 THz
Thermal Infrared		8 µm - 1 mm	0.3 THz - 37.5 THz
Microwave	**L-band**	15 cm - 30 cm	1 GHz - 2 GHz
	C-band	3.75 cm - 7.5 cm	4 GHz - 8 GHz
	X-band	2.5 cm - 3.75 cm	8 GHz - 12 GHz
	Ku-band	1.67 cm - 2.5 cm	12 GHz - 18 GHz
	K-band	1.11 cm - 1.67 cm	18 GHz - 26.5 GHz
Radio waves		>30 cm	<1 GHz

EM waves propagate in vacuum according to Maxwell's equations (Equations 2.1 to 2.4) [23].

$$\nabla \cdot \mathbf{E} = \frac{\rho}{\varepsilon_0} \quad \text{Electric charges create an electric field.} \tag{2.1}$$

$$\nabla \cdot \mathbf{B} = 0 \quad \text{There are no magnetic monopoles.} \tag{2.2}$$

$$\nabla \times \mathbf{E} = -\frac{\partial \mathbf{B}}{\partial t} \quad \text{A changing magnetic field induces an electric field.} \tag{2.3}$$

$$\nabla \times \mathbf{B} = \mu_0 \mathbf{J} + \mu_0 \varepsilon_0 \frac{\partial \mathbf{E}}{\partial t} \quad \text{Changing electric fields and currents induce magnetic fields.} \tag{2.4}$$

Where:

$\mathbf{E}$: Electric field	ρ : Charge density
$\mathbf{B}$: Magnetic field	ε_0 : Vacuum permittivity
$\mathbf{J}$: Current density	μ_0 : Vacuum permeability
t : Time	

An electric field is generated by charged particles. The charge density is the number of charges per unit volume, area, or length. A magnetic field is generated by the motion of charged particles. The current density describes the flux of charged particles.

To describe the propagation of EM waves in matter, Maxwell's equations must be adjusted using the material's permittivity and permeability as described in Equations 2.5 to 2.7 [23].

$$\varepsilon = \varepsilon_0 \varepsilon_r \tag{2.5}$$

$$\mu = \mu_0 \mu_r \tag{2.6}$$

$$c = \frac{1}{\sqrt{\varepsilon \mu}} \tag{2.7}$$

Where:

ε : Permittivity in matter	ε_r : Relative permittivity (dielectric constant)
μ : Permeability in matter	of the material
c : Speed of light in matter	μ_r : Relative permeability of the material

Relative permeability quantifies the amount of magnetization that occurs in a material when subjected to a magnetic field. Relative permittivity is a measure of the amount of polarization that occurs in a material when subjected to an electric field. Both quantities are relative to vacuum. The higher the relative permittivity of a medium, the more attenuation occurs when an EM wave penetrates the medium. Therefore, a medium with high relative permittivity is termed a lossy medium. Each surface terrain feature has unique spectral properties, and when EM waves interact with matter, they produce a distinct spectral signature as a result of this interaction.

This allows for the detection and analysis of remote targets from satellites, like sea ice.

The nature of the wave/matter interaction depends on the wavelength of the radiation. At the microwave and infrared bands, interactions occur at the molecular level. At the visible and ultra-violet bands, interactions occur at the electronic energy level.

EM radiation interacts with matter by absorption, reflection and transmission. Absorption is the process by which incident radiation is converted to another form of energy (often heat) as it interacts with matter. Reflection is the process by which incident unidirectional EM radiation is reflected at the boundary between two different media. Transmission is the process by which an incident EM radiation passes through a medium. Scattering occurs during absorption and transmission. Along the dielectric properties of the material, the surface roughness is a key factor in scattering. The roughness of a surface is defined relatively to the wavelength of the incident radiation. If the fine features at the surface are much smaller than the wavelength, the surface is said to be smooth. In the opposite case, the surface is said to be rough.

An incident EM radiation can be scattered by a surface by surface scattering, volume scattering, and double bounce, depending on the surface dielectric constant, the surface roughness, the incidence angle, and the radiation wavelength. On a smooth surface, specular reflection occurs; the incident radiation is reflected away from the satellite, like a mirror, and the surface has a low backscatter value. If the surface is slightly rough, the scattering has a specular (coherent, i.e., in phase) and a diffuse (incoherent) component. In this case, the backscatter value of the surface is dependent on the incident angle and the viewing angle, as for a very rough surface, where the scattering is completely diffuse. Volume scattering can occur as an incident radiation is transmitted through another medium. A portion of the scattered radiation can be sent back toward the medium it originated from. Double bounce occurs when an incident EM radiation is reflected against two smooth, almost orthogonal surfaces. Double bounce occurs, for example, on wet soil and tree trunks or on human-made structures like roads and buildings.

The penetration depth of a an incident EM wave into a medium depends on the medium's dielectric constant and porosity and on the wavelength of the radiation. The penetrating depth of the EM waves is inversely proportional to their frequency [24], therefore, longwave radiation penetrates deeper into materials [25].

2.2 Remote Sensing

Remote sensing methods provide numerous valuable benefits for studying sea ice, surmounting the challenges posed by its remote location and harsh weather conditions in the polar regions. Sensors function within various ranges of the EM spectrum, including optical, infrared, and passive and active microwave bands, each exploiting distinct EM radiation/matter interaction properties, thus permitting the detection of various surfaces and inferring surface characteristics.

Specific remote sensing terminology must be introduced to clarify the concepts related to the topic. The range direction is the direction orthogonal to the satellite's trajectory. The azimuth direction is the direction along the trajectory of the satellite. The incidence angle is the angle between the incoming radar beam and the normal to the target being sensed. Satellites can be side-looking or nadir-looking, meaning that measurements are carried out on one side of the satellite, or right below it. On a side-looking satellite, the slant range refers to the distance between the satellite and the target. The viewing geometry of a side-looking radar is illustrated in Figure 2.1. The orbit of a satellite describes the way in which it revolves around Earth. The orbit type depends on the altitude of the satellite from Earth's surface, and it's trajectory inclination relative to the equator. Different orbits can serve different purposes. For example, polar orbiting satellites pass over the poles of Earth. As the Earth revolves around itself at the same time, it allows for a global satellite coverage which is ideal for Earth observation applications, such as sea ice remote sensing. The swath of a satellite is the area that the satellite senses. The temporal resolution refers to the temporal frequency at which a satellite can repeat a measurement. The spatial resolution refers to the level of clarity of a satellite image (e.g., how many meters are resolved in each pixels of the image) that is obtained from a sensor mounted on the satellite.

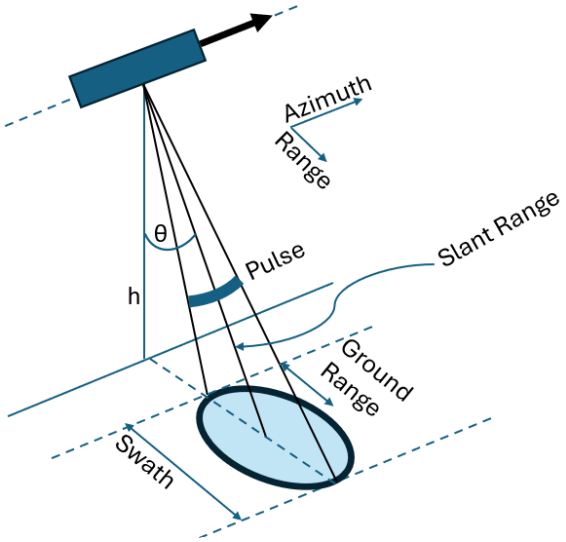

Figure 2.1: Viewing geometry of a side-looking radar.

Remote sensing sensors can be categorized as passive and active. In passive remote sensing, the radiation measured by the satellite originates from an external source (e.g. solar radiation). Passive sensors include optical sensors, thermal infrared sensors, and passive microwave radiometers. Passive microwave radiometers are characterized by a high temporal resolution and a low spatial resolution. For sea ice remote sensing, such technical features are particularly useful in applications where the fine features of the sea ice do not need to be resolved and where

frequent measurements are necessary, such as for the measurement of the sea ice concentration in the pan-Arctic region. Daily sea ice concentration maps [26] are for example delivered from the combination of data collected by the passive Advanced Microwave Scanning Radiometer - 2 (AMSR2) with a low resolution of 5x5 km (for the 89 GHz band) which is installed on the Global Change Observation Mission - Water 1 (GCOM-W1) satellite [26], and the thermal infrared sensor Moderate Resolution Imaging Spectroradiometer (MODIS) with a low spatial resolution of 1x1 km, mounted on the Aqua satellite [27]. The two satellites have a temporal resolution of 1-2 days.

In active remote sensing, the satellite emits a pulse and the sensor measures the back-scattered radiation. Active remote sensing methods include LIght Detection And Ranging (LIDAR) and RAdio Detection And Ranging (RADAR), in the optical and radio range respectively.

There exist various kinds of radars :

- Real Aperture Radar (RAR).
- Synthetic Aperture Radar (SAR) : used to provide high resolution imagery locally and regionally, as they are caracterized by a swath widh of 30 to 500 km and a spatial resolution of 1 m to 1 km [28]. SAR can for example measure ocean waves direction [29], and sea ice drift [30]. Side-looking.
- Radar Altimeter : used in sea ice thickness measurements [31], measures ocean's circulation [32], waves height and wind speed over oceans [33]. Nadir-looking.
- Radar Scatterometer : used to identify ice types [34], measure sea ice motion [35], measured the wind speed and direction over the ocean surface with high precision [36]. Side-looking.
- Radar Interferometry : used to measure the stability of sea ice [37], or sea ice surface topography [38]. Side-looking.

In the context of sea ice drift, drift products are often derived from single sensors or from combinations of sensors with different resolutions and/or ranges. These sensor combinations include, for example, passive microwave sensors, optical sensors, active microwave scatterometers, and SAR. Local high resolution images provided by SAR can be used to validate global drift estimates from low resolution sensors [39]. Moreover, an important factor in remote sensing is the atmospheric opacity, which varies with wavelength, as represented in Figure 2.2, along with typical ranges for active and passive remote sensing. The atmosphere alters radiation in the visible, and infrared ranges, but not in the microwave range. This makes radars convenient for remote sensing applications in the polar regions and is another motivation for sensor fusion. An example of a drift product derived from optical and passive microwave sensors combination is the Polar Pathfinder Daily 25 km EASE-Grid Sea Ice Motion Vectors product developed by the National Snow and Ice Data Center (NSIDC) [40].

It is based on the merging of Advanced Very High Resolution Radiometer (AVHRR) visible and thermal data with passive microwave data from Advanced Microwave Scanning Radiometer for Earth Observing Systems (AMSR-E), Scanning Multichannel Microwave Radiometer (SSMR), Special Sensor Microwave/Imager (SSM/I) and Special Sensor Microwave Imager Sounder (SSMIS). An example of a drift product derived from the Advanced SCATterometer (ASCAT) and passive microwave sensors (SSMIS, AMSR2) combination is the *low resolution sea ice drift product* of the EUMETSAT *Ocean and Sea Ice Satellite Application Facility* [41], with a resolution of 62.5 km. The properties of the sea ice change drastically in the microwave range during the melting season. Thus, drift products that use passive microwave data are only available before the start of the melting season. The *Global High Resolution SAR Sea Ice Drift Product* [42] provided by Copernicus is derived from SAR sensors (Sentinel 1-A and RADARSAT-2), and has a resolution of 10x10 km. High resolution ice drift estimates require the use of SAR to resolve for the individual floes and estimate their displacement. The temporal resolution must be such that the floes have not been too deformed at the risk of not being identifiable from one image to the next and that the floes are still present in the overlap region of the two images used for the drift estimation. A typical temporal resolution respecting those two conditions ranges from a few hours to a few days.

The following subsection focuses on describing RAR and SAR.

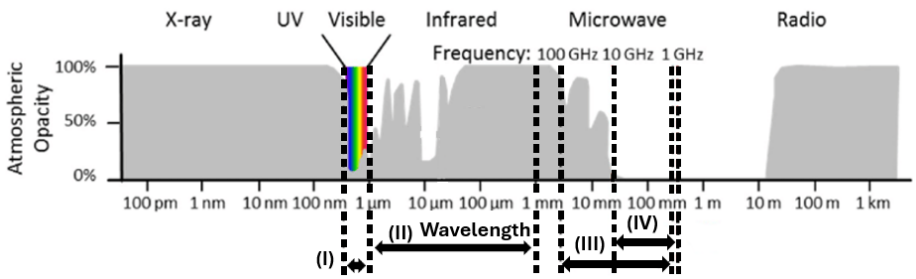

Figure 2.2: The EM spectrum, from X-rays to Radio waves. At 100% atmospheric opacity, a satellite sensor would not receive signals from Earth's surface at the respective wavelength. Examples of spectral domains used in remote sensing applications are indicated; (I) the visible range, (II) the infrared range, (III) the passive microwave sensors range, (IV) the active microwave sensors range. (Figure adapted from [43]).

2.2.1 Working principles of RAR and SAR

Imaging radar systems transmit several coherent pulses in the form of a chirp; the pulse's frequency is linearly modulated over time. The carrier frequency (often measured in GHz) refers to the central frequency of the chirp signal, while the bandwidth (typically a few MHz-wide) represents the range of frequencies covered by the chirp. Every chirp is separated by a waiting time to process the received backscatter, and a typical Pulse Repetition Frequency (PRF) can be of the order of

several kilohertz (kHz) to several megahertz (MHz). RAR and SAR measurements must be carried out on side-looking satellite, otherwise, there would be ambiguities between chirps emitted on either sides on the satellite. As the pulse sweeps across the swath, it scatters on the Earth's surface, and the antenna receives a portion of the backscattered signal. The power (Pr) of the received signal is linked to the power of the transmitted signal (Pt) by Equation 2.8, known as "the radar equation":

$$P_r = \left(\frac{P_t}{4\pi R_t^2} G_t\right) \sigma \left(\frac{1}{4\pi R_r^2} A_r\right) \qquad \sigma = A_{rs}(1 - p_a) G_{rs} \tag{2.8}$$

Where:

P_r = Received power [W]
P_t = Transmitted power [W]
G_t = Transmitted antenna gain
G_{rs} = Receiving antenna gain
R_t = Target-radar transmitter distance [m]
R_r = Target-radar receiver distance [m]
A_r = Effective aperture of the radar antenna [m^2]
A_{rs} = Effective receiving area of the target [m^2]
σ = Radar cross-section
p_a = Absorption fraction

From the sensor's perspective, the brightness of features depends on the polarization of the pulse, the frequency of the pulse, the incidence angle, the resolution, and the noise of the sensor. From the target's perspective, it is a combination of the surface roughness of the target, the surface geometry, and the electrical properties of the target.
In a RAR, the azimuth resolution X_{az} [m] is a function of the antenna length L [m], the beam range-width h, the wavelength λ [m], and the incidence angle θ [°] as described in Equation 2.9 :

$$X_{az} = \frac{h \cdot \lambda}{cos(\theta) \cdot L} \tag{2.9}$$

With antenna where $L = 10\,\text{m}$, $\theta = 30°$, $\lambda = 5\,\text{cm}$ (C-band), and $h = 750$ km, the azimuth resolution would be about 4.3 km. With such an antenna, achieving an azimuth resolution of $X_{az} = 100\,\text{m}$ would require using an antenna 433 m long, which would be unrealistic. Therefore, RAR have technical limitations for improving the azimuth resolution, and their use is restricted to the acquisition of low-resolution images. SAR overcomes this issue by combining all pulses reaching a target as the satellite passes above it. The term "synthetic aperture" refers to the fact that the surface is not sensed instantly while it is in the field of view of the satellite, but it is a combination of successive measurements made only very slightly staggered in time as the pulse travels at the speed of light, and the characteristic satellite speed is of about 10 km/s. The viewing geometry and the working principle of SAR are illustrated in Figure 2.3.

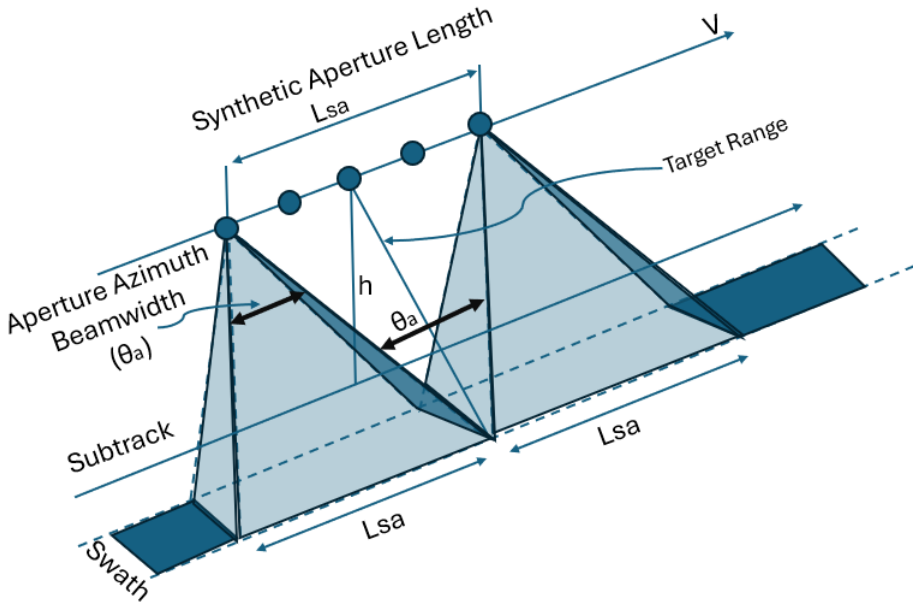

Figure 2.3: Working principle of SAR. As the satellite moves over the target, it senses it several times (indicated by the 5 points along the synthetic aperture length).

2.3 Sea ice

Sea ice is a highly dynamic and complex material; its formation can follow multiple pathways according to environmental conditions, it is subjected to multiple forcing from neighboring floes, the atmosphere, the ocean and is often covered with snow, therefore affecting the thermodynamics of the ice and its spectral signature when measured from space. In addition, seasonal variations and the aging of sea ice also continuously affect its physical properties. Therefore, remote sensing of sea ice requires extensive knowledge of its properties and their seasonal variations over time, from formation to aging and melting. Furthermore, global decadal sea ice trends derived from satellite measurements since the start of the Earth observation era in the 1970s are available and can be used to analyze its historical trends and predict future changes in sea ice. This section describes sea ice formation, its seasonal variation, and long-term trends to explain its physics in relation to remote sensing.

2.3.1 Formation and evolution

Sea ice **formation** in the Arctic starts in the late Autumn, referred to as the freezing season. The formation processes depend on the conditions of the ocean. Under quiet conditions, at the initial stage of sea ice formation, the water freezes into weak small ice crystals known as frazil ice. Under persistent freezing conditions, frazil crystals form a thin sheet of young ice, called nilas when it is at its earliest growth stage; it is only a few centimeters thick, it bends and breaks easily under the swell action and it is transparent. As it thickens, it progressively turns grey, and then white. Under windy and turbulent ocean surface conditions, the frazil crystals do not turn into nilas; instead, the constant mixing of the ocean surface maintains the frazil crystals, and as more freezing and mixing occurs, the density frazil crystals

occur, and the cyclic compression of frazil crystals leads to the formation of grease ice; a soupy layer of frazil ice crystals making the ocean surface resemble an oil slick. which progressively leads to the formation of pancakes of ice. Further accretion of frazil crystals onto those cakes makes them grow in diameter. Their round aspect results from the collisions between the individual ice pancakes. Sea ice can be categorized into landfast ice, which is fastened to the land and does not drift, and pack ice, which drifts with winds and ocean currents.

Sea ice **growth** starts when nilas and pancakes ice can no longer grow horizontally and instead grow vertically. Sea ice grows downward; it is cooled down at the surface by the atmosphere, and sea water freezes at the bottom. As sea ice thickens, the ice/ocean interface gets more insulated from the atmospheric cooling. The vertical growth through this process is limited to the point where the atmosphere can no longer remove heat through the vertical ice column. Initially, sea ice thickens and forms Young Ice (at most 15 cm thick), and eventually form First Year Ice (FYI). FYI designates ice that has not grown for more than one winter season. Ice that has survived from one winter season to the next is called Multi-Year Ice (MYI). The freezing process bonds the water molecules together, enclosing air and liquid brine (highly salty water) within a matrix of pure ice crystals, forming brine pockets. These pockets can be interconnected, forming brine channels, that contract and expand as the ice temperature decreases and increases respectively. Sea ice is often covered by snow. In the freezing season, when the snow is dry, it is characterized by a high albedo, as oppososed to when it is wet. The albedo of a surface describes its reflectivity. It is comprised between 0 (full absorption) and 1 (full reflection). Generally, the albedo of FYI is around 0.4-0.6. The albedo of dry snow is around 0.8-0.9, meaning that sea ice covered with a thick layer of dry snow absorbs very little radiation from the Sun. Water, on the other hand has an albedo close to 0 [44].

Two geophysical forces induce sea ice **motion and deformation**; wind and ocean currents. The range of mechanical deformations that sea ice undergoes includes breaking, shearing, divergence, melting, and rotation. Divergence within the sea ice cover can result in the creation of leads; wide linear openings of the ice sheet that may extend up to hundreds of kilometers, while convergence can lead to the formation of ridges; high and chaotic linear accumulations of pilled up ice.

The **evolution** of sea ice under climate change has been monitored globally since 1972, the year of the launch of the Nimbus-5 satellite, equipped with a passive microwave sensor [45]. Since 1979, the extent of Arctic sea ice has decreased every month, and sea ice freezing has been delayed [46]. Satellites records have shown that 30% of the Arctic MYI had disappeared within 30 years (from approximately 75% in the mid 1980s to 45% in 2011) [47]. Replacement of MYI by thinner FYI combined with changes in wind forcing results in an increase in the average drift speed in the Arctic by about 10.6% from 1992 to 2009 [16]. Satellite records from 1979 have shown that the extent of the melt season increased by approximately 20 days from 1989 to 2009 [48].

2.3.2 Seasonal changes and aging

The **melt** of sea ice is influenced by the combined action of the absorbed solar radiation and the heat convected by the air [49] [Section 1.5.5 : Sea Ice Melt, 2017 edition]. The melt season in the Arctic starts in May/June, a positive feedback is triggered; the first snow patches that start to melt are the thinnest ones. The wet snow and the exposed ice surface having a lower albedo compared to that of snow in a less advanced melt stage, they absorb more solar radiation, and turn into melt ponds, absorbing even more radiation, increasing the local surface temperature, which results in further melt. As the melt continues, the sea ice surface topography becomes more heterogeneous with low areas formed by the melt ponds and high areas formed by the remaining snow covered ice patches. Horizontal melt channels form from the ice and snow patches towards the melt ponds, further ablating the surface, and making the sea ice look like giants spiders, progressively making the dark melt ponds appearing as the body, and the melt channels as the legs [1] [section 2.5.1 "Ice Decay"]. During the melt season, the formation of thaw holes, the water saturated snow cover and ice surface, and the melt ponds drastically changes the visual appearance of the sea ice compared to during the freezing season, where the dry snow is relatively bright and homogeneous.

During the melt season, the snow becomes saturated with liquid water which eventually percolates down to the ice surface. As melt water flows over the surface of the ice, drains through the pores of the sea ice, the brine trapped within the ice is washed away. This process is called brine flushing. The meltwater can eventually be drained to the sea through cracks and thaw holes. When some melt occurs during an episodic warm event during freezing season, or at early stages of the melt season, the meltwater may percolate through the snow and refreeze at the snow and ice interface. This layer of refrozen meltwater, called superimposed ice [50], may disappear later over the melt season, or survive until the next season, and contribute positively to the sea ice mass balance.

As ice **ages**, its physical properties change. MYI is characterized by being generally thicker, less saline, having more numerous and bigger air inclusions, and a greater mechanical strength than FYI, as demonstrated by this comparative study, where 1300 borehole measurements were realised on FYI, Second-Year Ice (SYI) and (MYI) in the Canadian Arctic over 15 years [51]. The greater thickness of MYI is due to its longevity. The lower salinity displayed by MYI is explained by two primary mechanisms; the aforementioned brine flushing, and gravity drainage. Gravity drainage designates the expulsion of the dense brine from the ice under the action of gravity. The more numerous air inclusions in MYI compared to FYI result from the remains of the water drain channels emptied throughout the successive melt seasons [52]. Salinity and air inclusions in the ice are key parameters in sea ice remote sensing, has salt has a very high permittivity and inclusions modify the scattering mechanisms of EM waves with the ice, as discussed in the following subsection. More generally, the mechanisms by which the numerous changes sea ice undergoes seasonally and with aging modify its physical properties and the sea ice/EM waves interactions are discussed.

2.3.3 Scattering mechanisms

The sea ice parameters affecting the SAR image are salinity, temperature, wetness, surface roughness, subsurface porosity, inclusions, and the snow cover. This subsection aims to describe the EM wave/sea ice interactions in relation to each of these parameters, and their evolution in the context of the seasonal variations and the aging of the ice.

Salt controls the average dielectric constant of sea ice, over the contributions from its ice and air fractions, as salt has a much higher permittivity. The permittivity of the ice is one of the drivers of the penetration depth of an incident EM wave into the ice, along with the incidence angle, the temperature and the wavelength of the EM wave. The penetration depth describes where in a volume, scattering is likely to occur. A higher permittivity implies a smaller penetration of the pulse into the sea ice [18] as shown in Figure 2.4, and more surface scattering. Therefore, under stable conditions as in the middle of the freezing season, the distinct backscatter resulting from the difference in salinity between FYI and MYI with various incidence angles and frequency can be utilized to discriminate between these two ice types using the X-band, C-band or L-band for example. Water also has a very high permittivity, thus preventing sea ice discrimination during the melt season.

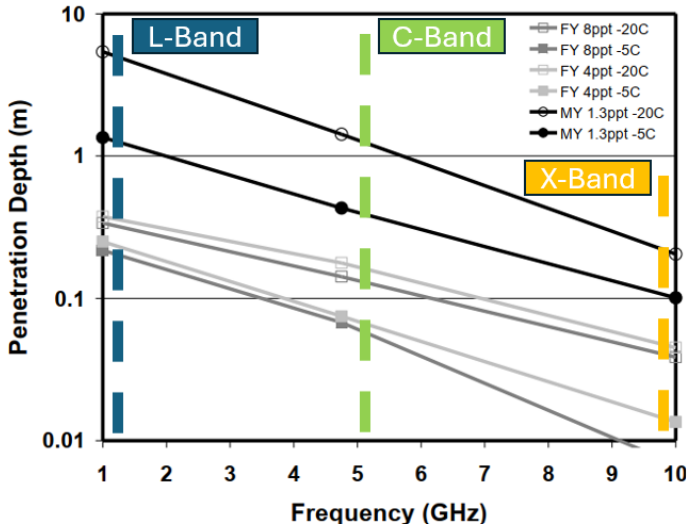

Figure 2.4: Penetration depth [m] vs. frequency for MYI and FYI (L/C/X-Bands added to the original figure). Generally, MYI have a lower salinity compared to FYI. Therefore, more volume scattering, and the beam penetrates deeper into MYI, compared with FYI. Figure adapted from [53]

The **porosity** of the sea ice is determined by the amount of brine inclusions and air bubbles. Three types of inclusions coexist within the ice, air, brine, and solid salt that precipitated inside the brine pockets, causing incident EM waves that penetrate the sea ice to undergo volume scattering [53].

The **surface roughness** impacts the sea ice SAR backscatters. On smooth surfaces

such as on the ocean surface or on a smooth FYI surface, smooth surface scattering (specular reflection) occurs. Almost vertical surfaces can be formed at the MYI and FYI boundary, and at the open ocean and FYI boundary, the smoothness on the surfaces gives rise to double bounce scattering onto the surface and the vertical delimitation. On a slightly rough surface, less diffuse scattering occurs. On a rough sea ice surface, like on a ridge, diffuse surface scattering occurs. Figure 2.5 illustrates how surface roughness impacts the sea ice SAR backscatter, as well as the aforementioned salinity effect on the backscatter and penetration of the beam into MYI, FYI and open water.

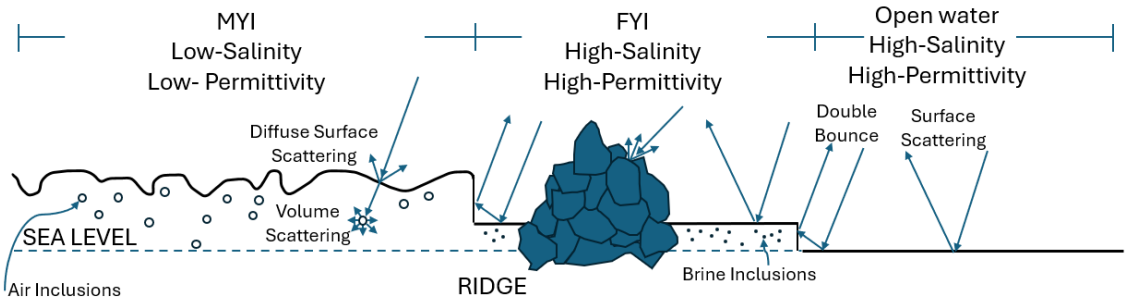

Figure 2.5: Scheme of the scattering mechanisms on FYI and MYI and open water. The MYI features numerous air inclusions, while the FYI features more brine inclusions.

The **snow cover** also plays a major role in the scattering mechanisms. Snow is a porous material made of ice and air. Its thermal and optical properties are highly unstable, as snow is permanently subjected to metamorphism, which modifies its macro-physical properties, such as density and grain size which will impact the scattering mechanisms [54]. The amount of moisture contained in the snow will also affect the scattering mechanism, as water has a high dielectric constant. Dry snow is essentially invisible to frequencies below 10 GHz and, therefore, ice can be detected in such conditions. When snow melts, its moisture content increases, thus producing more surface scattering with incident EM waves. The formation of melt ponds and thaw holes produce specular reflection similar to that on a calm ocean surface. Thus, the formation of thaw holes and melt ponds prevent the ice/ocean discrimination, and the increased wetness of the snow and ice complicates the retrieval of the properties of sea ice from remote sensing.

To conclude, the **seasonal variation** of sea ice and its **aging** affects its physical properties, and modifies the SAR signature of all types of sea ice. A figure illustrating the variation of the radar cross-section of sea ice versus the incidence angle of FYI and MYI in the C-band, in HH polarization, in the freezing season and in the melt season can be found in [53] (Figure 2.3). It shows that generally, the cross-section of FYI and MYI varies significantly from 3° and above, and that in the winter season, FYI has a greater cross-section than MYI, while the opposite occurs in the melt season.

2.3.4 Sea Ice kinematics

Sea ice can deform through various mechanisms such as rigid movement, bending and flexing, stretching and shearing, divergence and convergence, as well as plastic, elastic, and viscous flows [55]. The equations of sea ice kinematics are presented in Equations 2.10 to 2.17 [56]:

$$\frac{du}{dx} = \frac{1}{2A}\left[(u_1+u_3)(y_1-y_3)+(u_1+u_2)(y_1-y_2)+(u_2+u_3)(y_2-y_3)\right] \tag{2.10}$$

$$\frac{du}{dy} = -\frac{1}{2A}\left[(u_1+u_3)(x_1-x_3)+(u_1+u_2)(x_1-x_2)+(u_2+u_3)(x_2-x_3)\right] \tag{2.11}$$

$$\frac{dv}{dx} = \frac{1}{2A}\left[(v_1+v_3)(y_1-y_3)+(v_1+v_2)(y_1-y_2)+(v_2+v_3)(y_2-y_3)\right] \tag{2.12}$$

$$\frac{dv}{dy} = -\frac{1}{2A}\left[(v_1+v_3)(x_1-x_3)+(v_1+v_2)(x_1-x_2)+(v_2+v_3)(x_2-x_3)\right] \tag{2.13}$$

$$\text{divergence rate} = \frac{du}{dx}+\frac{dv}{dy} \tag{2.14}$$

$$\text{shear rate} = \sqrt{\left(\frac{du}{dx}-\frac{dv}{dy}\right)^2+\left(\frac{du}{dy}+\frac{dv}{dx}\right)^2} \tag{2.15}$$

$$\text{Tot. deformation rate} = \sqrt{\text{divergence}^2+\text{shear}^2} \tag{2.16}$$

$$\text{rotation} = \frac{dv}{dx}-\frac{du}{dy} \tag{2.17}$$

Where:

- x and y [m]: Horizontal and vertical position.
- u and v [m.s^{-1}]: Velocity components in the horizontal and vertical directions, respectively.
- $1, 2, 3$: Indices of the buoys in the triangular grid.
- A [m^2]: Area of the triangle spanned by buoys 1, 2, and 3.
- divergence rate [s^{-1}]: Measure of the rate at which the sea ice area changes, indicative of stretching or compression.
- shear rate [s^{-1}]: Measure of the rate of deformation due to shearing motion.
- Tot. deformation rate [s^{-1}]: Overall measure of deformation, combining divergence and shear.
- rotation [s^{-1}]: Measure of the rotation rate of the sea ice.

2.4 Waves and sea ice Interactions

The long trend changes that sea ice undergoes in the context of climate change described in Section 2.3; the thinning and retreat of the sea ice cover, as well as the replacement of MYI by FYI which features reduced material strength, alter the wave/sea ice interactions by forming bigger fetch areas (i.e., open ocean areas where the wind can form waves). Consequently, higher-amplitude waves are formed, strengthening the wave/ice interactions. Research in the wave/ice interactions domain aims to describe how the various types of sea ice are affected by potentially stronger waves. Rather than presenting the theoretical background of ocean waves interactions with sea ice, which can be found in this recent review of the topic [57], this section aims to describe these interactions from a practical perspective, in two parts. First, the wave/ice interactions in the Marginal Ice Zone (MIZ) is described, as it is the region of sea ice where the strongest interactions occur, and to motivates why research in this field heavily relies on remote sensing and in situ measurements. Second, an overview of the current research in this domain using buoys and satellite remote sensing is presented.

2.4.1 Marginal Ice Zone

On the local scale, the dynamics of sea ice can be classified by the concentration of sea ice and its proximity to open water. The sea ice concentration is defined as a percentage of ice in a given ocean area. The sea ice that covers the majority of the Arctic ocean is pack ice; ice that drifts with ocean currents and wind, as opposed to landfast ice. The extremity of the pack ice, also called sea ice edge is characterized by a sea ice concentration of approximately 0-15%, and is separated from the open ocean by a buffer region called the MIZ [1], where the sea ice concentration is approximately comprised between 0-30%, and the physical properties and dynamics of sea ice in the MIZ are impacted by ocean processes, as wave energy is the main responsible for the breakup of sea ice. The MIZ can extend over hundreds of kilometers.

In the MIZ, the ice cover acts as a dampener of wave energy. Smaller floes break up more easily, making them less resistant to further stress. The thinning of the Arctic sea ice cover [46] increases the mean speed of sea ice drift, since thinner ice has reduced material strength [55]. This describes a positive feedback loop; as the fetch areas increase, bigger waves are formed, leading to a higher propagation of the energy of the ocean waves in the ice pack leading to more deformation, more lateral ice melt during summer [55], reduced floe sizes, and more snow ice formation (refreezing of the slush born from flooding of the sea ice snow cover) [58]. The MIZ displays a great variability in floe size, distribution, and mobility. Smaller floes are usually concentrated closer to the open ocean, while bigger floes are expected closer to the ice edge, near the main ice pack. Waves are categorized upon their on their formation mechanism, amplitude, and wavelength. Wind waves are generated by the friction between the wind and the ocean surface. They are characterized by a short wavelength of a couple of meters. Swells are generated by storms, they propagate over vast distances, and have a wavelength of about 100 m.

2.4.2 In-situ and remote sensing methods for wave/ice interactions investigations

The mechanisms of waves in sea ice propagation and the consequences on the breakup and dynamics of the sea ice are being investigated by combining buoy deployments, numerical models [59] and remote sensing. The use of buoys is notably facilitated by the emergence of low-cost open-source waves-in-ice buoys such as the OpenMET buoys [21] and MicroSWIFT [60], described in Section 3.2.1. Buoys are often deployed in the MIZ, rather close to the ice edge, where it is the most accessible by boat, or sometimes by helicopter. It is the case in this study [61], where in situ wave attenuation measurements carried out in the Antarctic MIZ using five wave buoys along a transect of hundreds of kilometers oriented towards the interior of the ice cover. The floe size distribution along the transect was reported to range from 2-3 m close to the ice edge to 10-20 m about 200 km from the ice edge. These measurement showed that the wave height decay is exponential for small waves, and almost linear for larger waves (i.e., waves with a significant wave height over 3 meters), and permitted an assessment of the impact of the floe size distribution on the wave propagation into the ice. In another study in the Antarctic MIZ, an OpenMET buoy that was deployed by boat during the Antarctic summer and survived the winter season provided measurements of swells into sea ice at a distance of 1000 km from the ice edge [62], thus demonstrating the unexpectedly large length-scale of wave propagation into sea ice and the robustness of the OpenMET buoy. In situ measurements of wave/ice interactions on grease ice and land fast ice were realized in [63] and [64] respectively. These studies illustrate how the wave/ice interaction differs depending on the sea ice types.

A wide variety of remote sensing experiments have been carried out to investigate waves/ice interactions. Their combination with in situ experiments is always critical in identifying sea ice types, floe size, and thickness as major wave attenuation factor. For example, ice floes bigger than the wavelength of the wind-waves are responsible for the greatest attenuation rates [65]. This study [66] presents the current remote sensing capabilities for measuring wind-wave attenuation on sea ice, i.e. waves formed by the wind. A brief description of the capabilities of radar sensors is presented hereafter. Ocean wave attenuation coefficients can be derived from the Sentinel-1 Interferometric Wide (IW) mode, in HH polarization. The IW mode allows for a wide coverage (250 km swath) and very high spatial resolution (10 m), although, few measurements are carried out in this mode over sea ice. The most extensive data on waves in ice is provided by the very high resolution (5 m) Sentinel-1 Wave Mode (WM). This acquisition mode has the disadvantage of providing images spaced 100-200 km apart, while the measurement of wave attenuation requires more consecutive radar measurements along a transect. The Extra Wide Swath mode (EW) of Sentinel-1 provides numerous data over the Arctic with coarser data (in the azimuth direction, the pixel size is 43 m). This mode can only detect waves with relatively large wavelengths. When waves penetrate the ice cover, the short wavelengths are rapidly attenuated and only the long wavelengths propagate

with relatively little obstruction through the ice [67]. Ice attenuates waves with wavelengths shorter than 50 m within a few kilometers, allowing SAR to clearly capture longer waves within sea ice [68]. The EW and IW modes can detect waves in ice with a wave height greater than 50 cm [69]. The Surface Wave Investigation and Monitoring (SWIM) instrument is a scatterometer that estimates the directional spectrum of ocean waves. It is sensitive to the large-scale modulation of the waves, and insensitive to the small-scale surface roughness of the water produced by the wind [70]. Although backscatter over sea ice detected by a scatterometer differs significantly from that over ocean waves, the first attempt was made in this study to retrieve wave modulation over sea ice using SWIM [66]. The same study investigated the potential of Sentinel-3 SAR altimetry data to estimate wave modulation in sea ice, using a processing method called "Fully-Focused SAR altimetry" (FF-SAR) [71]. This data processing technique enhances the along-track resolution from altimetry data to its highest theoretical value. Although the wave signature was successfully identified by the FF-SAR altimetry method and the SWIM instrument, more work is required to obtain a more quantitative analysis of the waves [66].

2.5 Sea ice drift retrieval models

There exist several sea ice drift algorithms from satellite measurements. Some of the examples mentioned in Section 2.2 rely on various combinations of active and/or passive sensors. These four algorithms; [20], [42], [72], [73], rely on single and/or combinations of passive sensors, and have made the object of a comparative study [74]. Combining different SARs and/or passive microwave sensors data offers the advantages of more frequent measurements over extended areas. The challenges are that sea ice is highly dynamic, particularly in the MIZ, that in the Fram Strait a flow can drift 50 km in any direction, and that it concentrates 90% of the total Arctic sea ice export [14]. The size and shape of the floes, their orientation and distribution change within minutes to hours, leading to even more significant difference between two consecutive satellite observations, which typically occur every of 1-2 days.

The algorithm used in this thesis is the Chalmers SAR drift retrieval algorithm [20]. It measures the sea ice drift between overlapping subsequent SAR images. It is a hybrid model, that, in particular, combines modified versions of the area tracking by phase correlation method described in [75] and the feature tracking method described in [76]. This section introduces the theoretical background of phase correlation, as well as the methodologies used in these two publications of referencex, in order to motivate the relevance of combining them the way the Chalmers algorithm does. Finally, the section delves into the working mechanisms of the Chalmers algorithm.

2.5.1 Area matching by phase correlation

Phase correlation is a motion estimation technique used for estimating the global motion of an image frame. The shift between two frames is obtained by estimating

the phase component that results from the shift in the frequency domain.

Say two 2D frames are given at times *t-1* and *t*, with sizes [n_1,n_2]. x denotes the pixel intensity in the spatial domain and X denotes the frequency content of the image in the Fourier resulting from having applied a Fast Fourier Transform (FFT) on the image. k denotes the dimensions of the image in the Fourier domain. The amplitude of the two images in the Fourier domain is the same. However, the second image presents a linear phase component. Equation 2.18 is the mathematical expression of the two frames.

$$x_{t-1}(n_1, n_2) \leftrightarrow X_{t-1}(k_1, k_2) \qquad x_t(n_1, n_2) \leftrightarrow X_t(k_1, k_2) \tag{2.18}$$

A fundamental assumption of the phase correlation algorithm is that the image at time t is a shifted version of the image at time *t-1*, by m pixels. In the case of a circular shift, in 2D :

$$x_t(n_1, n_2) = x_{t-1}((n_1 - m_1) \pmod{N_1}, (n_2 - m_2) \pmod{N_2}) \tag{2.19}$$

The discrete Fourier transform of a 2D circularly shifted signal x is given by :

$$X_t(k_1, k_2) = \underbrace{X_{t-1}(k_1, k_2)}_{\text{Amplitude}} \underbrace{\exp\left(-j\frac{2\pi}{N_1}m_1k_1\right)\exp\left(-j\frac{2\pi}{N_2}m_2k_2\right)}_{\text{Phase}} \tag{2.20}$$

The cross-correlation between two images is calculated as follows:

$$C(k_1, k_2) = \frac{X_t(k_1, k_2) \cdot X^*_{t-1}(k_1, k_2)}{|X_t(k_1, k_2)X^*_{t-1}(k_1, k_2)|} \tag{2.21}$$

Substitute $X_t(k_1, k_2)$ in Equation 2.20:

$$C(k_1, k_2) = \frac{|X_{t-1}(k_1, k_2)|^2 \exp\left(-j\frac{2\pi}{N_1}m_1k_1\right)\exp\left(-j\frac{2\pi}{N_2}m_2k_2\right)}{|X_t(k_1, k_2)|^2} \tag{2.22}$$

$$= \exp\left(-j\frac{2\pi}{N_1}m_1k_1\right)\exp\left(-j\frac{2\pi}{N_2}m_2k_2\right) \tag{2.23}$$

The inverse Fourier transform of a periodic signal is Dirac delta function centered at the displacement pixel m. By isolating the maximum peak at coordinates [m_1, m_2], the dominating displacement can be retrieved.

$$c(n_1, n_2) = \delta(n_1 - m_1, n_2 - m_2) \tag{2.24}$$

2.5.2 Foundations of the Chalmers algorithm

Although there exist many different sea ice drift retrieval algorithms, they typically make use of similar motion detection techniques to retrieve sea ice motion. Common motion detection techniques include optical flow, pattern matching, feature tracking, implemented in hierarchical multi-resolution processing systems to improve the

efficiency of the calculations.

Hierarchical multi-resolution SAR drift algorithm: In [75], a drift field is derived from subsequent SAR images using the following scheme: preprocessing, global motion estimation, piecewise local motion estimation, and local linear motion. In this algorithm the motion of the sea ice is based on the tracking of elongated features such as leads and ridges, rather than on individual floes. The preprocessing is performed in two steps. First, adjusting the contrast level of the image in order to make it easier to interpret. Second, the creation of n-level scaled hierarchy of the image. The hierarchy is a collection of the original image which has been subsampled n-times. At each level, a lower-resolution version of the previous image is made. This common computer vision technique helps reduce the computational cost of drift estimation. The Global Motion Estimation consists in estimating a global motion of the sea ice floes by applying the phase correlation technique in a pyramidal resolution scheme. This process starts with the estimation of a draft field from the lowest resolution version of the image. Then, this coarse draft motion field is iteratively refined at higher resolutions, using the previous draft motion field from the previous level as an initial guess. The need for estimating a global motion field arises from the fact that motion detection computer vision techniques perform better on small displacements with a high temporal sampling rate. By removing the global motion between the two images, only the differential motion from the disjoint ice clusters remains in the motion field. Next, is the Piece-wise local motion estimation step, which again happens in a multi-resolution scheme. The two images are divided into initially large blocks (say 25 km^2 for an image of 100 km^2). The phase correlation technique is applied on all block pairs from the two images. When doing so, all the features within the blocks are considered as a rigid unit that move uniformly. This piecewise method allows one to estimate the large coherent motion of ice aggregates. Repeating the same process on blocks with higher resolution allows for more detailed local ice motion estimations. Last, the motion estimation is refined to its finest resolution, at the pixel level, by fitting a Gaussian curve around the peak of the phase-correlation motion estimate. This algorithm was built to detect discontinuous regions, such as leads and ridges, which are present in the heart of the pack ice. However, higher resolution SAR satellite imagery are now able to resolve individual floes, which can be used to estimate sea ice motion in the MIZ, the most dynamical region in terms of floe drift. Therefore, the use of high-resolution SAR imagery for this purpose requires adapted feature tracking techniques.

Ice floe feature tracking algorithm: The Least Average Residual Algorithm (LARA) [76] is a sea ice floes feature tracking algorithm, which was built to improve the identification of ice floes in two subsequent images. LARA identifies the floes by performing a constrained search within a defined search area, which is tailored based on the geometry of the ice field and the size and geometry of the floes. Given two subsequent SAR images in which the contours of the floes have been identified, a neighborhood matrix is constructed using all the floes (the preprocessing image segmentation stage is not detailed in the publication). This matrix ranks the floes on the basis of their Euclidean distance to all the other floes. Smaller floes being more

prone to melting and consequent deformations than bigger floes, only the biggest floes relative to the image size are tracked. The floe identification from one image to the next is carried out iteratively, floe by floe, as follows: at time t_0, the coordinates of each floe edge i are represented by the coordinate sets x_i. Similarly, at time t_1, the floe edge coordinates are represented by the coordinate sets y_i. The floes are identified from one image to the next by finding the coordinates x_r that minimize the equation $\|\mathbf{y}_i - \alpha - \beta\mathbf{x}_r\|$, where α and β are the translation and rotation parameters, respectively. After determining the matching floes in the two images, the motion parameters are estimated by minimizing the equation $\sum_{i=1}^{n} \|\mathbf{y}_i - \alpha - \beta\mathbf{x}_{j(i)}\|$. These parameters are initially estimated based on the distance between floe centroids and an arbitrary rotation, and then refined iteratively.

2.5.3 Chalmers drift algorithm

The Chalmers algorithm provides sea ice drift estimates from pairs of geo-referenced SAR images, by combining the phase correlation method described in [75] and the feature tracking method described in [76], in order to be able to cope with pack ice and marginal ice (ice in the MIZ). The algorithms of these publications will now then be referred to as the reference phase correlation algorithm, and the reference feature tracking algorithm, respectively. The Chalmers algorithm architecture represented in Figure 2.6, serves as the structural framework for the algorithm explanations provided below.

Similar to in the reference phase correlation algorithm, the images are down-sampled, and divided into blocks. In the Chalmers algorithm, the blocks are collocated at the initial iteration, but when an initial draft motion has been estimated, the blocks in the two images are shifted along the direction of the estimated drift, in order to define a tracking region which follows the motion of the sea ice. Next, the area-based matching takes place. Like in the reference phase correlation algorithm, the area-based matching estimates translation motion only. A measure of the correlation at this stage indicates that the coarse motion of the ice in the image block was successfully retrieved. However, a low correlation suggests that rotational motion may have occurred. Therefore, under the condition of low correlation, a succession of search for rotation, phase correlation followed by up-sampling of the image takes place, until the original image resolution is reached and the correlation is high enough. The Chalmers algorithm handles rotation differently than in the reference algorithms, by making use of the Fourier-Melin transform [77], which ensures that the images maintain invariant properties under translation, rotation, and scaling. If the area-based matching gave a low correlation, the next step is the feature-based tracking, which is done at the original image resolution. In the correlation was high enough, then the draft motion field is retained and the image is filtered by a circular weighted median filter and up-sampled to match the image resolution used in the next processing step. The circular weighted median filter offers several advantages; it is a non-linear filter which preserves the edges and removes outliers from the motion field efficiently by being weighted according to the phase-correlation coefficient. Progressively, the iterations are carried out into smaller blocks of increasingly higher

resolutions.

The feature-based tracking employed in the Chalmers algorithm is similar to the reference feature tracking algorithm. Although, the LARA algorithm relies on the coordinates of the contours of the floes in the images, and no specific method is indicated by the authors in their algorithm description. The Chalmers algorithm makes the choice of performing an image segmentation using an improved version of the Otsu threshold selection method [78], which is a common approach for foreground/background identification in the case where the distribution of the image intensities is bimodal, with two normal distribution that are normally distributed. Indeed, in this case, the Otsu threshold tends to segment the image at a pixel intensity too close to the distribution with the highest variance, meaning, the darker portion of the image which represents the water. Following the image segmentation comes a filtering of the floes based upon the geometry, size, stability and the location of the floes to the edges. From the resulting binary image, floes that are too small to be meaningful for tracking, and floes located at the edges of the image are removed, as their contour is unknown. Floes are also filtered according to their solidity, which is calculated as the ratio of the area of the floe to that of its convex hull. A low ratio indicates an inefficient use of space within the boundaries of the floes, suggesting an fragile composition. The fragile portions of the flow are selectively removed for the profit of the most densely packed portion of the floe. Finally, the motion parameters α and β of the floes are estimated as in the reference paper.

The Chalmers algorithm buffers the areas at the edges of the image, in order to avoid attempting to estimate the motion of floes that have drifted out of the image pair. The Chalmers algorithm also focuses on estimating the drift in areas where the land cover is below a certain threshold, in order to prevent coastal effects of inshore waters.

The input parameters to run the Chalmers algorithm are the block size, the downsampling factors, the step size, the size of the circular weighted median filter. The step size refers to the amount of overlapping between adjacent blocks. A step size of 2 means that two adjacent blocks overlap by half of their side length. The parameters were tuned to provide the most efficient runs, as described in the Algorithm Validation and Discussion Section in [20], shown in Section 4.2.

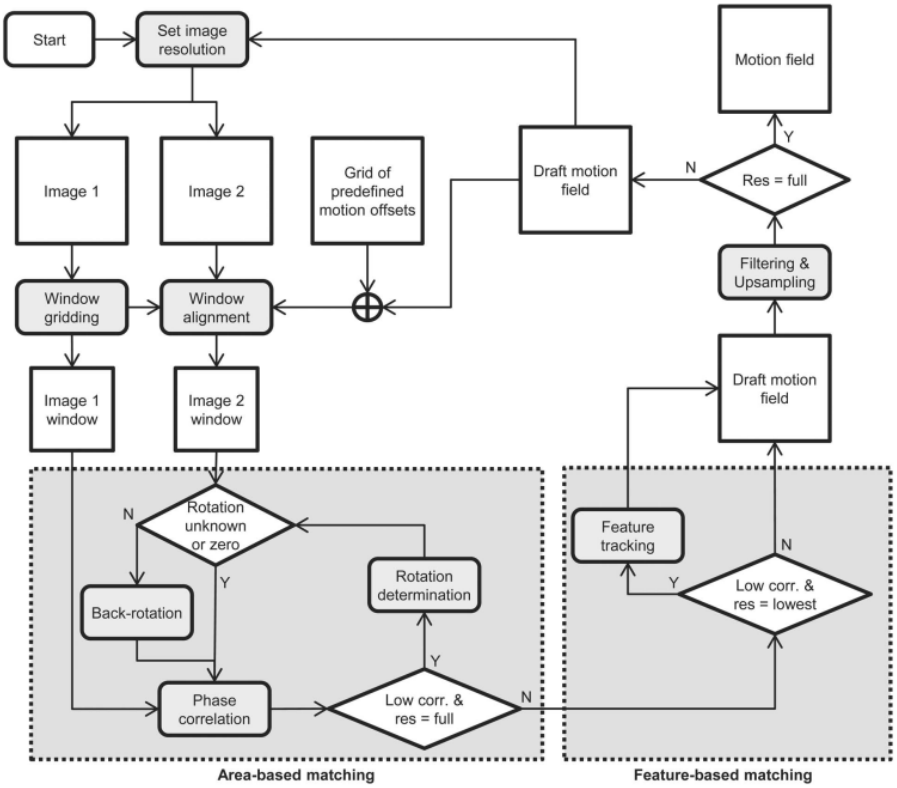

Figure 2.6: Diagram of the Chalmers drift algorithm (used with the permission of the authors) [20].

3

Study area and Data

3.1 Study area

From May 7^{th} until June 15^{th} 2023, the AoM23 expedition took place on board of Research Vessel (R/V) icebreaker Oden, a vessel belonging to the Swedish Maritime Administration. The trajectory of Oden over the study area is presented in Figure 3.1. The ship was in the study area from approximately May 9^{th} to June 13^{th}.

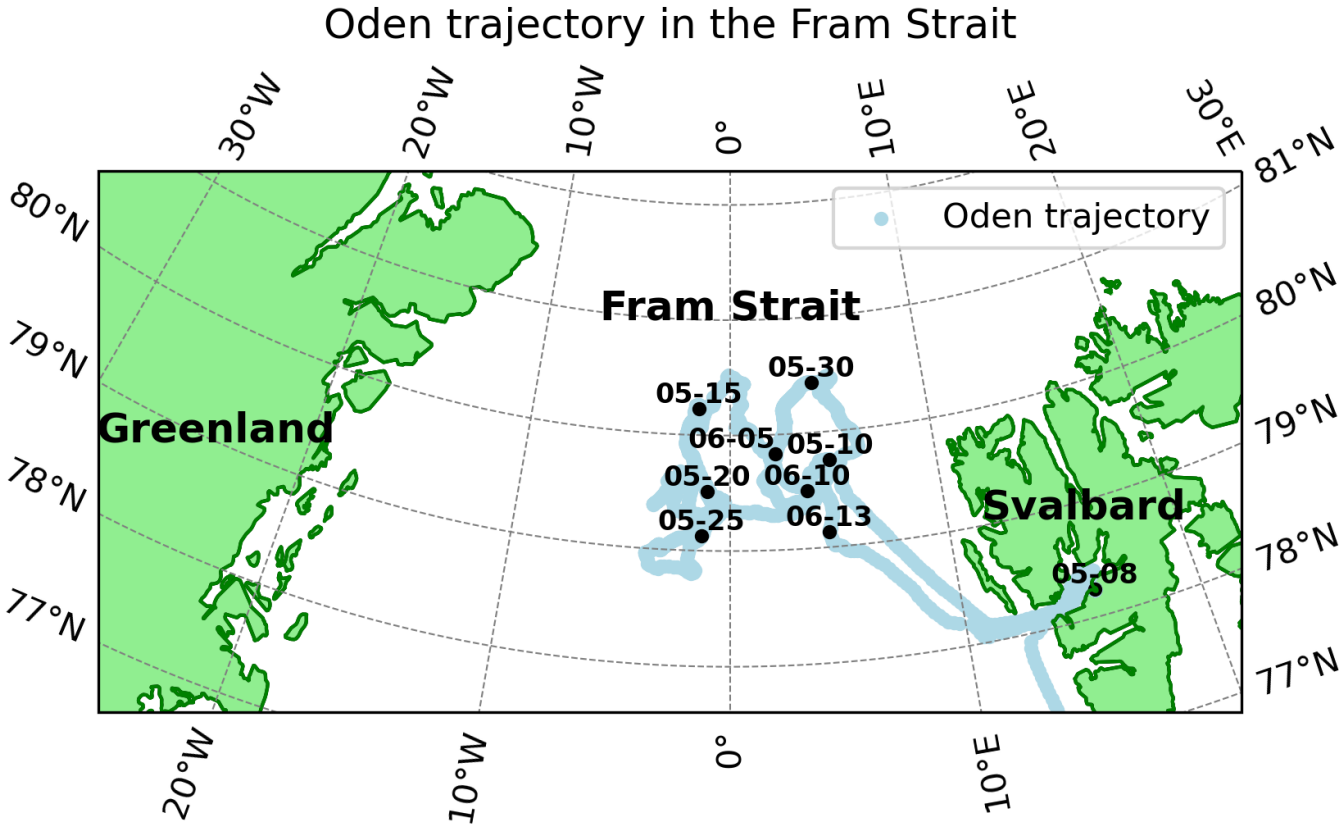

Figure 3.1: Trajectory of R/V Oden during AoM23, in the Fram Strait. The ship departed from Svalbard on May 7^{th} and returned from the Fram Strait on June 15^{th}

3.1.1 Conditions in the field.

Unexpectedly heavy ice conditions prevented Oden from sailing as far north as initially hoped, away from the MIZ. Oden was anchored to Floe 1 on May 16th, which was reported to be 170-180 cm thick. On May 21st, the crew reported the onset of the breaking of Floe 1, and Oden left the floe. A gale occurred on May 25^{th}-26^{th}, attested by the wind data along R/V Oden's trajectory presented in Figure 3.2 breaking large ice floes earlier than anticipated. On May 29^{th} Oden was anchored to Floe 2, where the SIMBA buoy 1001 was deployed. On June 5^{th} it sustained damages after a polar bear encounter. Buoy 1001 was subsequently brought back onboard Oden for repair, and was re-deployed on May 9^{th} by helicopter. From visual inspection of the field conditions made by the crew, melt ponds started to appear towards the end of the expedition. The temperature measurements recorded from the SIMBA buoys at the ice interface, shown in Figure 3.3 indicate that all buoys measured positive temperature from August 10^{th}. This indicates the net melting regime of the floe. The fieldwork area was left on June 13^{th}.

Climate data for temperature, wind and waves conditions in the field are crucial for analysing the sea ice dynamics over the study area. In situ wind and temperature data were obtained from two Weather Stations (WS1 and WS2), that were deployed on the ice over the cruise on May 17^{th} and May 29^{th} respectively. The wind and temperature measurements of the two stations are presented in Appendix A.1 and Appendix A.2. The SIMBA buoys also feature temperature sensors. Moreover, surface temperature, sea ice concentration and waves height and direction data were retrieved from climate reanalysis models. Climate reanalysis climate models combine real climate observations with weather models to reconstruct past weather conditions. The Copernicus Climate Change Service (C3S) provides numerous freely available reanalysis models, including Copernicus Arctic Regional Reanalysis (CARRA, [79]), which was used in this work to obtain 10 m wind and surface temperature reanalysis data. CARRA has a temporal resolution of 3 hours and a spatial resolution of 2.5 km. Another reanalysis model was used; the *Arctic Ocean Wave Analysis and Forecast* model from the E.U. Copernicus Marine Service Information, to obtain ocean waves and sea ice concentration reanalysis data ([80]), at an hourly temporal resolution and a spatial resolution of 3 km.

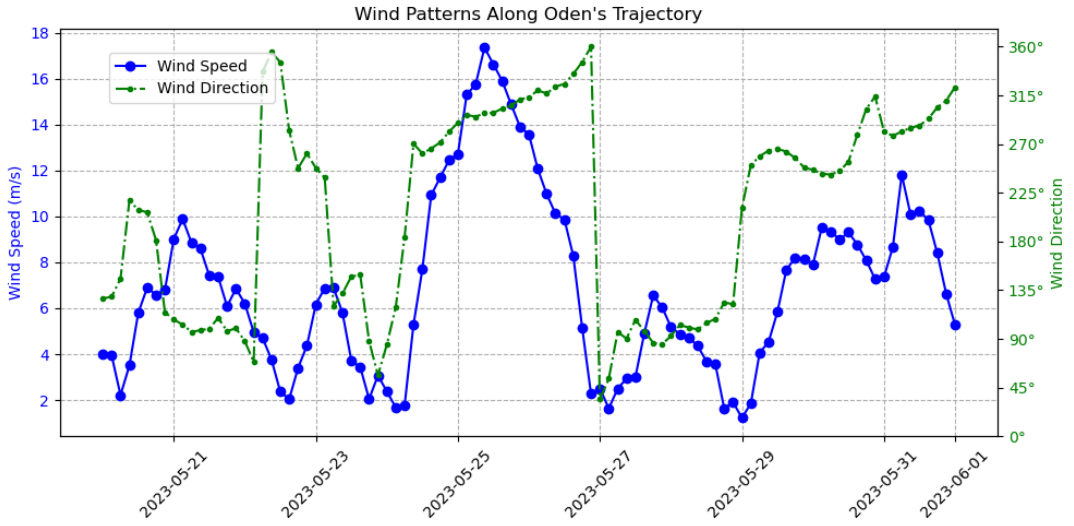

Figure 3.2: CARRA reanalysis wind data over the trajectory of Oden, May 20^{th}-June 1^{st} [79].

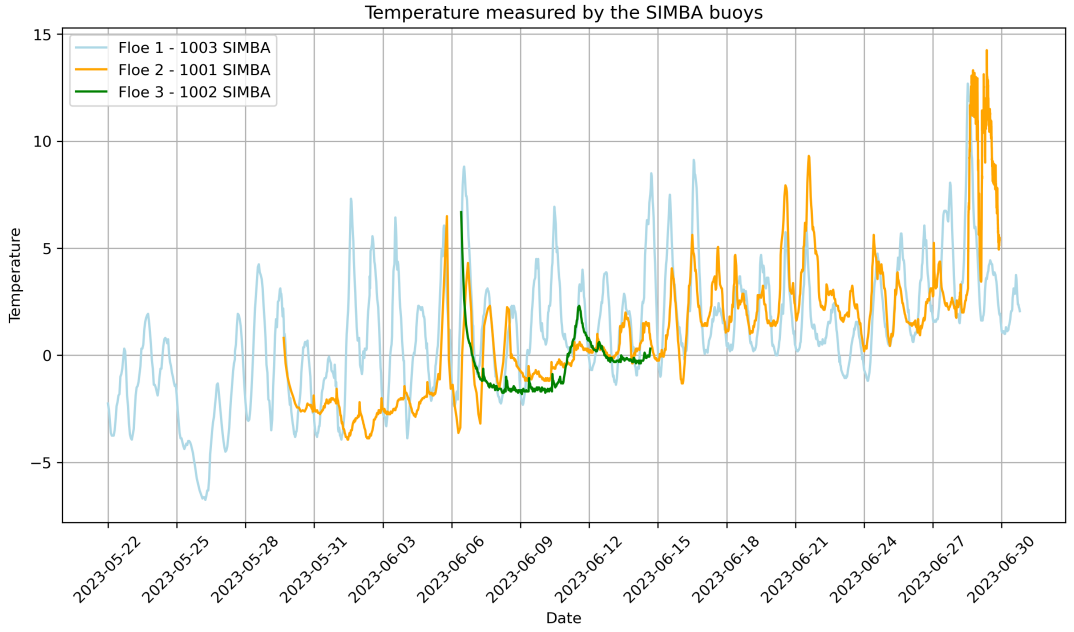

Figure 3.3: Temperature measured by the SIMBA buoys.

3.2 Data

The collection of in-situ observations used to validate satellite observations of sea ice dynamics involved the following steps: deployment of two types of buoys and collection of high and medium resolution radar satellite images. In this section, first, the two types of buoys, their deployment, and their lifespan throughout the field work are presented. Second, the RCM and the S1A satellites are introduced, along with the the specific data that was used, and an overview of the whole RCM and S1A images aligned with buoys is presented.

3.2.1 Buoys data

Two types of buoys were deployed during AoM23, OpenMET [21] and SIMBA [22], described hereafter.

OpenMET: The OpenMET buoys are low cost buoys equipped with GNSS (Global Navigation Satellite Systems), gyro, and accelerometer. Their purpose is to facilitate the horizontal motion, rotation and deformation analysis of the sea ice floe, as well as the analysis of wave action on the floes and in open water. The wave spectra are obtained from the integration of waves data over 20 minutes intervals. In the laboratory, the OpenMET was demonstrated to be able to measure waves as small as 0.1 cm for waves with a period of 16 seconds. The accuracy of the OpenMET was demonstrated under controlled conditions and on the field; in open water, and on sea ice. The results were consistently aligned within 5% of state-of-the-art reference instruments and measurement methods [21]. The GNSS transmits data via Iridium with a temporal resolution of 30 minutes. The model of the GNSS is *GPS ZOE-M8Q*, whose precision ranges from ± 2.5 m to ± 4 m according to the user manual, although the presence of snow on top of the GNSS can alter the quality of the positioning.

SIMBA (Snow and Ice Mass Balance Apparatus): The SIMBA is a sea ice mass balance buoy used to monitor the seasonal evolution of the ice thickness. It measures the temperature profile through the air/snow/ice/water interfaces using a thermistor string with incorporated heaters next to the temperature sensing elements. It permits the measurement of variations in heating temperature and the discrimination of the specific interface the sensor is monitoring. The deployed SIMBA buoys were combined with a GPS, had a 2 cm temperature resolution, and transmitted data via Iridium every 30 minutes. The purpose of the SIMBA buoys in this thesis is to analyze the drift of the floes using its GPS data and validate the Chalmers drift algorithm's predictions, as well as to record wave spectra in order to estimate the strength of the wave / ice interaction over the drift.

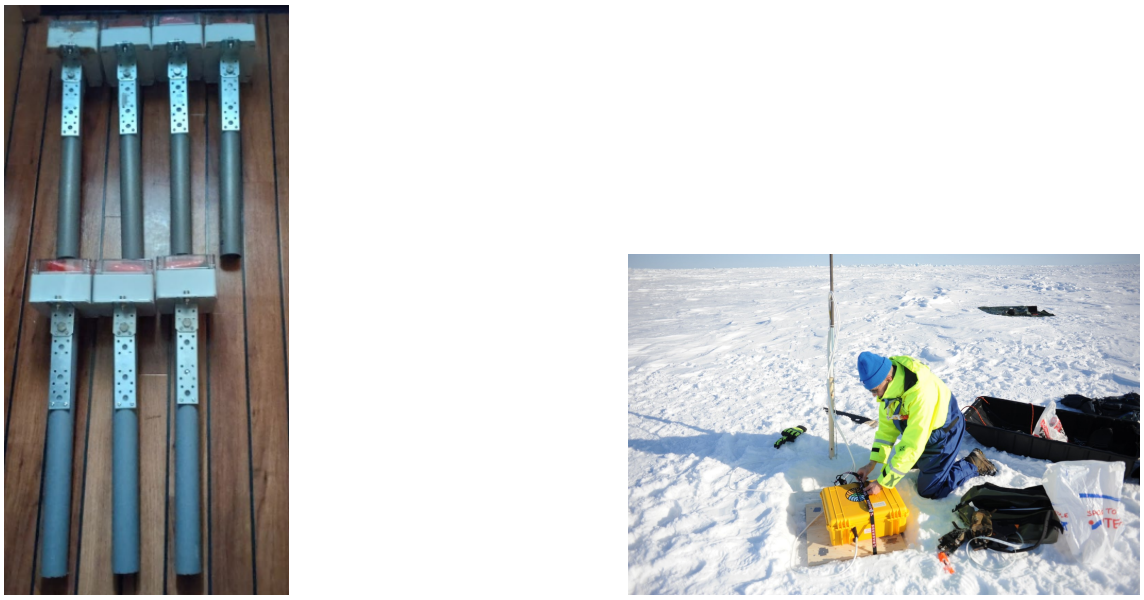

(a) 7 OpenMET-buoys

(b) SIMBA buoy

Figure 3.4: Pictures showing the two different buoys types.

Buoys deployment: In total, seven OpenMET-buoys (Figure 3.4a) and three SIMBA buoys (Figure 3.4b) where deployed on four first-year ice floes in the Marginal Ice Zone (MIZ). The placement of the buoys is shown in Figure 3.5.

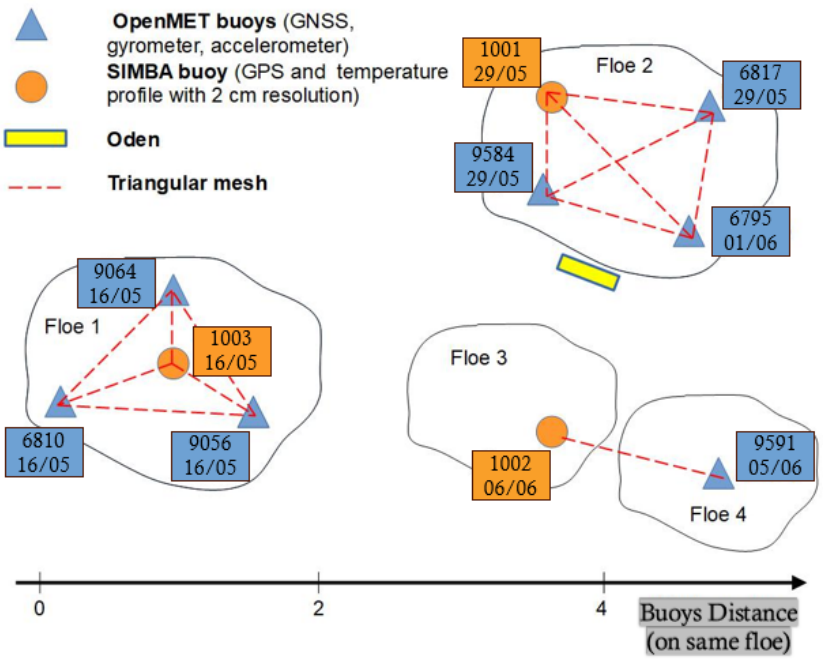

Figure 3.5: Buoy placement on the four ice floes with deployment dates.

The lifespan of every buoy is represented in Figure 3.6, where the buoys on the respective floes have been color-coded. Both the floes 1 & 2 had one of their buoys

(9056 and 9584, respectively) cease functioning unexpectedly soon after their deployment. The longest lived buoy was 6810.

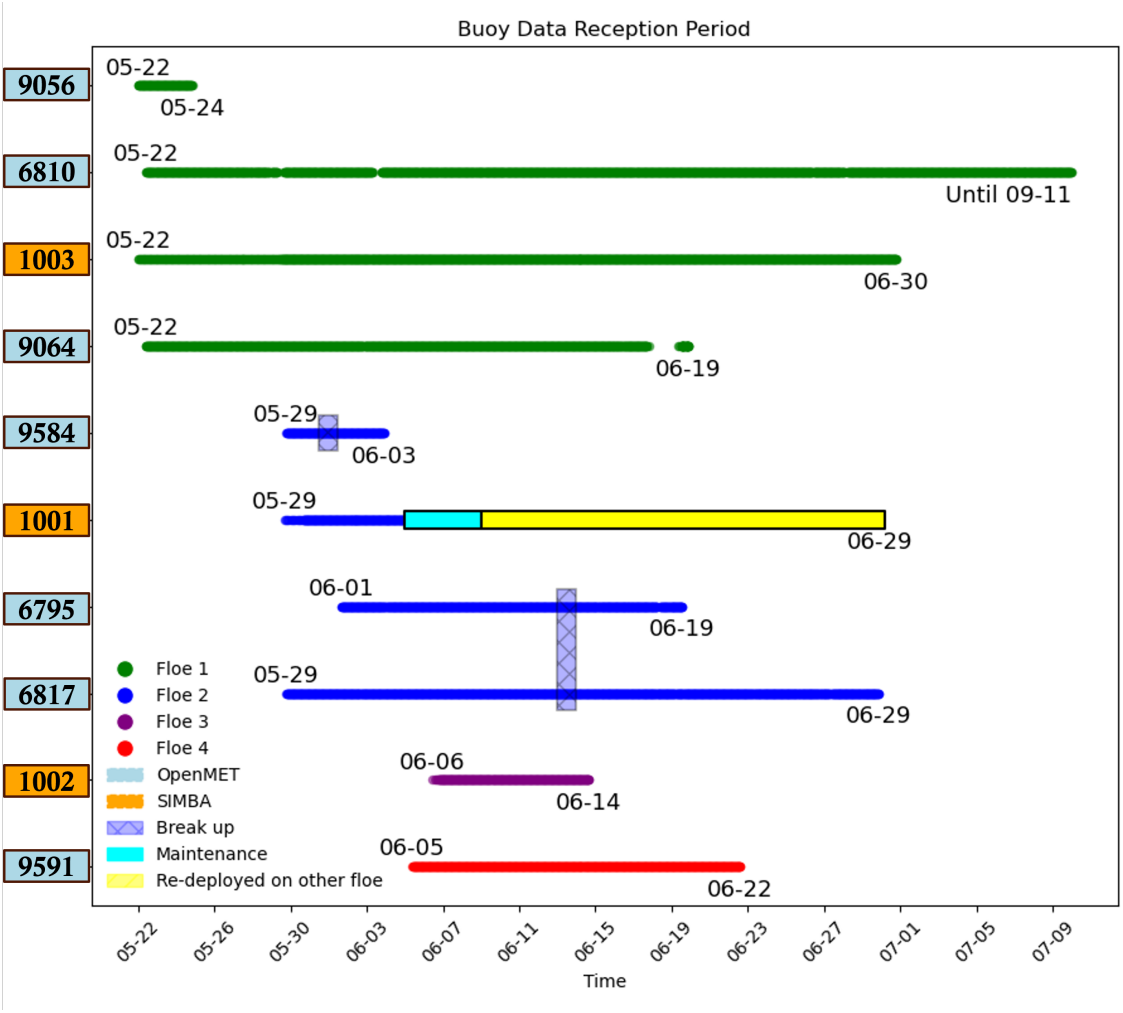

Figure 3.6: Lifespan of the buoys deployed on sea ice floes. The buoys ID written in lightblue indicate the OpenMET buoys. The ones in orange indicate the SIMBA buoys. The color-coding (green, darkblue, purple and red) indicates the floe the buoys were placed on. The vertical dashed lines indicate the dates when buoys that were on the same floe starting drifting apart, indicating the floe broke up. For example, the SIMBA buoy 1001 split from the rest of Floe 2 on June 8^{th}, and the two remaining buoys on that floe, 6795 and 6817, both OpenMET buoys, split on June 14^{th}.

3.2.2 Satellites data

During the cruise, high and medium resolution SAR images from the Radarsat Constellation Misssion (RCM) were ordered in the HH+HV mode over the buoys locations. After the cruise, SAR images from Sentinel-1A (S1A), in Extra-Wide (EW) swath mode (polarizations HH+HV) were downloaded in addition to the RCM images. The technical characteristics of the two satellites, RCM and S1A are presented in Table 3.1.

Table 3.1: Technical characteristics of RCM and S1A.

Characteristic	**Sentinel-1A**	**RCM**
Mission type	Earth observation	Earth observation
Operator	European Space Agency	Canadian Space Agency
Launch date	3 April 2014	12 June 2019
Mission duration	Planned: 7 years	Planned: 7 years (each satellite)
Reference system	Geocentric	Geocentric
Regime	Sun-synchronous	Sun-synchronous
Altitude	693 km	600 km
Period	98.6 minutes	96.4 min
Repeat interval	12 days	12 days
Band	C-band	C band
Available Modes	Stripmap (SM), 5x5m Interferometric Wide swath (IW), 5x20m Extra Wide swath (EW), 25x100m Wave (WV), 5x20m	Low res. (100m) Medium res. (50m, 30m, 16m) High res. (5m) Very High res. (3m)

The characteristics of the data obtained from the RCM and S1A satellites are displayed in Table 3.2.

Table 3.2: Type S1A and RCM data collected during the fieldwork period over the study area.

Sentinel-1A			
Observation Mode	**Resolution [m]**	**Swath Width [km]**	**Polarization Options**
Extra-Wide Swath	40	400	HH+HV
RCM			
Observation Mode	**Resolution [m]**	**Swath Width [km]**	**Polarization Options**
Medium Resolution	50	350	HH+VV, HH+HV
Medium Resolution	30	350	HH+VV, HH+HV
High Resolution	5	30	HH+VV, HH+HV

A summary of all the satellite images containing a buoy within their extent with a buoy/satellite time gap inferior to 1 hour is presented in Figure 3.7.

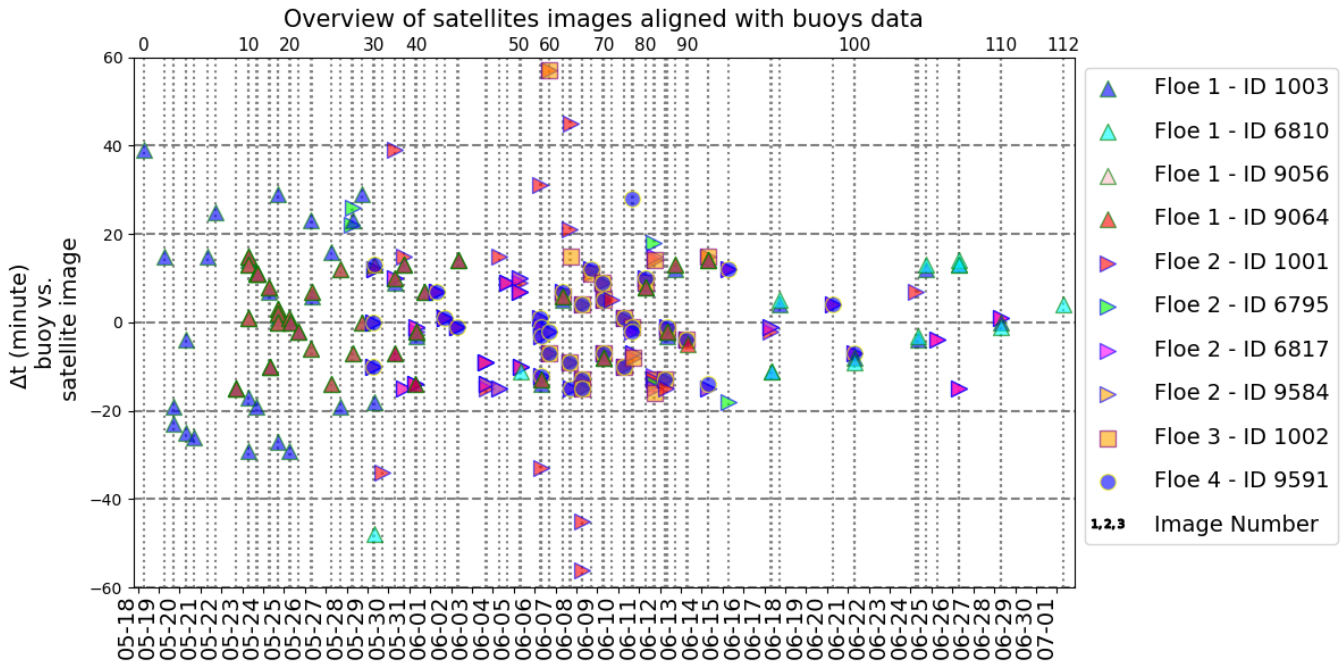

Figure 3.7: Overview of RCM & S1A images aligned with the buoys data. Each vertical dotted line represent satellite image. The colored markers on the line indicates the presence of a buoy within the image. The y-axis indicates the time gap between the data acquisition from the buoy and the satellite image acquisition date. The dashed lines indicate the date of acquisition of the satellite image. The "image number" refers to the index of the image.

3.2.3 Waves Data

Wave spectra were recorded from each of the seven OpenMET buoys, and are presented in power spectral density (PSD) plots, which represents the distribution of power across a range of frequencies. The significant wave height and the wave period are derived from the PSD, as described in [21]. The wave signature measured by a buoy placed on an ice floe can reveal information about the ice / ocean interaction. It also provides clues about the size of the floe, its and melting stage, whether the floe is (A) solid ice, (B) in a transition phase, in which case the buoy would be on a small piece of ice or drifting in the middle of brash ice, or (C) in open water. The best interpretation of the wave signature of a floe requires its observation using satellite imagery in order to consider within the context of its drift environment, whether it is in the middle of the MIZ, at its edge or in the open ocean. When a buoy is located on pack ice, or in a dense cluster of big floes, the ice acts as a dampener of high wave frequencies. On the other hand, when a buoy is on a small, isolated piece of ice, or floating in the open ocean, it is much more subjected to small waves having a large high frequency content. The analyses and interpretation of wave spectra of buoys placed on ice floes is discussed in Section 5.3.

4

Methods

4.1 Analyses of Buoy Data

The evolution of the floes throughout their drift was analyzed by combining numerous data sources. The drift trajectory of the buoys and the ice conditions around them over the drift was investigated using within the open-source Python geospatial stack, using GeoPandas for vector processing, pandas / NumPy for data management and numerical calculations, Shapely and pyproj for geometry and CRS transformations, rasterio and xarray for reading and manipulating gridded sea-ice products, and Matplotlib together with Cartopy for map-based visualisation and QGIS. The break up dates of the floes was also estimated by analyzing their drift on QGIS and Python, calculating the inter-buoy distance on each floe, consulting the AoM23 cruise report, reading personal notes from the crew onboard Oden, and having direct communications with them. The analyses of the wave spectra from the OpenMET buoys also provided clues about the state of the floes; their drifting conditions, either in the middle of other floes or in open ocean as well as their melting stage. Given that we were interested in the drift of the floes, their melting, and the ocean conditions throughout the drift, in situ data from WS1 and WS2 were used, as well as wind and ocean reanalysis data, in order to identify strong weather events and their impact on the ocean conditions.

The interpretation of the wave spectra was carried out after personal communications with Jean Rabault, and the explanations provided in [81].

The sea ice kinematics equations were calculated for Floes 1 and 2, by considering only the three OpenMET buoys that were deployed on them. This approach was adopted for the following reasons: On Floe 1, the SIMBA buoy 1003 was placed in the middle of the floe, therefore we decided to only consider the ones at the edges. On Floe 2, the SIMBA buoy 1002 had been damaged by a polar bear encounter soon after its deployment, and was subsequently re-deployed on a separate floe. Although every buoy recorded at nominal 30-minute intervals, their clocks were offset by only a few seconds. To align the time stamps, each buoy's record was resampled to exact 30-minute steps.

4.2 Analysis of high resolution radar satellite images

Several hundred satellite images were acquired during the field campaign. The Chalmers drift algorithm was used with satellite image pairs that were filtered as follows :

- The two satellite images must have captured the same buoy.
- The acquisition time of each satellite image must fall within 5 minutes of the corresponding buoy timestamp.
- The interval between the two satellite images must be between 1 hour and 24 hours.
- The two satellite images must have the same resolution.

The performance of the Chalmers algorithm is assessed by comparing its drift vectors to the actual drift of the buoys. Because the algorithm only provides drift vectors at locations where it successfully identified and tracked ice floes in the two successive images, there may not be an perfect overlap between the in situ drift measurements and the drift vectors. In this report, we consider the flow of sea ice to be approximately homogeneous within a length scale of 5 km. This assumption allows us to compare the in situ drift measurements with the nearest drift vector, and with drift vectors located within a 5 km radius around the buoys. When in-situ drift measurements are available within a 5 km radius, we compare their mean drift direction (azimuth angle from North) and speed with (i) the drift vector nearest to the buoy and (ii) the mean of all satellite-derived drift vectors within the same 5 km radius. Although the drift field is not perfectly homogeneous, this comparison helps evaluate the ability of the Chalmers drift algorithm to reproduce the observed sea-ice motion.

5
Results

The results are presented in three parts. First, the trajectories of the buoys, the floe-fracture date for each buoy and the buoy-divergence date are presented using the GPS/GNSS data of the buoys, combined with satellite imagery which provides information on the ice conditions around them as they drift. Second, the drift predictions from the Chalmers algorithm are presented. Last, the wave data measured from the buoys are presented. This report presents results from May 16^{th} to July 1^{st}.

5.1 Buoys drift analyses

The trajectories of each buoy and of the two WS are depicted in Figure 5.1. WS1 was deployed on May 16^{th}. Buoys 1003, 9064, 9056, 6810 were deployed on Floe 1 on the same day, however, due to delays with the Iridium satellite service, data from these buoys were not received until May 22^{nd}. These buoys headed south-west, along the East-Greenland current. Subsequently, buoys 1001, 9584, 6817 were deployed on floe 2 on May 29^{th}. WS2 was also deployed on this day. The deployment of the fourth buoy on floe 2; 6795, was delayed until June 1^{st}. Buoy 9591 was deployed on floe 4 on June 1^{st}. Buoy 1002 was deployed on floe 3 on June 6^{th}. Floes 2, 3 and 4 headed towards the north-western coast of Svalbard. Buoy 6810 was the longest lived buoy. After its supporting ice floe melted, it drifted in open water along the East-Greenland current, and ceased functioning after having passed the southern tip of Greenland on September 11^{th}. Given that Floe 1 did not provide data before May 22^{nd}, but was deployed on the same day as WS1, the drift of Floe 1 can be inferred from that of WS1 between those two dates.

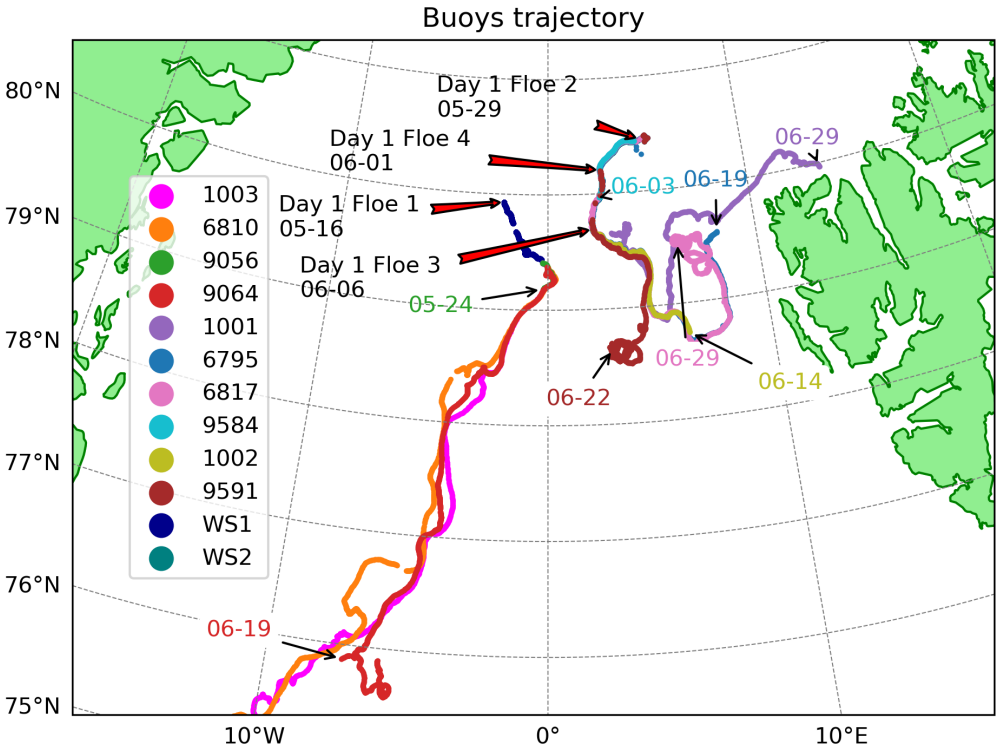

Figure 5.1: Trajectories of the buoys and the two WS. WS1 and buoys were deployed on Floe 1 on May 16th. WS1 was removed on May 21st. WS2 was deployed on May 29th and drifted along the same trajectory as Floe 2 until its removal on June 11th. "Day 1" refers to the deployment date of a first buoy on a floe. The buoys dates indicate the day each buoy ceased functioning.

5.1.1 Floe 1

Buoys 9056, 6810, 9064 and 1003 were deployed on Floe 1 on May 16th. Figure 5.2 represents the inter-buoy distances between buoys 6810, 9056 and 9064, although buoy 9056 ceased functioning on May 24th in the evening. The crew onboard Oden reported that Floe 1 started to break up on May 21st. Globally, the disjointed buoys drifted south-west. The inter-buoy distances started diverging significantly from May 22nd at 12pm, when the buoys drifted along a circular path, shown in Figure 5.3, representing the trajectory followed by Floe 1 on May 22nd-25th.

Figure 5.4 shows that on May 26th, buoy 6810 was following a trajectory slightly different than that of buoys 9064 and 1003, which remained close to each other on that date, until May 27nd.

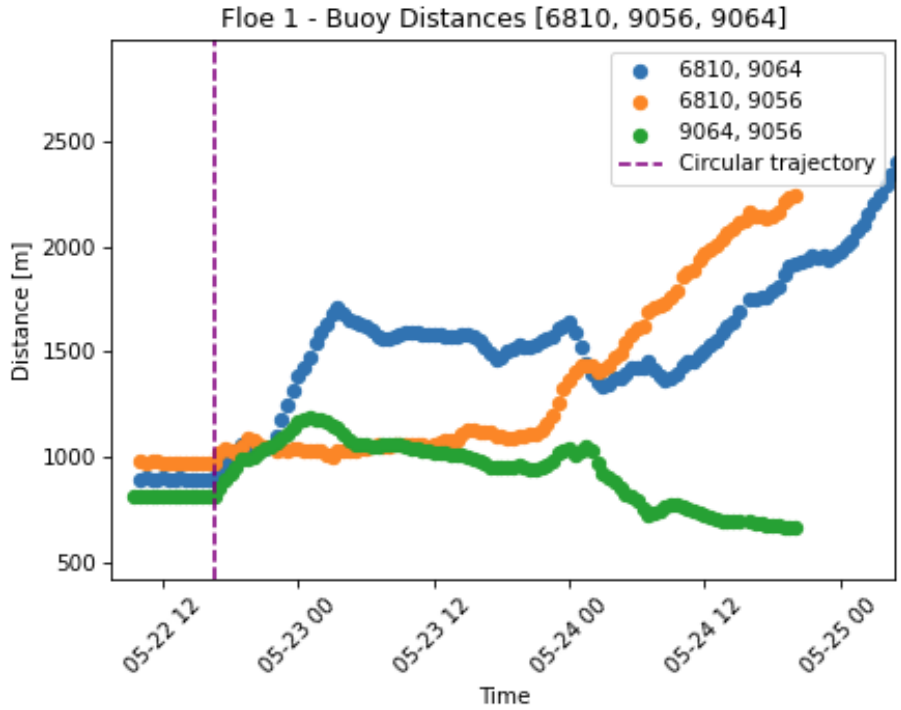

Figure 5.2: Inter-buoy distances on Floe 1 [6810, 9056, 9064]. The floe started to break up on May 21^{st}. The initial distance on May 22^{st} at 10:00 am was 977 m between buoys [6810, 9056] (orange), 897 m between buoys [6810, 9064], and 819 m between buoys [9064, 9056].

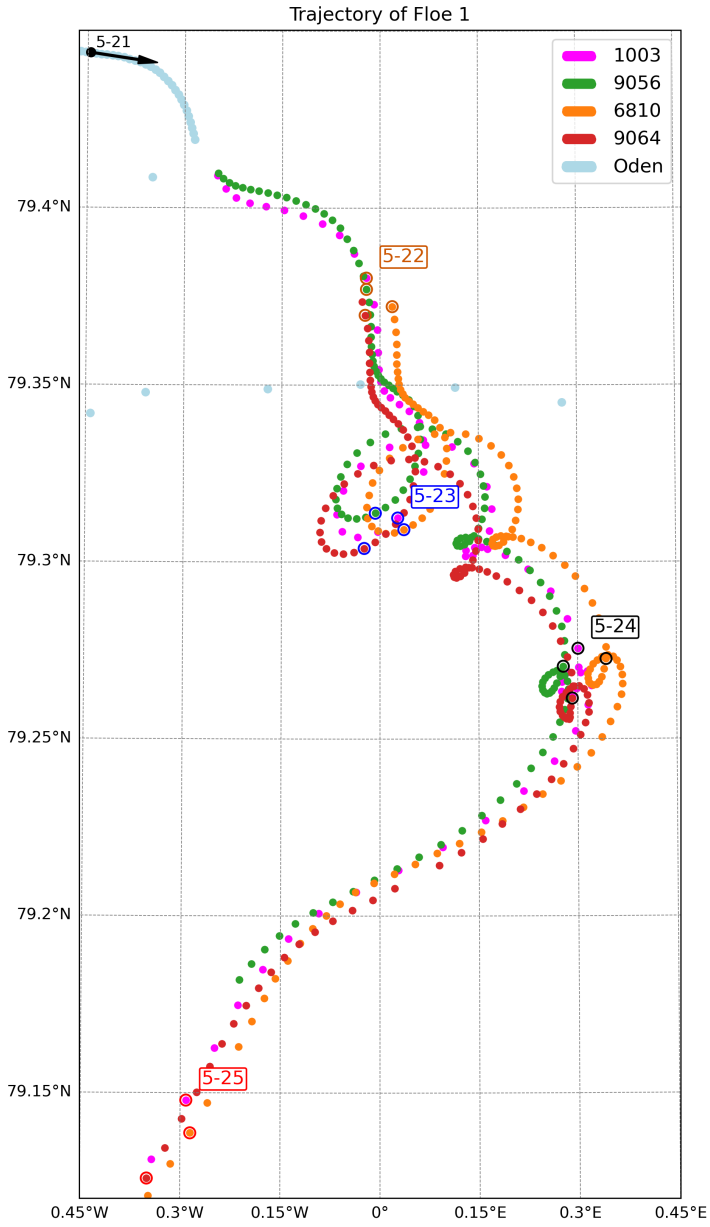

Figure 5.3: Between May 22^{nd} and May 25^{th} the buoys of Floe 1 drifted along a similar trajectory, and were all subjected to a drift pattern which made them follow circular paths, three times. The last location of buoy 9056 before it died is visible in the plot.

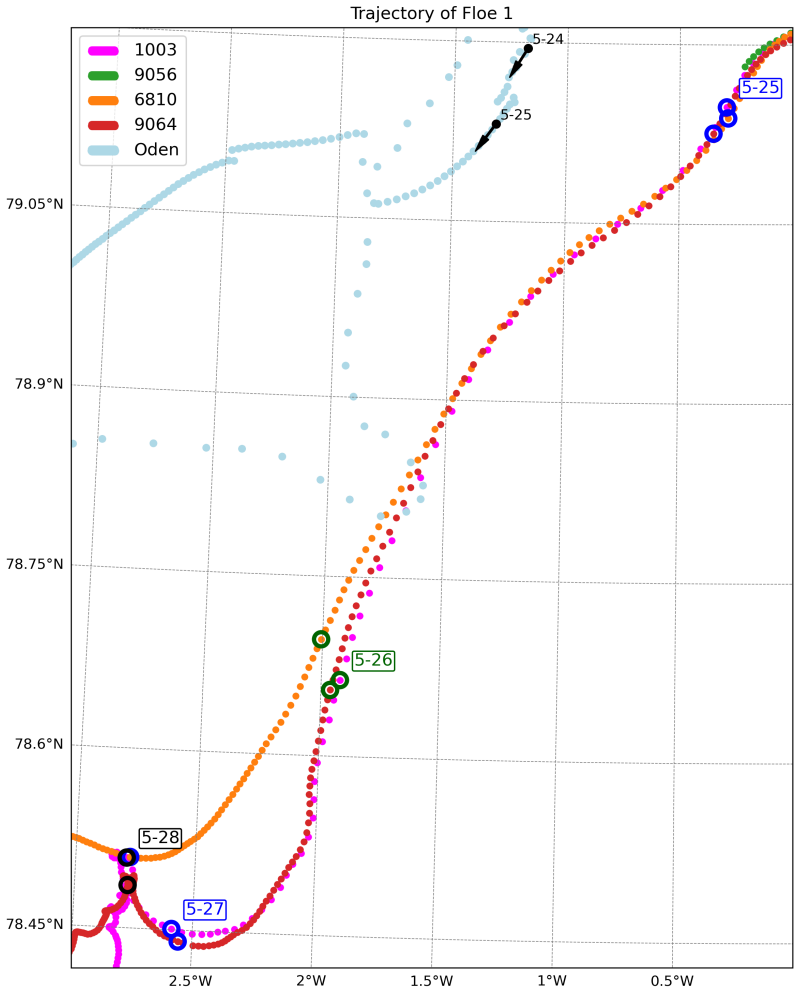

Figure 5.4: On May 26^{nd}, buoy 6810 started following a trajectory significantly different than 9064 and 1003. On May 27^{th}, this happened to buoys 9064 and 1003.

Satellite images taken over Floe 1 on May 26^{th} and May 30^{th} are shown in Figure 5.5a and 5.5b respectively. These are the two images available capturing buoys 1003, 9064 and 6810 closest to when the buoys were following slightly different trajectories. The satellite images are included in order to identify the proximity of the buoys to the open ocean and the ice conditions in the MIZ around the buoys. In the MIZ, ice conditions are chaotic, ice floes are expected to drift faster, and are subjected to the strongest wave / ice interactions. Because there is no perfect overlap between the moment the satellite image is captured and the buoy data acquisition date, there is a time gap between the two indicated by Δt in the legend. The date of the satellite image is the reference date, therefore, $\Delta t = 2$ min means that the buoy location displayed corresponds to the buoy position 2 minutes after the satellite image was taken. Throughout this report we show only satellite scenes captured within 15 minutes of the corresponding buoy timestamp when illustrating ice conditions and drift, whereas the Chalmers drift algorithm is run exclusively with images whose acquisition times differ from the buoy record by 5 minutes. The wave height, wave direction and sea ice concentration reanalysis data from ERA5 shown in this section

(Section 5.1) will be discussed in Section 5.3.

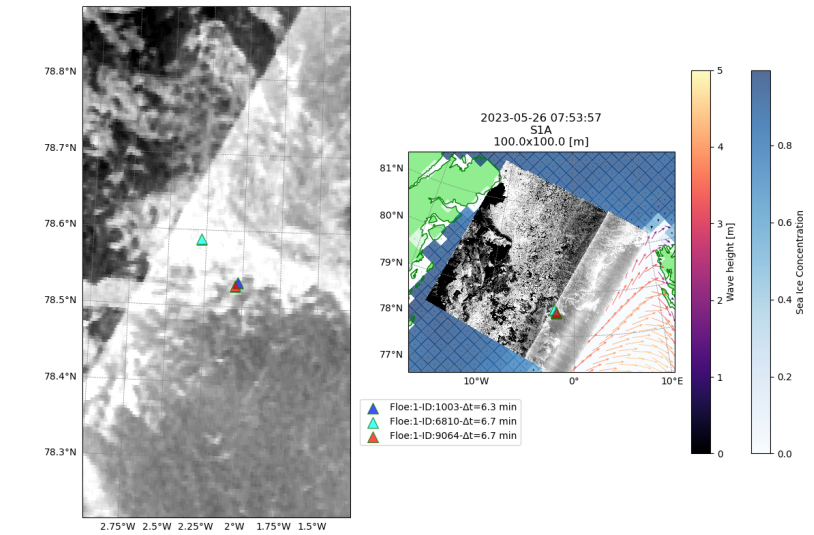

(a)

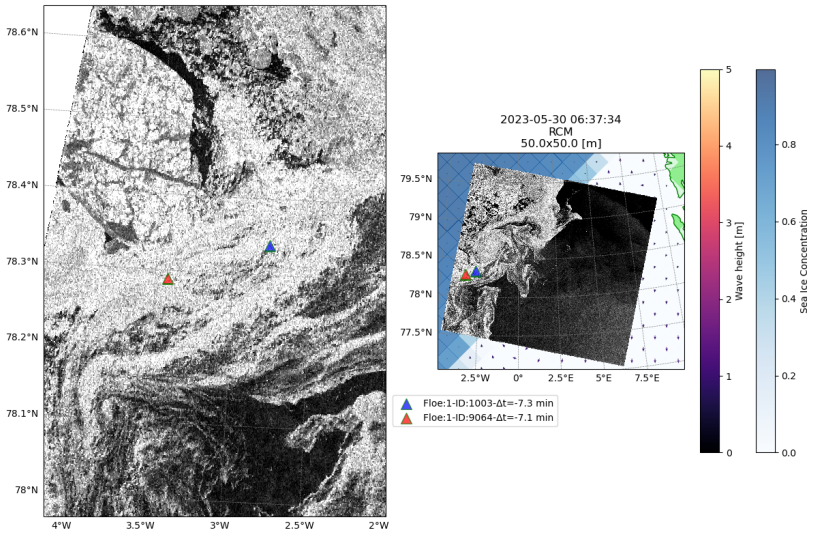

(b)

Figure 5.5: S1A and RCM images over Floe 1, at dates closest to when buoys 6810, 9064 and 1003 were drifting away from each other. Δt designates the time gap between the satellite image time and the buoy data acquisition time. **a)** On May 26^{nd} at 07:53 am, buoy 6810 was about 5 km away from buoys 9064 and 1003, while these two were about 500 m away from each other, and about 5 km away from the open ocean, where waves about 3 m high were present, propagating towards the north-east. **b)** On May 30^{th} at 06:37 am, buoys 9064 and 1003 were about 14.5 km away each other.

The shear and divergence rates of Floe 1 are shown in Figure 5.6a. The rotation rate of Floe 1 is shown in Figure 5.6b, derived from the equations presented in Section 2.3.4.

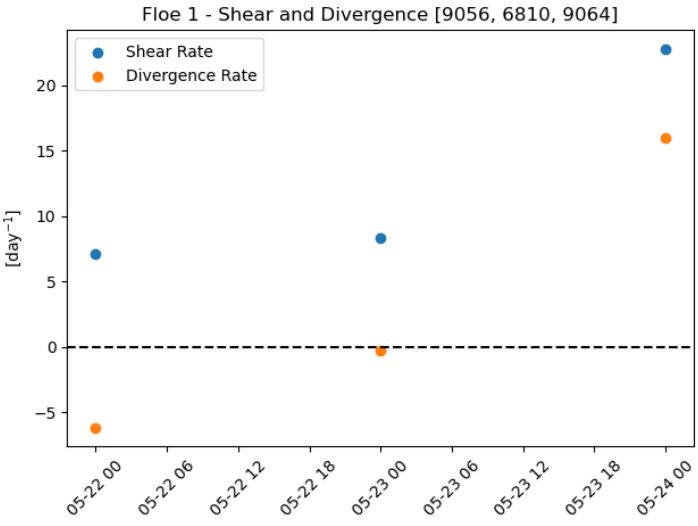

(a)

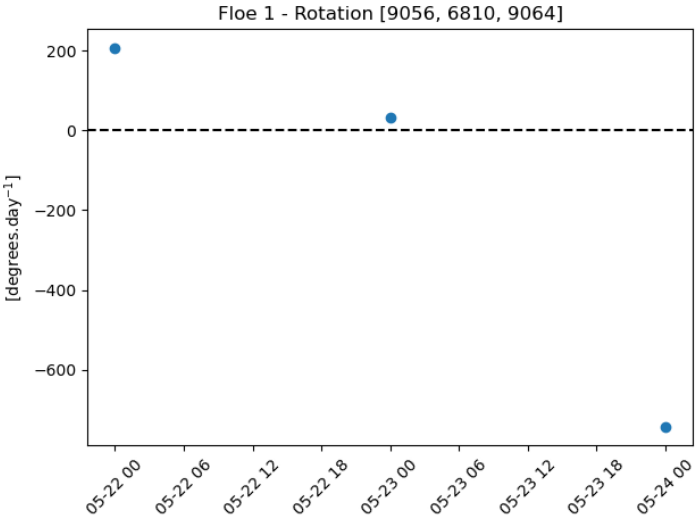

(b)

Figure 5.6: Analysis of buoys [9056, 6810, 9064] on Floe 1: **a)** Shear and divergence rates. **b)** Rotation rate.

5.1.2 Floe 2

Buoy 9584, 6817 and 1001 were deployed on Floe on 2 on May 29^{th}. An attempt was made to deploy buoy 6795 on that day as well, but it finally was delayed until June 1^{st} in the evening. Figure 5.7 represents the inter-buoy distances between buoys 9584, 6817 and 6795. The portion of Floe 2 on which buoy 9584 was deployed broke off in the night between May 31^{st} and June 1^{st}. Buoy 9584 ceased functioning on June 3^{rd}. Buoys 6817 and 6795 remained on Floe 2 until they separated on June 13^{th}.

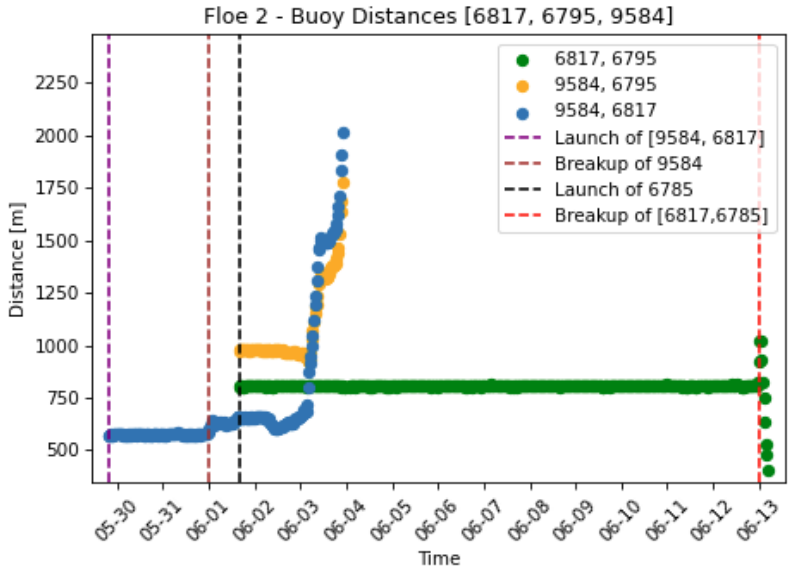

(a) Buoy 9584 was deployed on May 29^{th}, and broke off in the night of May 31^{st}. Buoy 6795 was deployed on June 1^{st} in the evening. Compared to the other buoys, buoys 6795 and 6817 are the buoys pair which remained together on a floe for the longest time (13 days) until till they broke off on June 13^{th}.

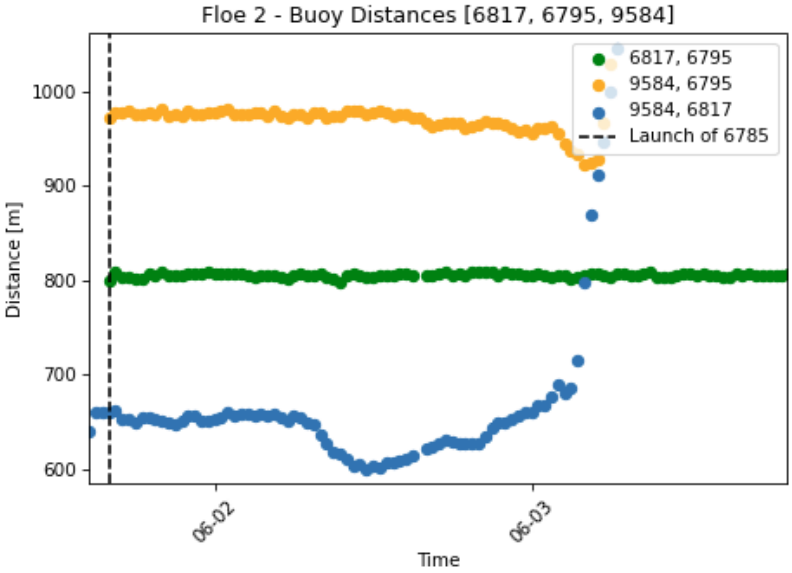

(b) Buoy 9584 broke off on June 2^{nd}. Buoys 6795 and 6817 broke off on June 13^{th} (not shown in the figure).

Figure 5.7: Inter-buoy distance between buoys 9584, 6795 and 6817. Buoy 9584 broke off on June 2^{nd}. Buoys 6817 and 6795 remained on Floe 2 until June 13^{th}, where they broke off. Those buoys drifted together until they took different trajectories on June 18^{th}.

Figures 5.8–5.9 show the trajectories of buoys 6817, 6795, and 1001 on Floe 2. On June 5^{th}, buoy 1001 was damaged by a polar bear. Thus, it was retrieved onboard Oden, repaired, and finally redeployed on June 9^{th} on another floe. Buoys 6795 and 6817 followed a similar trajectory until June 18^{th}.

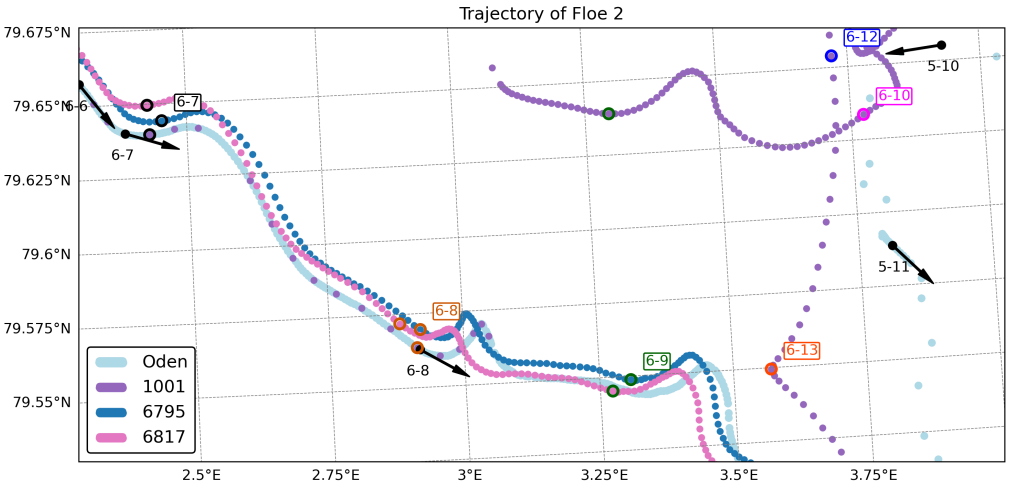

Figure 5.8: Trajectory of Floe 2 on May June 9^{th}-13^{th}. Buoy 1001 was brought back on Oden on June 5^{th} and re-deployed by helicopter on June 9^{th}.

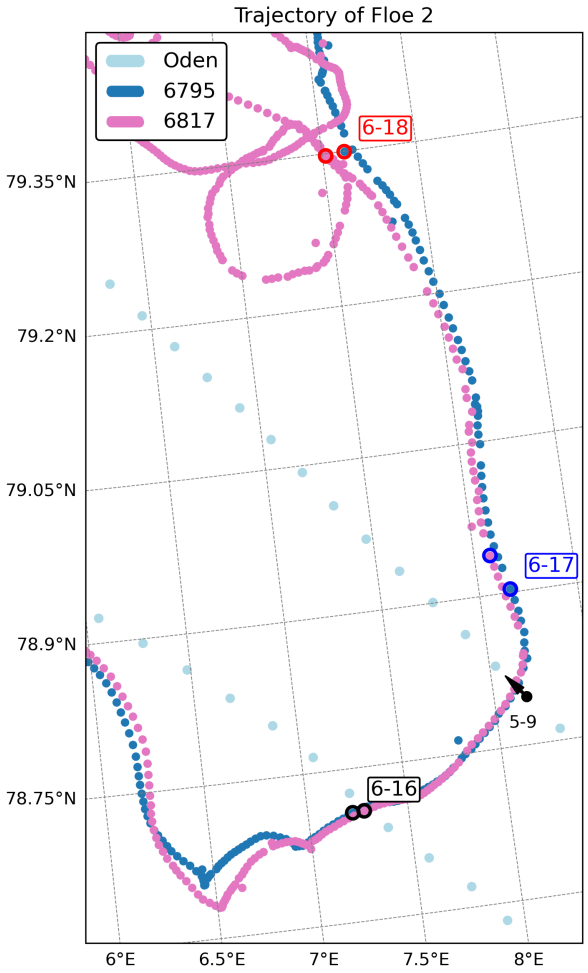

Figure 5.9: Buoys 6795 and 6817 broke off on June 13^{th}, but drifted together until they took different trajectories on June 17^{th}.

Figures 5.10a and 5.10b show satellite images over Floes 2,3, and 4 on June 12^{th} and June 17^{th} respectively. On Figure 5.10a, buoys 6817 and 6795 were drifting along the same trajectory, until June 17^{th}, shown in Figure 5.10b, where the two buoys were in open ocean.

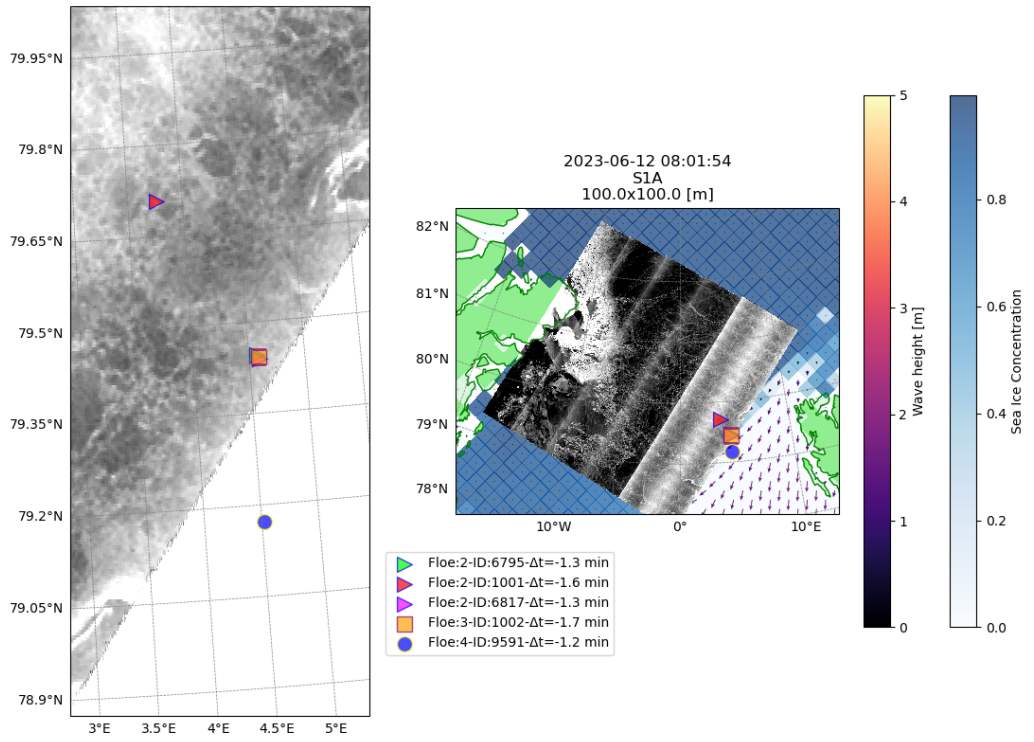

(a)

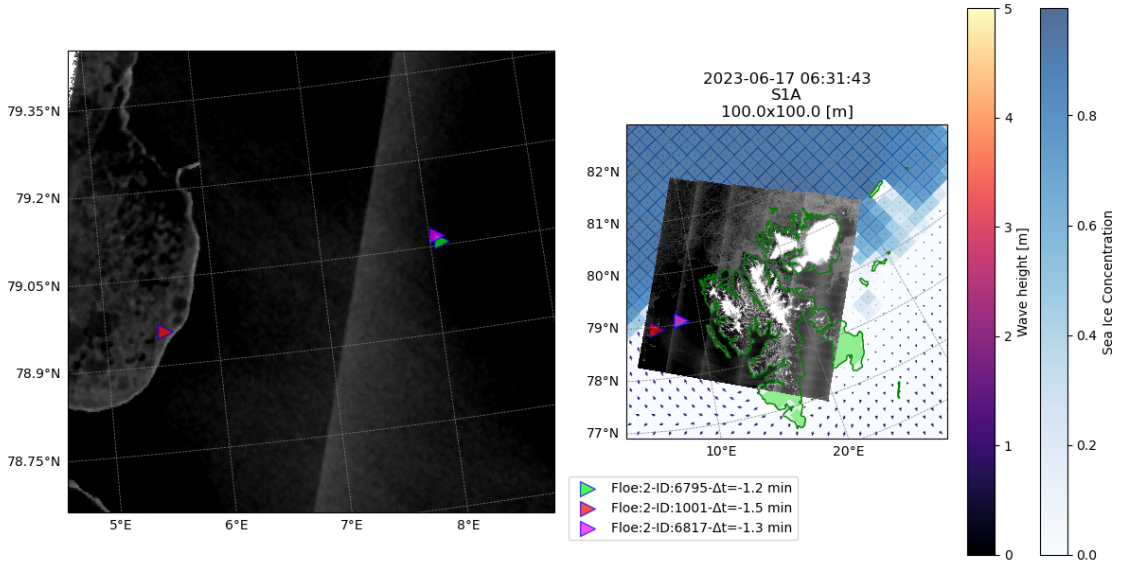

(b)

Figure 5.10: S1A images taken over Floes 2, 3, and 4. **a)** On June 12^{th} at 08:01 am, buoys 6795 and 6817 were still attached to Floe 2. They broke off on June 13^{th}, but drifted together until they took a different trajectories on June 17^{th}. **b)** On June 17^{th} at 06:31 am, when buoys 6795 and 6817 were drifting away from each other, they were in the open ocean.

For Floes 2, 3 and 4, the transition between drifting in the MIZ (e.g., in the middle of numerous ice floes) and in open ocean occurred between June 13^{th} (Figure 5.11a) and June 14^{th} (Figure 5.11b).

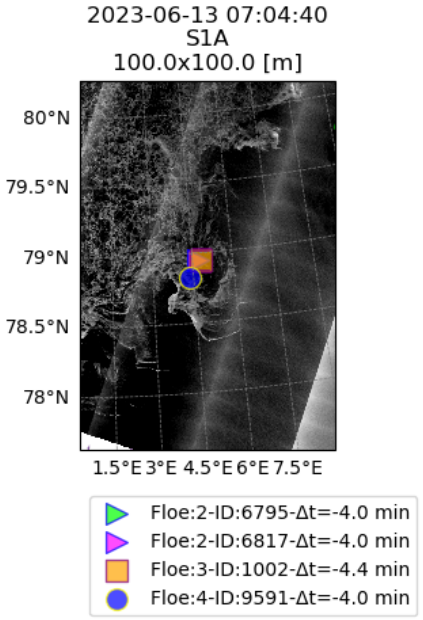

(a)

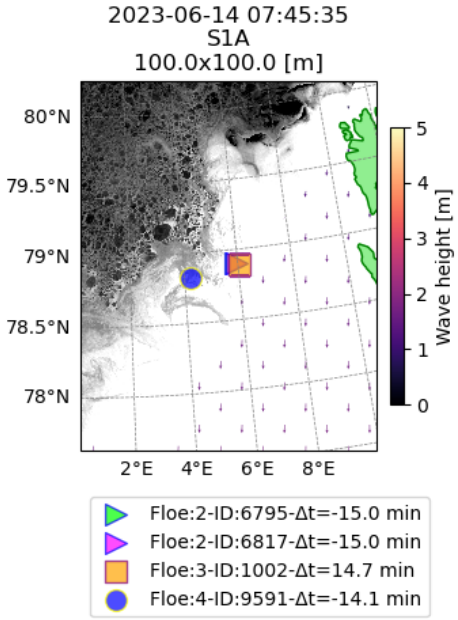

(b)

Figure 5.11: S1A images over Floes 2, 3 and 4, showing their transition between drifting in the MIZ and in the open ocean. **a)** On June 13^{th} at 07:04 am, the three floes were in the MIZ. **b)** On June 14^{th} at 07:45 am, they were drifting in the open ocean.

The shear and divergence rates of Floe 2 are shown in Figure 5.12a. The rotation

rate of Floe 2 is shown in Figure 5.12b, derived from the equations in Section 2.3.4.

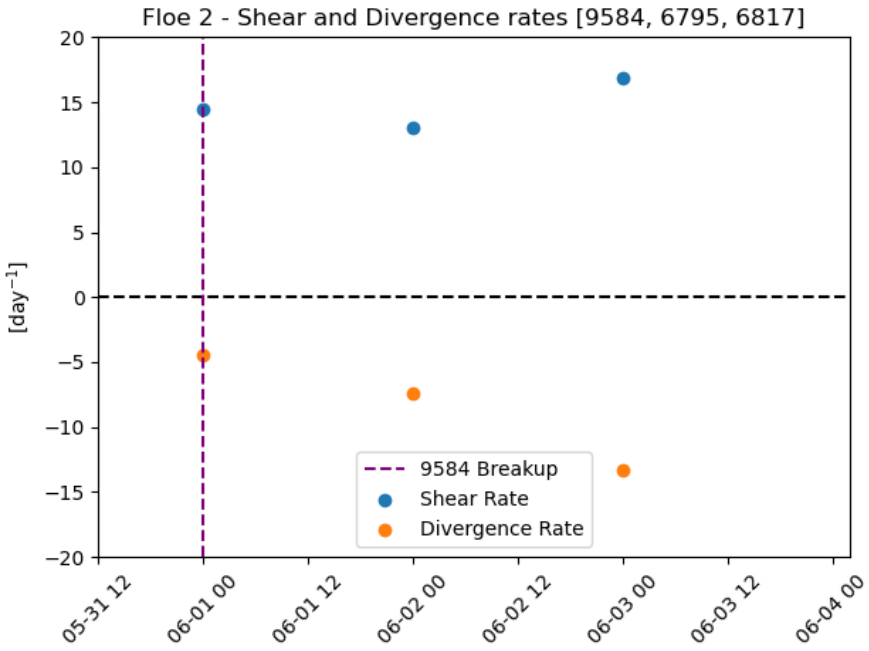

(a)

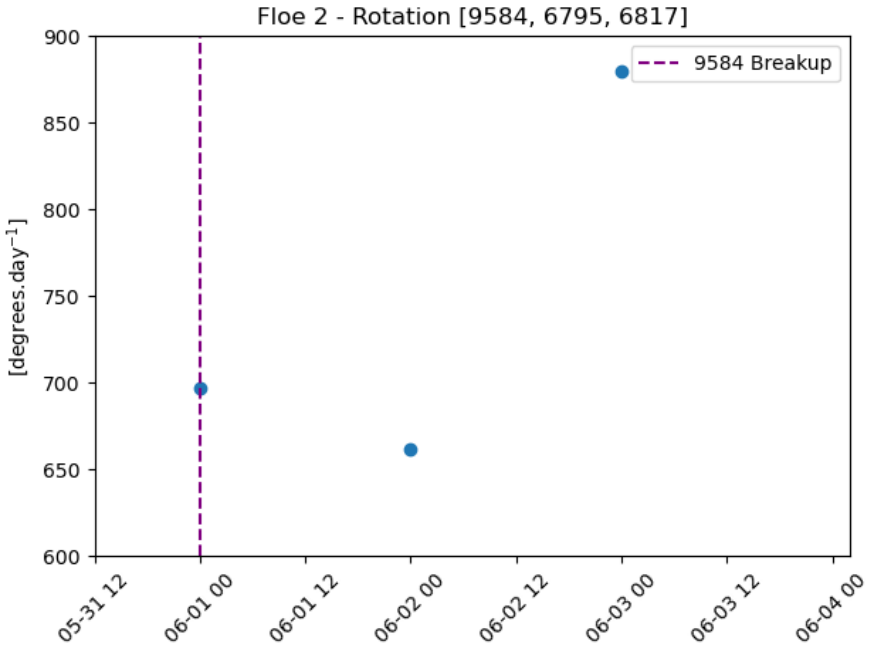

(b)

Figure 5.12: Analysis of buoys [9584, 6795, 6817] on Floe 2: **a)** Shear and divergence rates. **b)** Rotation rate.

5.1.3 Floes 3 and 4

Buoy 9591 was deployed on Floe 4 on June 1^{st}. Buoy 1002 was deployed on Floe 3 on June 6^{th}. The trajectories of Floes 3 and 4 are represented in Figures 5.13, along with the trajectory of Floe 2. Floe 3 drifted together with Floe 2 at least until buoy 1002 ceased functioning on June 14^{th}. Floe 4 drifted away from Floes 2 and 3 from June 11th. As mentioned earlier, the transition between drifting in the middle of the ice and in open ocean occurred for Floes 3 and 4 between June 13^{th}-14^{th} at the same time as for Floe 2, as shown in Figure 5.11.

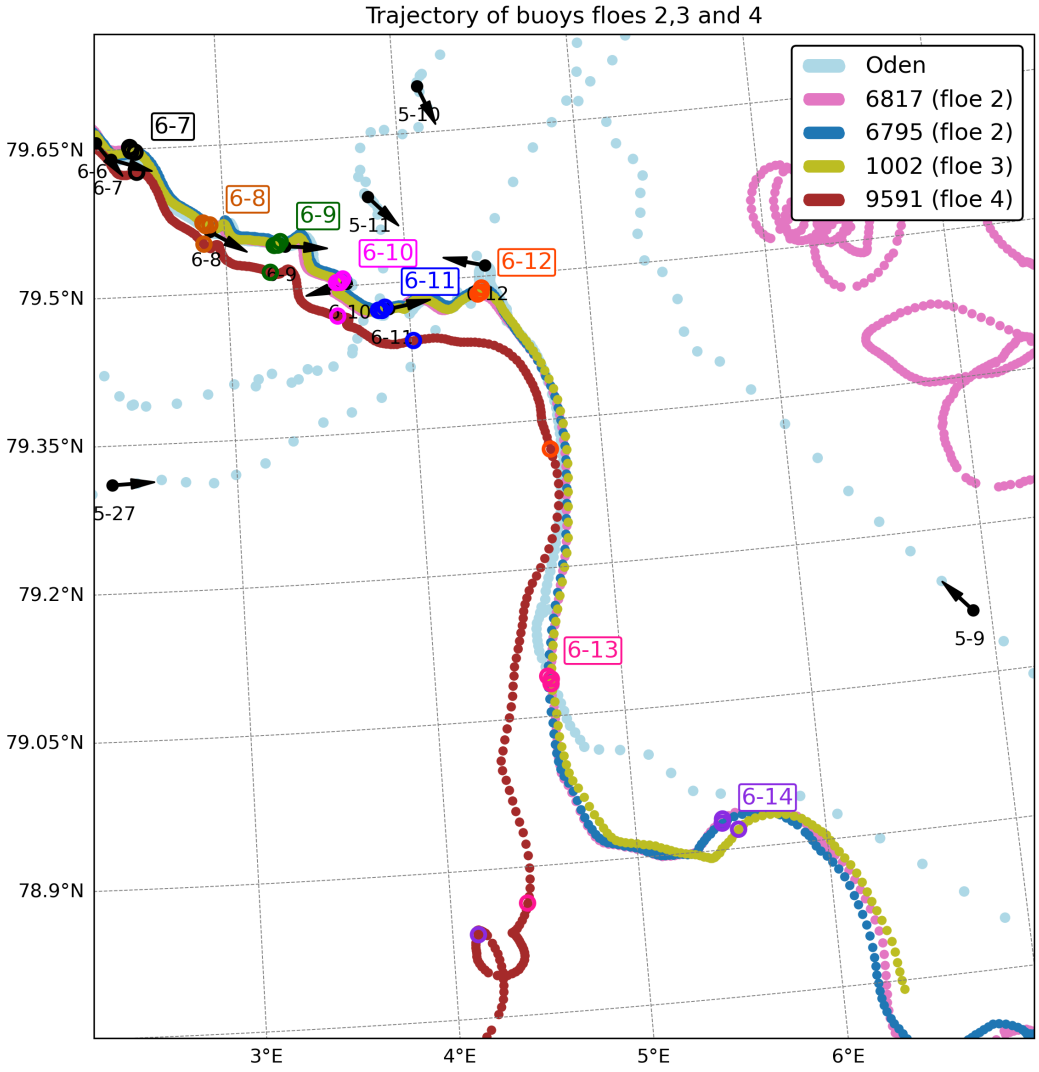

Figure 5.13: Buoys 6795 and 6817 broke up on June 13^{th}, but drifted together until they took a different trajectories on June 18^{th}.

5.2 Drift estimates from the Chalmers algorithm.

A total of 8 image pairs were retrieved from the filtering conditions cited in Section 4.2. Out of those 8 pairs, the Chalmers algorithm was successfully ran on two of them; two pairs of RCM satellite images with a 10 m resolution, over buoys 6817, 6795 (Floe 2), and 9591 (Floe 4). The drift estimates were obtained from these high resolution images using the following parameters values :

- grid step = 50 [m]
- image resolution = 10 [m]
- max speed = 0.4 [m.s^{-1}]
- max block size = 1e5 [pixels]

The working images were captured on June 6, 2023, at 07:33:16 and 16:02:53 (Estimate No.1) and 07:01:28 and 16:02:53 (Estimate No.2). The 6 other images pairs which were not successfully processed by the Chalmers algorithm were S1A images with a resolution of 100 m - 150 m. The algorithm outputs (presented in the form of drift vectors), and a summary statistics for these two estimates are presented in Figures 5.14, Figure 5.15, and Table D.1, and Figure 5.16, Figure 5.17, and Table D.2, respectively. The algorithm produces drift vectors at locations where it was able to successfully identify and track the floes in the two consecutive images. The tables in Appendix D compare the direction and magnitude of the buoys' drift to those of the algorithm's closest drift vector to each buoy, as well as to the average drift vectors within a 5 km radius around the buoys. In Estimate No.2, the earliest image of the satellite image pair was collected 30 minutes before the earliest image in the pair used for Estimate No.1, thus Estimate No.2 is expected to represent the continuity of Estimate No.1. In the two estimates, the azimuth angle of the drift is almost identical, about 162°. Given that the three in situ measurements are located within a radius of about 3 km, the average speed and direction of these measurements is presented against the average speed and direction of the closest drift vector and the drift vectors within a 5 km radius. This is done assuming that the drift field is approximately homogeneous within a length scale of 5 km.

There are two major sources of uncertainty that should be considered when validating the performance of the Chalmers algorithm against our in situ buoy measurements. The GPS inaccuracy of 4-6 m, as well as the buoy to image time gap of each buoy. The greater the buoy to image time gap, the less representative of the actual drift the buoy measurement becomes. In this report, the specific buoy to image time difference is not considered. Instead, the maximum time gap of 5 minutes is considered. Given that on those dates, the buoys drifted at a speed of maximum 0.2 m.s^{-1} (see Section 5.3 and Appendix C), an uncertainty of 120 m shall be considered when comparing the drift distance from the drift vectors to the actual drift distance (assuming that the time gap is of 5 minutes between the buoy and each of the satellite image). This uncertainty on the drift distance impacts the uncertainty on the direction as well. Given that the drift distance of the buoys is

around 3 km, the uncertainty of 120 m on the position results in an uncertainty of 1.8-2° in the direction (calculations not shown). Those uncertainties are reported in Figures 5.15 and Figure 5.17.

Regarding the drift distance; in Estimate No.1, the buoys drifted on average about 3566 m in 8 hours and 30 minutes. On average, the drift distance of the closest vector to each buoy is 3649 m, and the average drift distance of the drift vectors within a 5 km radius of the buoys is approximately 4004 m. Estimate No.2, the buoys drifted on average about 3856 m in 9 hours. On average, the drift distance of the closest vector to each buoy is 4487 m, and the average drift distance of the drift vectors within a 5 km radius of the buoys is approximately 4507 m. The closest drift vectors overestimate the average of the actual drift of the buoys by 68 m (9%) in Estimate No.1, and by 363 m (10%) in Estimate No.2. When considering the average of the drift vectors within 5 km of the buoys, the algorithm overestimates the actual drift by about 438 m (12.5%) in Estimate No.1 and 650 m (16.8%) in Estimate No.2.

Regarding the azimuth angle, in Estimate No.1, the buoys' azimuth angle is about 156°. On average, the azimuth angle of the closest vector to each buoy is 162°, and the average azimuth angle of the drift vectors within a 5 km radius of the buoys is approximately 161°. Estimate No.2, the buoys' average azimuth angle is about 158°. On average, the azimuth angle of the closest vector to each buoy is about 163°, and the average azimuth angle of the drift vectors within a 5 km radius of the buoys is approximately 162°. The closest drift vectors overestimate the average of the actual azimuth angle of the buoys by 6° (4%) in Estimate No.1, and by 5° (3%) in Estimate No.2. When considering the average of the drift vectors within 5 km of the buoys, the algorithm overestimates the actual direction by about 5° (3%) in Estimate No.1 and 4° (3%) in Estimate No.2.

Drift Estimate No.1:

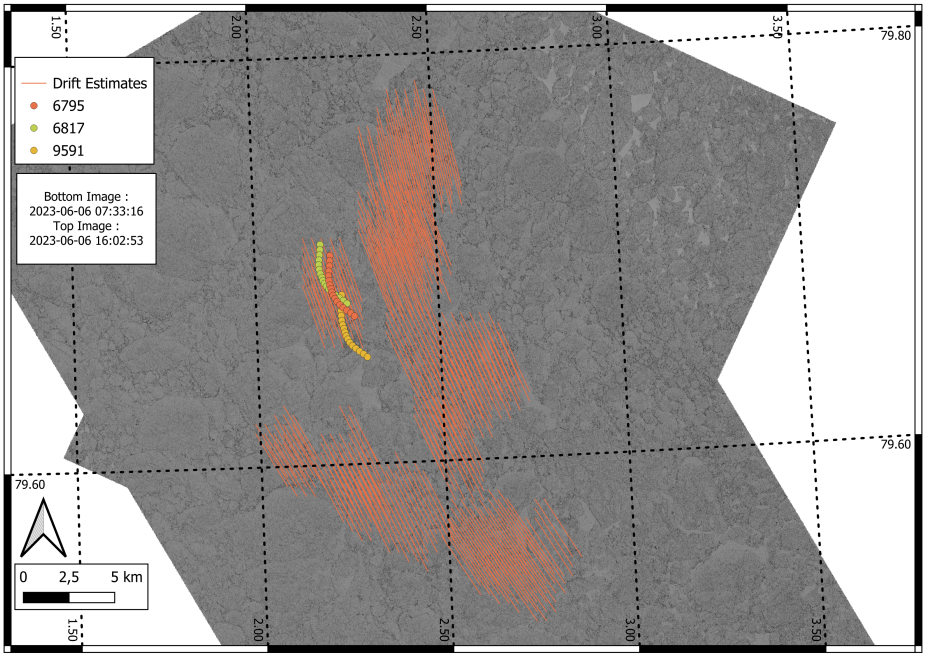

Figure 5.14: Chalmers algorithm drift Estimate No.1 using RCM satellite images with a resolution of 10 m. Image 1 (bottom): 2023-06-06 07:33:16. Image 2 (top): 2023-06-06 16:02:53. The time difference between the two images is 8 hours, 29 minutes, and 37 seconds.

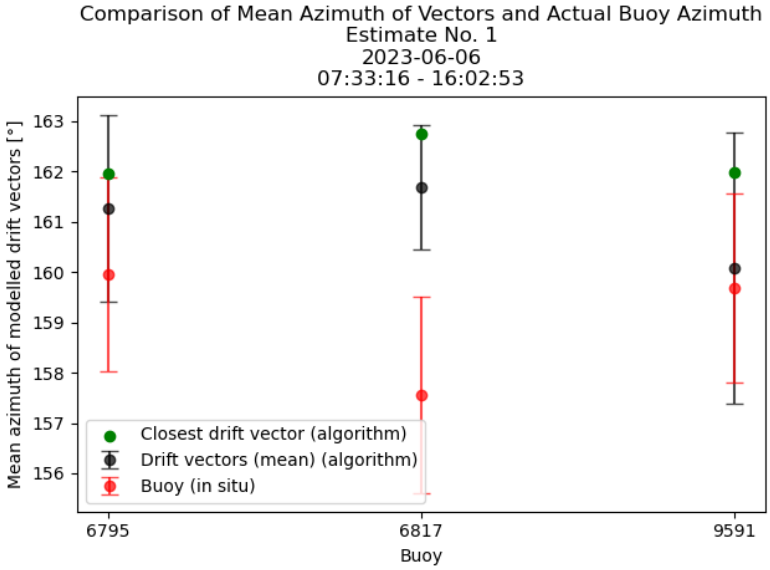

(a)

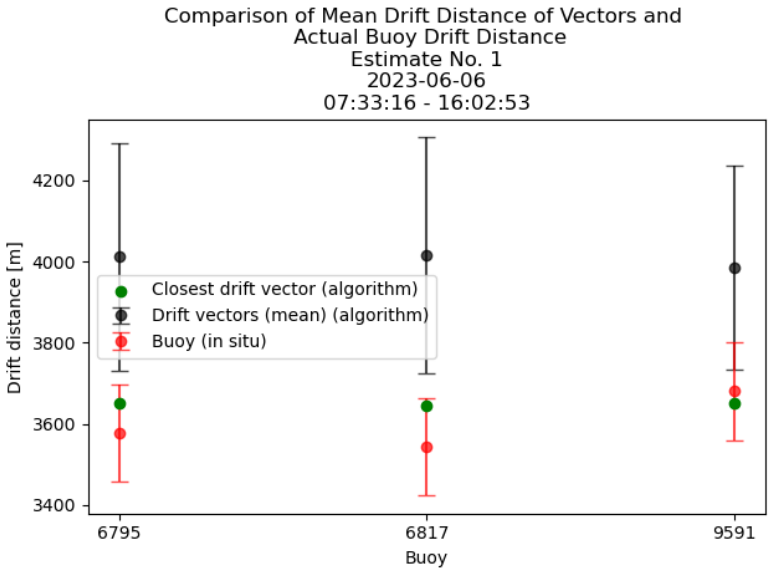

(b)

Figure 5.15: Summary statistics for Estimate No. 1, comparing drift vector and in situ measurements. (a) Azimuth direction, (b) Drift distance

Drift Estimate No.2:

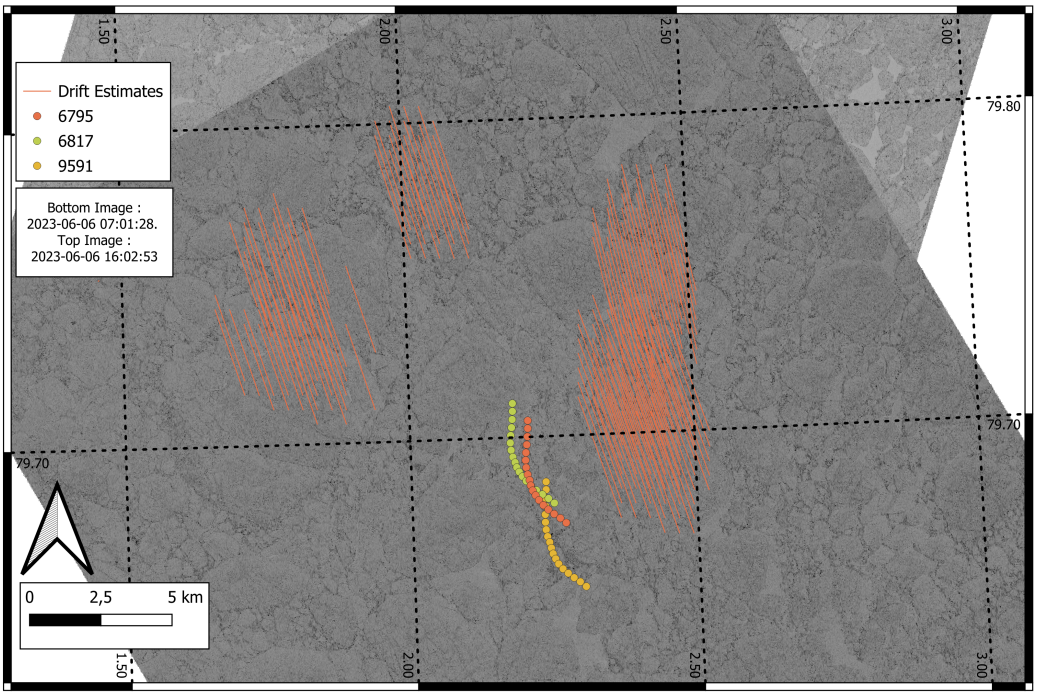

Figure 5.16: Chalmers algorithm drift Estimate No.2: using RCM satellite images with a resolution of 10 m. Image 1 (bottom): 2023-06-06 07:01:28. Image 2 (top): 2023-06-06 16:02:53. The time difference between the two images is 9 hours, 1 minute, and 25 seconds.

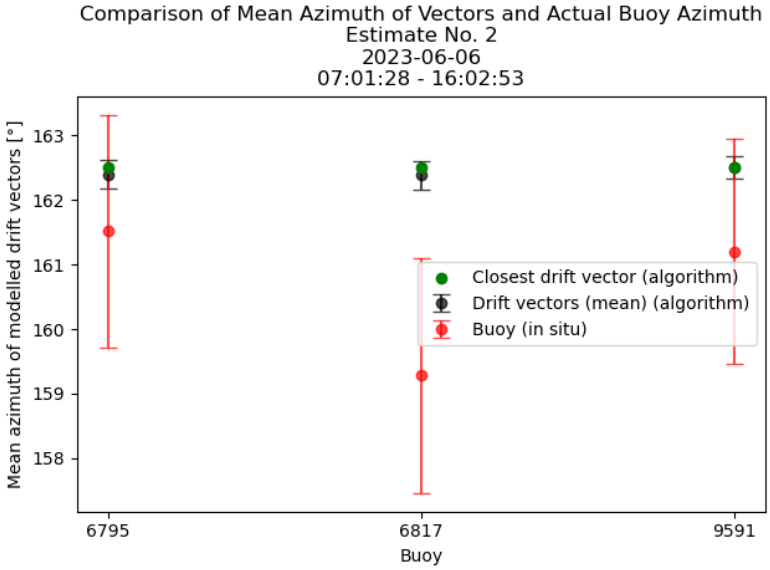

(a)

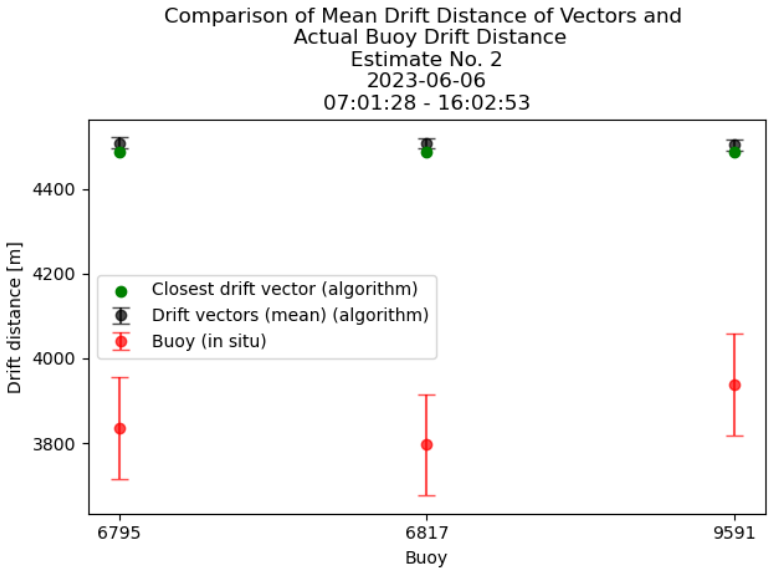

(b)

Figure 5.17: Summary statistics for Estimate No. 2, showing mean and standard deviation of drift vectors. (a) Azimuth direction, (b) Drift distance

5.3 Waves analyses

The wave data presented hereafter include wave spectra (in Hertz), significant wave height (in meters), and wave period (in seconds). To fully interpret the wave measurements, they must be contextualized with the wind, ocean and ice conditions. Therefore, the wave data is presented alongside the heading direction and speed of buoys and wind, and with references to satellite images presented in the report. Given that a total of seven wave data sets were obtained - one for each OpenMET buoy, two of them are presented hereafter; 9064 and 6817, as they were placed on Floe 1 and Floe 2, respectively, and convey complementary information about the wave - ice interaction on the floes throughout their drift. The wave data of the other buoys are presented in Section C

Buoy 9064: Figure 5.18 presents the wave spectra, wave height and wave period measured by the OpenMET buoys 9064, along with the buoy speed and direction measured by the buoy, and the CARRA reanalysis wind data. The two dates marked with *"Strong waves"* and the one marked with *"No waves"* in the wave spectra plot refer to the relatively strong wave conditions on May 24th and May 26th presented in Figures 5.5a and Figure 5.19a, respectively, and the relatively weak wave conditions on June 2nd presented in Figure 5.19b. On May 24^{th}, the ERA reanalysis model indicates waves up to 1.5-2 m high directed towards the edge of the MIZ where all four buoys of Floe 1 were located. On May 26th, it indicates waves about 3-4 m high directed towards north-east. The buoy and wind speed and heading are displayed to assess their correlation, and estimate whether the motion of the buoy was mostly driven by the wind, or by the ocean currents.

Figure 5.19 shows two S1A images taken over Floe 1 on May 24^{th} (Figure 5.19a) and June 2^{nd} (Figure 5.19b), at times when the wave conditions were significantly different. On May 24^{th}, there were waves about 2-3 m high directed directly toward Floe 1. On June 2^{nd}, there were almost no waves.

Buoy 6817: Figure 5.20 presents the wave spectra, wave height, and wave period measured by the OpenMET buoys 6817, along with the buoy speed and direction measured by the buoy, and the CARRA reanalysis wind data. These figures must be put in relation to the satellite images showing when the buoy transited from drifting in the MIZ to the open ocean on June 13^{th} in Figure 5.11, and the drift conditions on June 17 shown in Figure 5.10b, when the buoy was drifting in the open ocean.

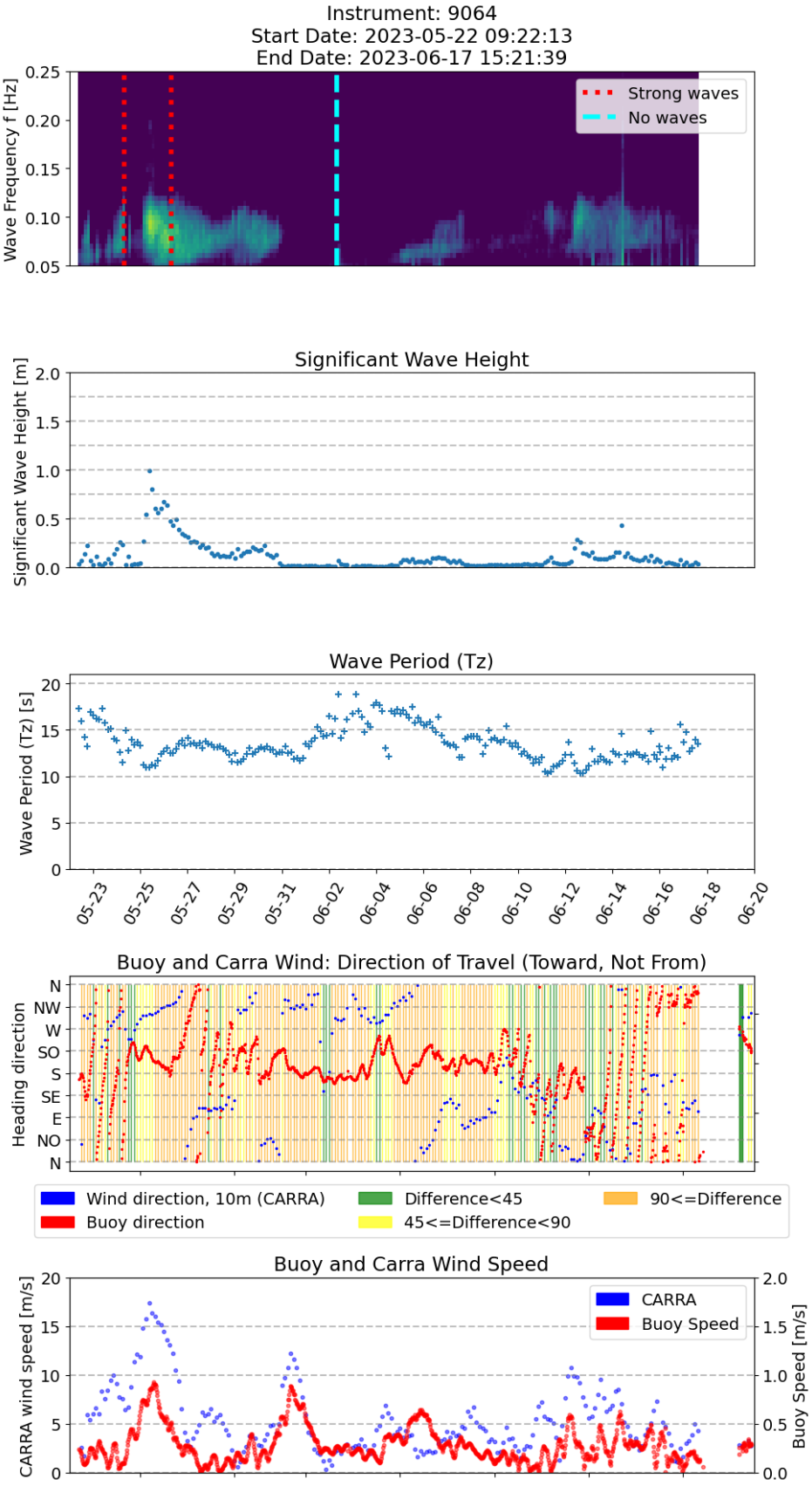

Figure 5.18: Wave spectra of buoy 9064. May 24th and 26th are labeled "Strong waves", and June 2nd is labeled "No Waves" as seen in the wave reanalysis data presented in Figures 5.5a, Figure 5.19a, and Figure 5.19b, respectively.

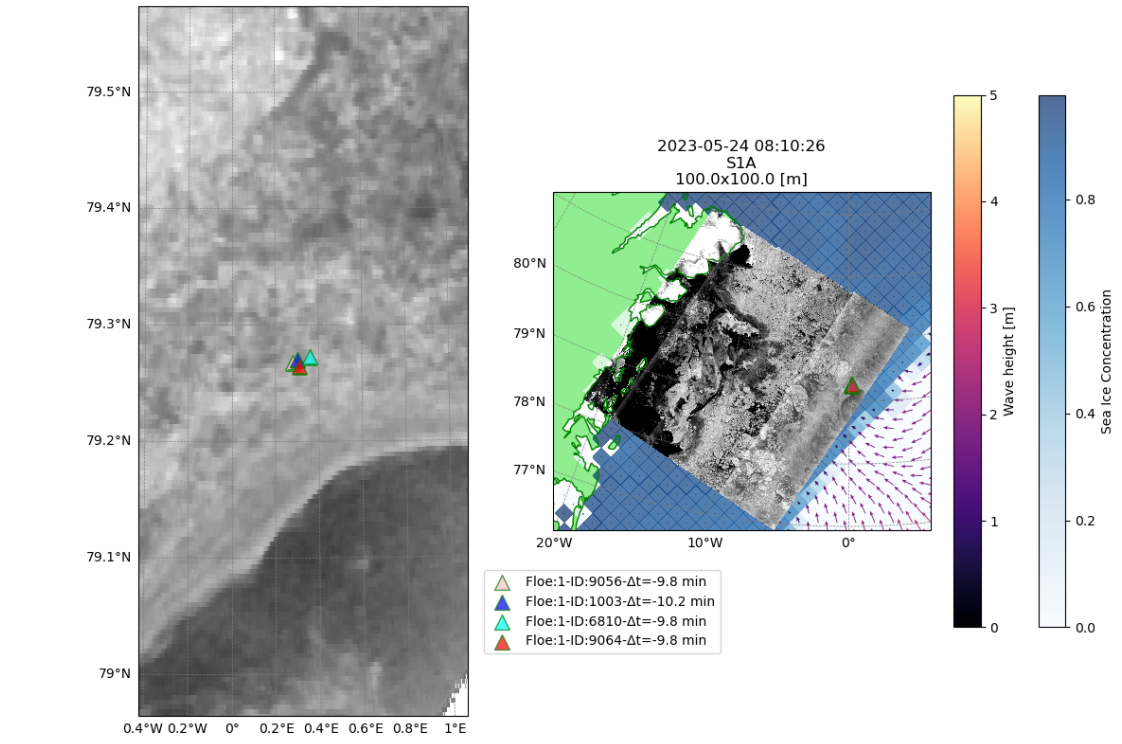

(a)

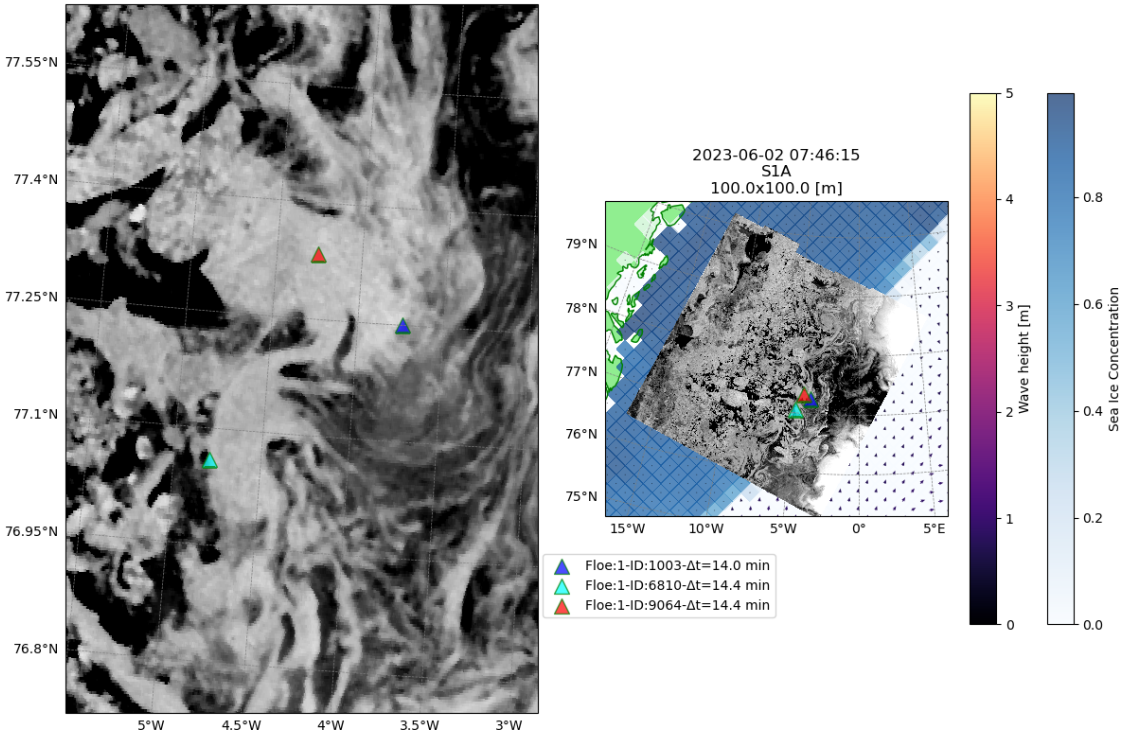

(b)

Figure 5.19: **a)** On May 24^{th}, there were waves about 2-3 m high directed directly toward Floe 1. **b)** On June 2^{nd}, there were almost no waves.

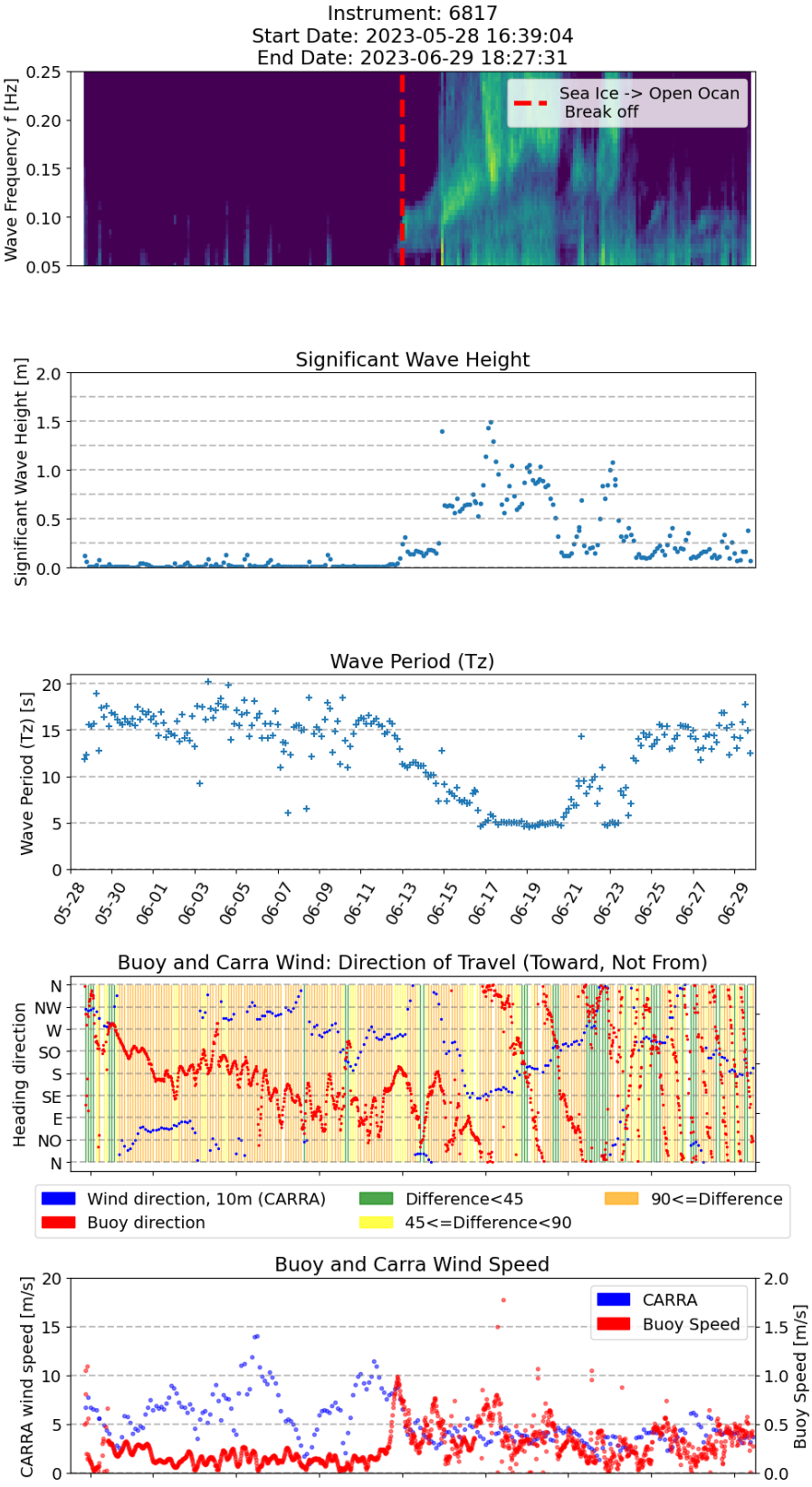

Figure 5.20: Waves spectra of buoy 6817. The red dashed line indicates when the buoy transited from drifting in the MIZ and in the open ocean on June 13^{th} (5.11) and the breaking of the floe.

6

Discussion

The weather data available on May 21^{st} from WS1 (Appendix A.1) and the CARRA reanalysis data (Figure 3.2) indicate southern winds of up to 12.5 m.s^{-1} (strong breeze) on that day. Therefore, the onset of the breakup of Floe 1 reported by the crew onboard Oden on this day cannot be attributed to any particularly strong weather event upon inspection of the available weather data. The inter-buoy distances on Floe 1 remained stable for a total of 6 hours from the first data reception on May 22^{nd} before they began to drift apart, as they followed a circular drift pattern. Among the numerous observations of the buoy trajectories presented in this report, two significant observations underline the complex nature of the drift in the MIZ. First, on May 26^{th}, when 6810 drifted apart from buoys 1003 and 9064 (Figure 5.4), while the latter two remained close to each other despite being on separate floes, and then drifted apart the following day. The fact that buoys 1003 and 9064 had already separated on May 26^{th} is shown in the inter-buoy distance plot (Figure 5.2), indicating that the buoys have separated on May 22^{nd} in the afternoon. Second, the observation of the drift of buoys 6795 and 6817 (Figure 5.9), which on June 18^{th} followed a completely different trajectory; 6817 became entangled in a swirling motion, while 6795 continued heading north. The chaotic nature of the sea ice conditions in the MIZ is evident in the satellite images (e.g., Figure 5.5, Figure 5.10) from the significant brightness variations.

The deformation and the rotation rates of Floe 1 (Figure 5.6) must be interpreted keeping in mind that the floe had already disintegrated on May 22^{nd}. Therefore, a positive divergence means that the dislocated buoys were drifting apart from each other. A negative divergence indicates the convergence of the buoys toward each other. From May 22^{nd} to 24^{th}, the buoys were caught in the circular drift pattern, which accounts for the observed alternating convergence and divergence of the buoys relative to each other under these particular drift conditions. Given that Floe 1 had disintegrated, the shear results shall not be considered for analysis. The deformation and rotation rates of Floe 2 (Figure 5.12) must be interpreted knowing that the buoys still held together on Floe 2 at the dates represented in the corresponding plots. Floe 2 appears to have rotated between 650 degrees.day^{-1} and almost 900 degrees.day^{-1}. Such rotation rates shall be compared to other observations from other expeditions. According to M. Leppäranta [4], in the Ice Kinematics chapter, rotation of the floes "may occasionally be fast". He mentions the work of Gorbunov and Timokhov (1968) in the Chukchi Sea on floes' rotation, which indicated that in a fragmented ice field, floes smaller than about 200 m typically rotated at rates between 720 degrees.day^{-1}, up to 2400 degrees.day^{-1}. Given that Floe 2 drifted in

the MIZ, where the ice field is fragmented, its rotation rate falls within the range reported by Gorbunov and Timokhov.

The wave data measured by buoy 9064 (5.18) present a wave spectrum that is characteristic for a buoy placed on a solid ice floe (phase (A)). On the dates marked as "Strong waves" (May 24th and 26th), the behavior of the ice floe as an effective dampener of high-frequency waves is evident. Although on May 26^{th} the waves from the reanalysis model were not directed towards the buoy, it was when the buoy measured its strongest wave signal and the buoy speed. It follows a Gale which occurred on May 25^{th} coming from the south-west as indicated by the CARRA wind speeds up to 17 m.s^{-1} on that day. This Gale was also reported by the Oden crew, who noted that it contributed to the breaking of large floes. When on the 24^{th} and 26^{th}, the reanalysis wave data indicated waves about 1.5-2 m high directed towards the buoys and 3-4 m high directed towards the north-west, the buoy measured waves heights of about 0.25 m and 0.70 m, respectively. On June 2^{nd}, the wave reanalysis data showed practically no waves at all. This is coherent with the buoy having measured no waves signal on that day. Throughout its existence, buoy 9064 only very briefly recorded wave data typical for a buoy drifting on a small individual floe (phase (B)), maybe in the open ocean (phase (C)); where the whole range of wave frequencies is expected to be recorded by the buoy. This occurred very shortly on June 14th, perhaps suggesting that buoy 9064 sank after the progressive decay of its floe. In general, as the wave height increases, the wave period is shorter, as expected.

The wave spectrum of buoy 6817 (Figure 5.20) presents the characteristics of a buoy in the three phases. From its deployment until June 13^{th}, the wave spectrum is indicative of a buoy on a solid ice floe (phase (A)). At those dates, the buoy progressed from the core of the MIZ to the edge and traveled a daily distance of about 10 km.day^{-1} to 20 km.day^{-1} (Figure B.3). The buoy was shielded by the dense ice cover surrounding it when a Near-Gale occurred on June 6^{th}, as indicated by the CARRA wind speeds of approximately 14 m.s^{-1} on that day. The great capacity of the ice floes in filtering the high-frequency waves is clearly observable from the weak low-frequency wave signals measured during this period. On June 13^{th}, buoy 6817 both broke off from buoy 6795, and started to transit from drifting in the middle of other ice floes in the MIZ to drifting in the open ocean (Figure 5.11. This transition coincides with the buoy's highest daily distance traveled, ranging from approximately 20 km.day^{-1} to 60 km.day^{-1} (Figure B.3). At this stage, the buoy recorded more high-frequency waves, but continues to filter out high-frequency waves until June 15^{th}, where the floe appears to have completely disintegrated in the open ocean. This is suggested by the observation that wave frequencies were recorded throughout the frequency range and coincides with the satellite image showing the buoy drifting in the open ocean on June 17^{th} (Figure 5.10b)). Finally, from June 24^{th}, the buoy no longer recorded a wave spectrum characteristic to a buoy drifting in open water, although there was no drastic changes in wind conditions compared to during the "drift in open ocean" phase. Therefore the lack of high-frequency waves measurements cannot be attributed to weaker wind and waves conditions. Upon inspection of a satellite image capturing the buoy on June 30^{th}, the buoy was located

in the vicinity of the MIZ again. Maybe the proximity to other floes shielded the buoy from high frequency waves until it ceased functioning.

A similar interpretation of the main features of the wave data can be made for the remaining buoys, whose wave data is presented in Appendix C. Overall, there is a poor agreement between the heading direction of the reanalyses wind and the buoy, even when the floes are drifting in open water and should not be obstructed by neighboring ice floes. This can be partly attributed to the relatively lower wind data resolution (3 hours) compared to that of the positions sensors of the buoys (30 minutes) and the contribution of the ocean currents.

The daily distance traveled by each buoy ranges from 10 km.day^{-1} to 60 km.day^{-1} and is presented in Appendix B.

The Chalmers algorithm was successfully run on two pairs of high-resolution (10 m) RCM images, taken on June 6, 2023, between 07:33:16 and 16:02:53 (Figure 5.14) and 07:01:28 and 16:02:53 (Figure 5.16). The drift estimates for these two pairs are referred to as Estimate No.1 and Estimate No.2, respectively. The estimates are produced using two satellite images taken over the same area, at a different time. Thus, the images in the pair will be designated as the "preceding" and "following" images. Given that the two estimates were produced using the same "following" image, and that their "preceding" image has only about 30 minutes time difference, that no significant shift in the weather conditions can be observed from the weather data on this day, and that the two estimates are independent from each other, we expect to see coherency in the azimuth direction and drift distance of the two estimates; Estimate No.2 is expected to follow the path of Estimate No.1. This is corroborated by the fact that the azimuth direction of the drift vectors remained constant between the two estimates. Regarding the drift distance, it may be more intuitive to discuss it in terms of the buoy speed rather than distance estimation. Although the algorithm tends to overestimate the drift distance compared to the actual drift from the buoy measurements, the buoy speed that would correspond to those overestimated displacements would be 0.1-0.2 m.s^{-1}. The actual drift speed of the buoy falls within this same range. Therefore, despite not matching the buoy drift distance exactly, the algorithm succeeded in providing realistic estimations. According to the buoy speed measurements presented along the waves results, drift speeds greater than 2 m.s^{-1} would have been considered unrealistic.

It is important to consider the implications of evaluating the Chalmers algorithm performance in estimating the actual sea ice drift by comparing the average in situ measurements within a 5 km radius to both the average of the closest drift vectors and the average of all drift vectors within the same radius. Indeed, the drift field is not perfectly homogeneous, therefore, a perfect agreement between the drift vectors and the in situ measurements shall not be expected. Moreover, the time difference between the buoy and the satellite images is a major source of discrepancy between the algorithm outputs and the actual drift. In this report, the buoy to image time gap of 5 minutes is considered, with a drift speed of 0.2 m.s^{-1}. This results in a dis-

placement uncertainty of about 120 m (in the case where the buoy has a 5 minutes time difference with both satellite images in the pair). One could have decided to display the uncertainty associated with the specific time gap between each buoy and the total time difference with the two satellite images of the considered pair, but the choice of representing the worst-case scenario was made instead because our analyses focuses on two estimates only, which is not statistically significant. The resulting uncertainties in the drift distance and azimuth direction of the buoys is shown in Appendix D. Although the actual buoy drift does not always fall within the standard deviation of the azimuth direction and drift distance of the drift vectors (see Appendix D), the Chalmers algorithm performance remains reasonably promising. For a more accurate and statistically significant evaluation of the Chalmers algorithm' performance, it should be investigated on a larger number of image pairs. In this report, a total of eight image pairs was retrieved based on the filtering conditions cited in Section 4.2, but only two pairs of RCM images were successfully processed. The remaining image pairs were S1A images with a resolution of 100-150 m. Further work should be carried out in order to include these image pairs in the evaluation of the Chalmers algorithm. The reason the S1A images were not successfully processed remains unclear to this day, despite attempts to adjust parameters (block size, grid step, image resolution, max speed, and max block size). The tested parameter values in these attempts are not shown in this report. Next, further work could include testing the Chalmers algorithm performances on image pairs where the time gap between the buoys and the images is greater than 5 minutes, and where the time gap between the images in the pair is greater than 24 hours. The risk of increasing the buoy / image time gap is that the corresponding buoy drift will become less representative of the actual sea ice drift. The risk of increasing the time gap between the satellite images is that as this time gap increases, the ice floes become more deformed, and may not be present in the overlapping region between the images, thus reducing the ability of the Chalmers algorithm to detect and track the sea ice floes from one image to the next.

The damage to buoy 1001 caused by a polar bear encounter, which required the crew to retrieve it and repair it onboard Oden before redeploying by helicopter, the unexpectedly heavy ice conditions that prevented the ship from traveling further north as initially planned, and the heavy weather conditions which contributed to breaking the floes earlier than anticipated, exemplify the difficulties associated with carrying out fieldwork in the polar regions.

7
Conclusion

The aims of this Master's thesis work was to analyse in situ sea ice dynamics data, including drift data and waves spectra, measured from buoys deployed on sea ice floes during the Art of Melt 2023 expedition, and use the in situ drift data to validate sea ice drift estimates made by the Chalmers algorithm. The time period considered for the analyses was May-July 2023.

The in situ sea ice drift and waves data from the buoys was successfully retrieved. It permitted analyses of the floes' trajectory and progressive break-up and melting throughout the drift. Combining drift data, wave spectra, satellite imagery, and weather data from in situ and reanalysis models allowed for the reconstruction of the floes' decay, and contextualizing it with weather, ocean, and surrounding ice conditions. The complex nature of sea ice drift in the marginal ice zone was observed from the large variation in daily distance travelled by the buoys, and from the drift patterns of single buoys after they broke off from the floe on which they were initially deployed. The wave spectra measured from the buoys were coherent with the drift of the floes and the weather conditions, whether in the middle of the MIZ, where the floes acted as effective high-frequency waves filters, or in the open ocean, where they were subjected to both high- and low-frequency waves.

The sea ice drift and waves data collected by the buoys during this expedition will contribute to an open source sea ice, integrating data from various contributors over the period 2022-2023 [82]. This new data set builds upon [81].

The Chalmers drift algorithm was successfully ran on two pairs of RCM images with a resolution of 10 m, out of a total of 8 image pairs. The image pairs were filtered from all the RCM and S1A images available as follow; the respective time gap between the two images is within 1-24 hours, they both captured the same buoy, they have the same resolution, the buoy / image time gap is of at most 5 minutes. The six remaining pairs contained S1A images with a resolution of 100-150 m. The two satellite images of the retrieved pairs can be labelled the "earlier" and "later image". The working RCM pairs happened to have their later image in common, and the image taken earlier to have a 30 minutes time gap with that of the other pair, allowing for assessing the quality of the Chalmers algorithm by examining the consistency of the estimated drift fields across the two estimates.

Although the two drift estimates obtained from the Chalmers algorithm are not statistically significant, they demonstrate the ability of the Chalmers algorithm in

producing coherent realistic drift estimates. This is suggested by the consistency in the azimuth direction of the drift vectors with the actual buoys' drift, as well as the realistic sea ice drift distances compared to the buoys' measurements. However, in order to evaluate better the performance of the Chalmers algorithm it shall be tested on a larger dataset, including the six remaining S1A image pairs, and pairs with a larger time gap.

The reason why the S1A images were not correctly processed by the Chalmers algorithm remains unclear to this day. Further work should aim to successfully run the Chalmers algorithm on the S1A image pairs. This would enable more statistically significant analyses on the Chalmers drift algorithm's performance. Additionally, it would be valuable to experiment with the effects of increasing the time gap between the buoy and the satellite images, and increasing the time separation between the two satellite images, to gain further insight into the algorithm's capacities.

Bibliography

[1] Mohammed Shokr and Nirmal K Sinha. Sea ice: physics and remote sensing. John Wiley & Sons, 2023.

[2] Sascha Schiøtt, Pelle Tejsner, and Søren Rysgaard. Inuit and local knowledge on the marine ecosystem in Ilulissat Icefjord, Greenland. In: *Human Ecology* (2022), pp. 1–15.

[3] Gita J Laidler et al. Travelling and hunting in a changing Arctic: Assessing Inuit vulnerability to sea ice change in Igloolik, Nunavut. In: *Climatic change* 94 (2009), pp. 363–397.

[4] Matti Leppäranta. The drift of sea ice. Springer Science & Business Media, 2011.

[5] PA Berkman et al. Satellite record of Pan-Arctic maritime ship traffic. In: (2022).

[6] Willy Ostreng et al. Shipping in Arctic waters: a comparison of the Northeast, Northwest and trans polar passages. Springer Science & Business Media, 2013.

[7] Gary A Maykut. Energy exchange over young sea ice in the central Arctic. In: *Journal of Geophysical Research: Oceans* 83.C7 (1978), pp. 3646–3658.

[8] Cecilie Mauritzen and Sirpa Häkkinen. Influence of sea ice on the thermohaline circulation in the Arctic-North Atlantic Ocean. In: *Geophysical Research Letters* 24.24 (1997), pp. 3257–3260.

[9] Lars Chresten Lund-Hansen et al. Arctic sea ice ecology. Springer, 2020.

[10] Rubao Ji, Meibing Jin, and Øystein Varpe. Sea ice phenology and timing of primary production pulses in the Arctic Ocean. In: *Global change biology* 19.3 (2013), pp. 734–741.

[11] Kevin R Arrigo and Gert L van Dijken. Continued increases in Arctic Ocean primary production. In: *Progress in oceanography* 136 (2015), pp. 60–70.

[12] R Colony and AS Thorndike. An estimate of the mean field of Arctic sea ice motion. In: *Journal of Geophysical Research: Oceans* 89.C6 (1984), pp. 10623–10629.

[13] Gunnar Spreen et al. Arctic sea ice volume export through Fram Strait from 1992 to 2014. In: *Journal of Geophysical Research: Oceans* 125.6 (2020), e2019JC016039.

[14] Bert Rudels, Hans J Friedrich, and Detlef Quadfasel. The Arctic circumpolar boundary current. In: *Deep Sea Research Part II: Topical Studies in Oceanography* 46.6-7 (1999), pp. 1023–1062.

[15] Arctic Monitoring and Assessment Programme (AMAP). Snow, Water, Ice and Permafrost in the Arctic (SWIPA) 2017. Oslo, Norway: Arctic Monitoring and Assessment Programme (AMAP), 2017, pp. xiv + 269. ISBN: 978-82-7971-101-8.

[16] Gunnar Spreen, Ron Kwok, and Dimitris Menemenlis. Trends in Arctic sea ice drift and role of wind forcing: 1992–2009. In: *Geophysical Research Letters* 38.19 (2011).

[17] Pierre Rampal, Jérôme Weiss, and David Marsan. Positive trend in the mean speed and deformation rate of Arctic sea ice, 1979–2007. In: *Journal of Geophysical Research: Oceans* 114.C5 (2009).

[18] David G Barber and Ellsworth F LeDrew. Modeling synthetic aperture radar (SAR) scattering from a seasonally varying snow-covered sea ice volume at 5.3 and 9.25 GHz. In: *Polar research* 13.1 (1994), pp. 35–54.

[19] Xue Wang et al. An intercomparison of satellite derived Arctic sea ice motion products. In: *Remote Sensing* 14.5 (2022), p. 1261.

[20] Anders Berg and Leif EB Eriksson. Investigation of a hybrid algorithm for sea ice drift measurements using synthetic aperture radar images. In: *IEEE Transactions on Geoscience and Remote Sensing* 52.8 (2013), pp. 5023–5033.

[21] Jean Rabault et al. Openmetbuoy-v2021: An easy-to-build, affordable, customizable, open-source instrument for oceanographic measurements of drift and waves in sea ice and the open ocean. In: *Geosciences* 12.3 (2022), p. 110.

[22] Keith Jackson et al. A novel and low-cost sea ice mass balance buoy. In: *Journal of Atmospheric and Oceanic Technology* 30.11 (2013), pp. 2676–2688.

[23] Paul G Huray. Maxwell's equations. John Wiley & Sons, 2009.

[24] Hai Liu et al. Penetration properties of ground penetrating radar waves through rebar grids. In: *IEEE Geoscience and Remote Sensing Letters* 18.7 (2020), pp. 1199–1203.

[25] Shefali Aggarwal. Principles of remote sensing. In: *Satellite remote sensing and GIS applications in agricultural meteorology* 23.2 (2004), pp. 23–28.

[26] Valentin Ludwig, Gunnar Spreen, and Leif Toudal Pedersen. Evaluation of a new merged sea-ice concentration dataset at 1 km resolution from thermal infrared and passive microwave satellite data in the Arctic. In: *Remote Sensing* 12.19 (2020), p. 3183.

[27] William L Barnes, Xiaoxiong Xiong, and Vincent V Salomonson. Status of terra MODIS and aqua MODIS. In: *Advances in Space Research* 32.11 (2003), pp. 2099–2106.

[28] Wolfgang Dierking. Sea ice monitoring by synthetic aperture radar. In: *Oceanography* 26.2 (2013), pp. 100–111.

[29] Fabrice Collard, Fabrice Ardhuin, and Bertrand Chapron. Extraction of coastal ocean wave fields from SAR images. In: *IEEE Journal of Oceanic Engineering* 30.3 (2005), pp. 526–533.

[30] Denis Demchev et al. Sea ice drift tracking from sequential SAR images using accelerated-KAZE features. In: *IEEE Transactions on Geoscience and Remote Sensing* 55.9 (2017), pp. 5174–5184.

[31] Maofei Jiang et al. Estimation of Arctic Sea Ice thickness from Chinese HY-2B radar altimetry data. In: *Remote Sensing* 15.5 (2023), p. 1180.

[32] Rosemary Morrow et al. Ocean circulation from space. In: *Surveys in Geophysics* 44.5 (2023), pp. 1243–1286.

[33] Panagiotis Mitsopoulos and Malaquias Peña. Characterizing Coastal Wind Speed and Significant Wave Height Using Satellite Altimetry and Buoy Data. In: *Remote Sensing* 15.4 (2023), p. 987.

[34] Christian Melsheimer et al. First results of Antarctic sea ice type retrieval from active and passive microwave remote sensing data. In: *The Cryosphere* 17.1 (2023), pp. 105–126.

[35] Fanny Girard-Ardhuin and Robert Ezraty. Enhanced Arctic sea ice drift estimation merging radiometer and scatterometer data. In: *IEEE Transactions on Geoscience and Remote Sensing* 50.7 (2012), pp. 2639–2648.

[36] Firouz M Naderi, Michael H Freilich, and David G Long. Spaceborne radar measurement of wind velocity over the ocean-an overview of the NSCAT scatterometer system. In: *Proceedings of the IEEE* 79.6 (1991), pp. 850–866.

[37] Dyre O Dammann et al. Mapping Pan-Arctic landfast sea ice stability using Sentinel-1 interferometry. In: *The Cryosphere* 13.2 (2019), pp. 557–577.

[38] Temesgen Gebrie Yitayew et al. Validation of Sea-Ice Topographic Heights Derived From TanDEM-X Interferometric SAR Data With Results From Laser Profiler and Photogrammetry. In: *IEEE Transactions on Geoscience and Remote Sensing* 56.11 (2018), pp. 6504–6520. DOI: 10.1109/TGRS.2018.2839590.

[39] R Kwok et al. Sea ice motion from satellite passive microwave imagery assessed with ERS SAR and buoy motions. In: *Journal of Geophysical Research: Oceans* 103.C4 (1998), pp. 8191–8214.

[40] C Fowler, W Emery, and M Tschudi. *Polar Pathfinder daily 25 km EASE-grid sea ice motion vectors*. 2003.

[41] OSI SAF. *Low resolution sea ice drift product of the EUMETSAT Ocean and Sea Ice Satellite Application Facility.[Dataset]*. 2021.

[42] R Saldo. Global ocean-high resolution SAR sea ice drift. In: *Copernicus Marine Service [data set]* 10 (2020).

[43] Stefan Kern and Burcu Ozsoy. Remote Sensing. In: May 2018.

[44] Kristina B Katsaros et al. Albedo of a water surface, spectral variation, effects of atmospheric transmittance, sun angle and wind speed. In: *Journal of Geophysical Research: Oceans* 90.C4 (1985), pp. 7313–7321.

[45] Wiebke Margitta Kolbe, Rasmus Tage Tonboe, and Julienne Stroeve. Mapping of sea ice concentration using the NASA NIMBUS 5 ESMR microwave radiometer data 1972–1977. In: *Earth System Science Data Discussions* 2023 (2023), pp. 1–26.

[46] Julienne Stroeve and Dirk Notz. Changing state of Arctic sea ice across all seasons. In: *Environmental Research Letters* 13.10 (2018), p. 103001.

[47] James Maslanik et al. Distribution and trends in Arctic sea ice age through spring 2011. In: *Geophysical Research Letters* 38.13 (2011).

[48] Thorsten Markus, Julienne C Stroeve, and Jeffrey Miller. Recent changes in Arctic sea ice melt onset, freezeup, and melt season length. In: *Journal of Geophysical Research: Oceans* 114.C12 (2009).

[49] David N Thomas. Sea ice. John Wiley & Sons, 2017.

[50] Mats A Granskog et al. Superimposed ice formation and surface energy fluxes on sea ice during the spring melt–freeze period in the Baltic Sea. In: *Journal of Glaciology* 52.176 (2006), pp. 119–127.

[51] ME Johnston. Seasonal changes in the properties of first-year, second-year and multi-year ice. In: *Cold Regions Science and Technology* 141 (2017), pp. 36–53.

[52] Mohammed E Shokr and Nirmal K Sinha. Arctic sea ice microstructure observations relevant to microwave scattering. In: *Arctic* (1994), pp. 265–279.

[53] Robert G. Onstott and Robert A. Schuman. NOAA SAR Manual. Synthetic Aperture Radar Marine User's Manual, 2004. Chap. Chapter 3: SAR Measurements of Sea Ice, pp. 81–116.

[54] Stephen G Warren. Optical properties of snow. In: *Reviews of Geophysics* 20.1 (1982), pp. 67–89.

[55] Polona Itkin et al. Thin ice and storms: Sea ice deformation from buoy arrays deployed during N-ICE 2015. In: *Journal of Geophysical Research: Oceans* 122.6 (2017), pp. 4661–4674.

[56] Alan S Thorndike. Kinematics of sea ice. In: *The geophysics of sea ice*. Springer, 1986, pp. 489–549.

[57] Vernon A Squire. Ocean wave interactions with sea ice: A reappraisal. In: *Annual Review of Fluid Mechanics* 52.1 (2020), pp. 37–60.

[58] Christine Provost et al. Observations of flooding and snow-ice formation in a thinner A rctic sea-ice regime during the N-ICE 2015 campaign: Influence of basal ice melt and storms. In: *Journal of Geophysical Research: Oceans* 122.9 (2017), pp. 7115–7134.

[59] Guillaume Boutin et al. Towards a coupled model to investigate wave–sea ice interactions in the Arctic marginal ice zone. In: *The Cryosphere* 14.2 (2020), pp. 709–735.

[60] Jim Thomson et al. Development and testing of microSWIFT expendable wave buoys. In: *Coastal Engineering Journal* (2023), pp. 1–13.

[61] Alison L Kohout et al. Storm-induced sea-ice breakup and the implications for ice extent. In: *Nature* 509.7502 (2014), pp. 604–607.

[62] Takehiko Nose et al. Observation of wave propagation over 1,000 km into Antarctica winter pack ice. In: *Coastal Engineering Journal* (2023), pp. 1–17.

[63] Jean Rabault et al. Measurements of wave damping by a grease ice slick in Svalbard using off-the-shelf sensors and open-source electronics. In: *Journal of Glaciology* 63.238 (2017), pp. 372–381.

[64] Graig Sutherland and Jean Rabault. Observations of wave dispersion and attenuation in landfast ice. In: *Journal of Geophysical Research: Oceans* 121.3 (2016), pp. 1984–1997.

[65] Fabrice Ardhuin et al. Ice breakup controls dissipation of wind waves across southern ocean sea ice. In: *Geophysical Research Letters* 47.13 (2020), e2020GL087699.

[66] Fabrice Collard et al. Wind-Wave Attenuation in Arctic Sea Ice: A Discussion of Remote Sensing Capabilities. In: *Journal of Geophysical Research: Oceans* 127.7 (2022), e2022JC018654.

[67] Clarence O Collins III et al. In situ measurements of an energetic wave event in the Arctic marginal ice zone. In: *Geophysical Research Letters* 42.6 (2015), pp. 1863–1870.

[68] JE Stopa et al. Wave attenuation through an Arctic marginal ice zone on 12 October 2015: 1. Measurement of wave spectra and ice features from Sentinel 1A. In: *Journal of Geophysical Research: Oceans* 123.5 (2018), pp. 3619–3634.

[69] Fabrice Ardhuin et al. Measuring ocean waves in sea ice using SAR imagery: A quasi-deterministic approach evaluated with Sentinel-1 and in situ data. In: *Remote sensing of Environment* 189 (2017), pp. 211–222.

[70] Danièle Hauser et al. SWIM: The first spaceborne wave scatterometer. In: *IEEE Transactions on Geoscience and Remote Sensing* 55.5 (2017), pp. 3000–3014.

[71] Alejandro Egido and Walter H. F. Smith. Fully Focused SAR Altimetry: Theory and Applications. In: *IEEE Transactions on Geoscience and Remote Sensing* 55.1 (2017), pp. 392–406. DOI: 10.1109/TGRS.2016.2607122.

[72] S. Eastwood and T. Lavergne. *Product User Manual for Global Sea Ice Concentration, Edge, Type and Drift, Near Real Time Observations*. 1.4. EUMETSAT, OSI SAF. France, July 2014.

[73] R. Ezraty, F. Girard-Ardhuin, and J. Poille. *Sea Ice Drift In The Central Arctic Estimated From SeaWinds/QuikSCAT Backscatter Maps—User's Manual*. Version 2.2. CERSAT, IFREMER. France, Feb. 2007.

[74] A Malin Johansson and Anders Berg. Agreement and complementarity of sea ice drift products. In: *IEEE Journal of Selected Topics in Applied Earth Observations and Remote Sensing* 9.1 (2016), pp. 369–380.

[75] M Thomas, CA Geiger, and C Kambhamettu. High resolution (400 m) motion characterization of sea ice using ERS-1 SAR imagery. In: *Cold regions science and technology* 52.2 (2008), pp. 207–223.

[76] S Das Peddada and Robert McDevitt. Least average residual algorithm (LARA) for tracking the motion of arctic sea ice. In: *IEEE transactions on geoscience and remote sensing* 34.4 (1996), pp. 915–926.

[77] Morgan McGuire. An image registration technique for recovering rotation, scale and translation parameters. In: *NEC Res. Inst. Tech. Rep., TR* (1998), pp. 98–018.

[78] Nobuyuki Otsu et al. A threshold selection method from gray-level histograms. In: *Automatica* 11.285-296 (1975), pp. 23–27.

[79] H. Schyberg et al. *Arctic regional reanalysis on single levels from 1991 to present*. Copernicus Climate Change Service (C3S) Climate Data Store (CDS). DOI: 10.24381/cds.713858f6 (Accessed on 01-06-2023). 2020.

[80] Copernicus Marine. *Arctic Ocean Wave Analysis and Forecast, dataset-wam-arctic-1hr3km-be 202311*. DOI: 10.48670/mio-00002. URL: https://doi.org/10.48670/mio-00002.

[81] Jean Rabault et al. A dataset of direct observations of sea ice drift and waves in ice. In: *Scientific Data* 10.1 (2023), p. 251.

[82] Jean Rabault et al. An OpenMetBuoy dataset of Marginal Ice Zone dynamics collected around Svalbard in 2022 and 2023. In: *arXiv preprint arXiv:2409.04151* (2024).

A

Appendix 1

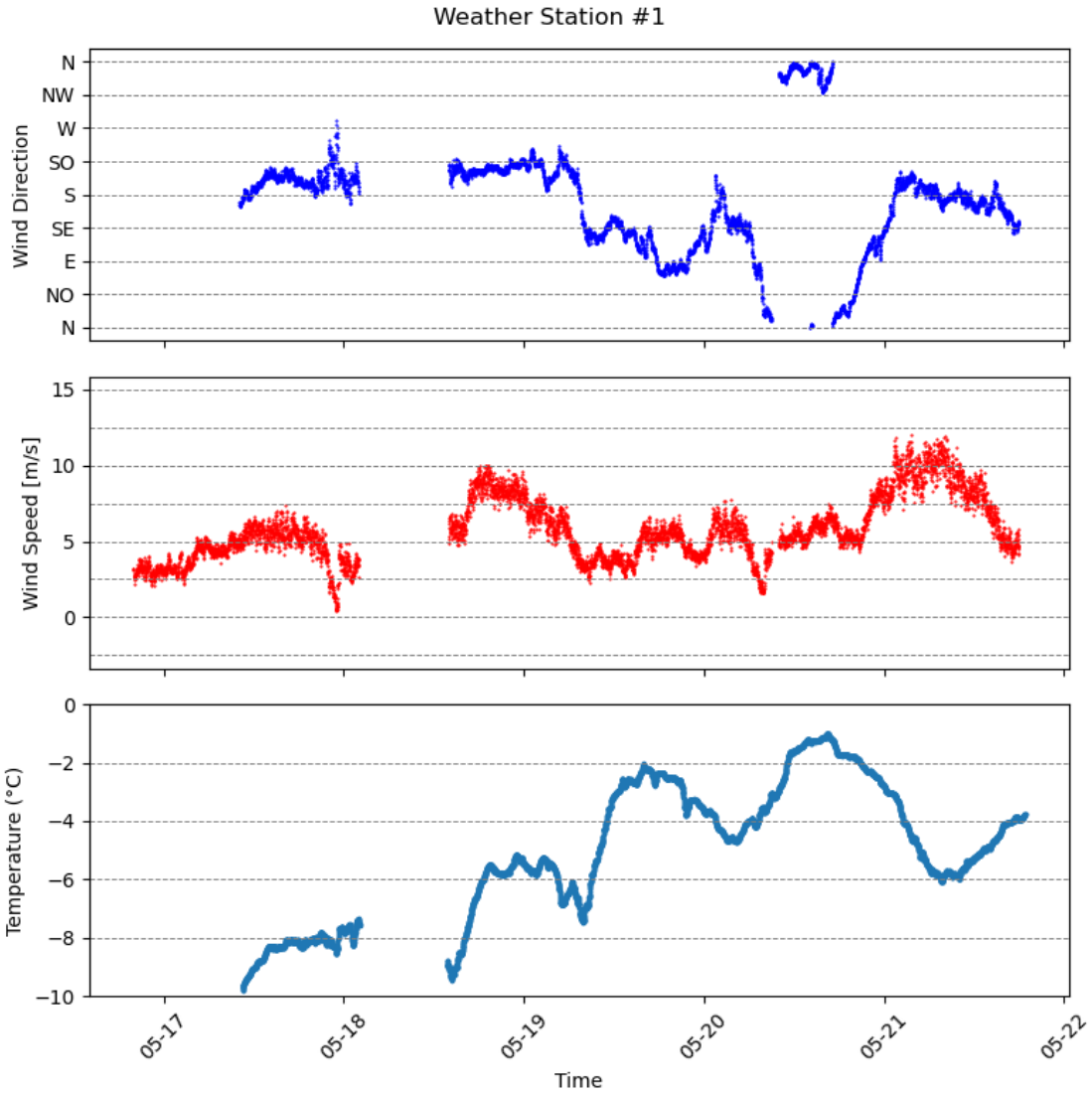

Figure A.1: Wind and temperature data from Weather Station n°1

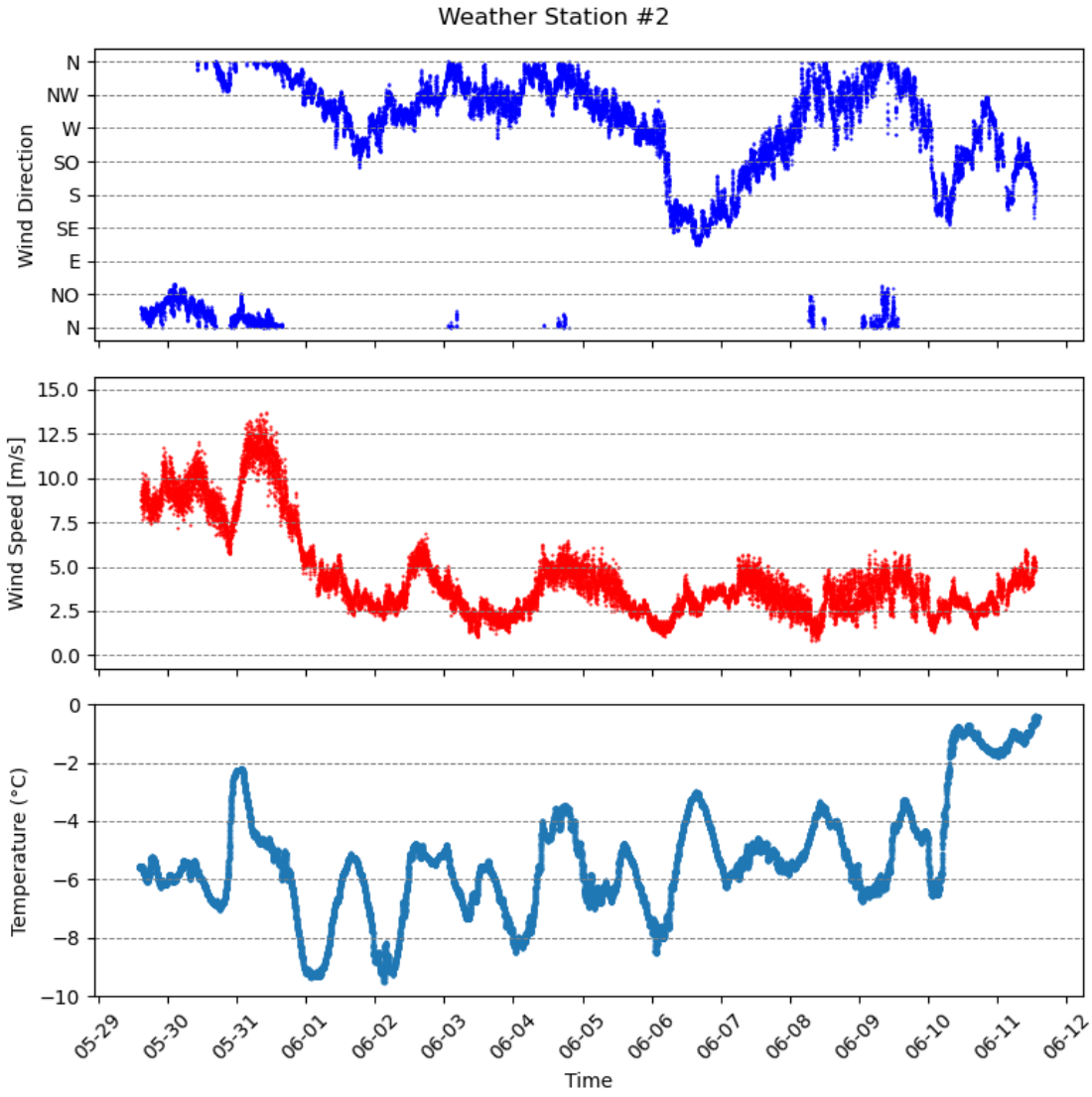

Figure A.2: Wind and temperature data from Weather Station n°2. The wind speed logger was connected before the temperature and wind direction loggers, thus explaining the missing data of these two on May 17^{th}

.

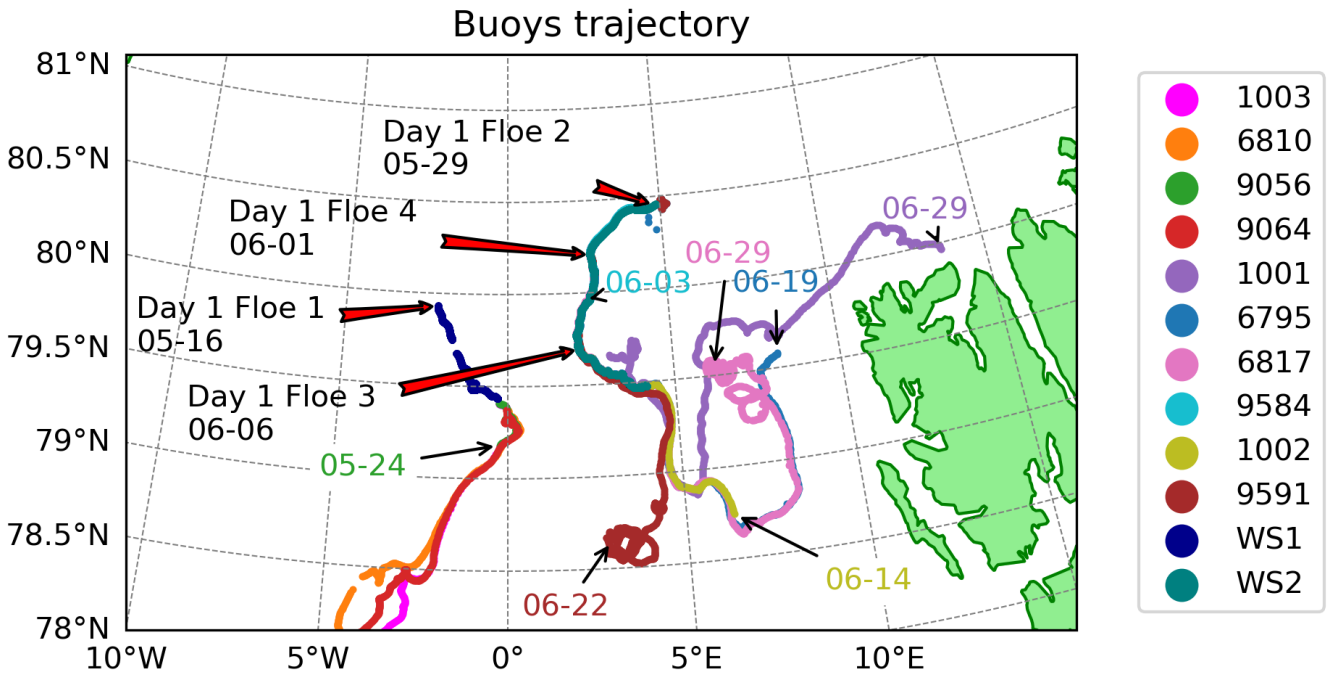

Figure A.3: Zoomed Extent

B

Appendix 2

B.1 Distance travelled daily by the buoys

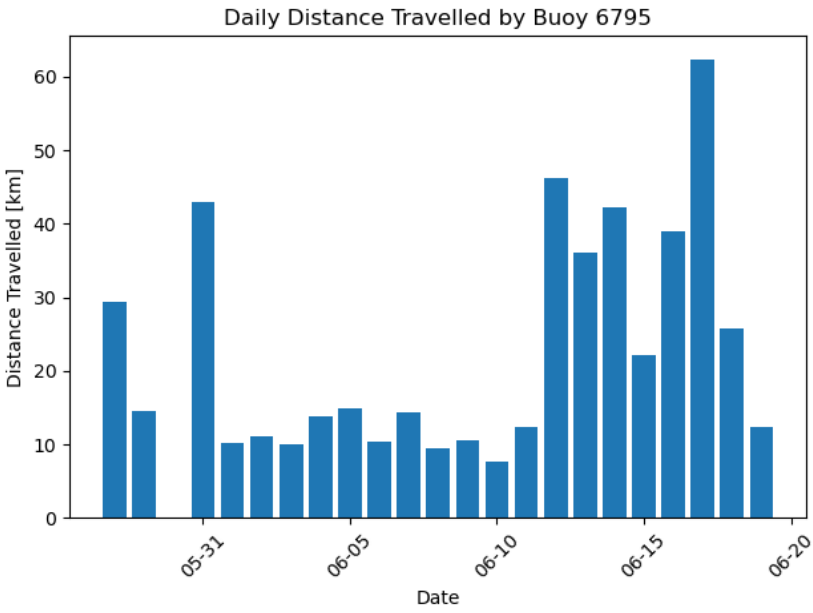

Figure B.1: Daily distance travelled by buoy 6795

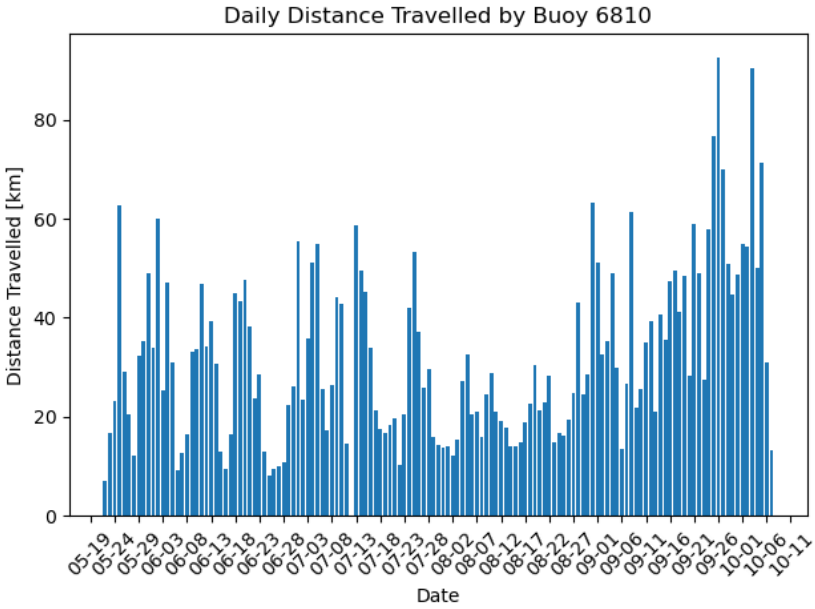

Figure B.2: Daily distance travelled by buoy 6810

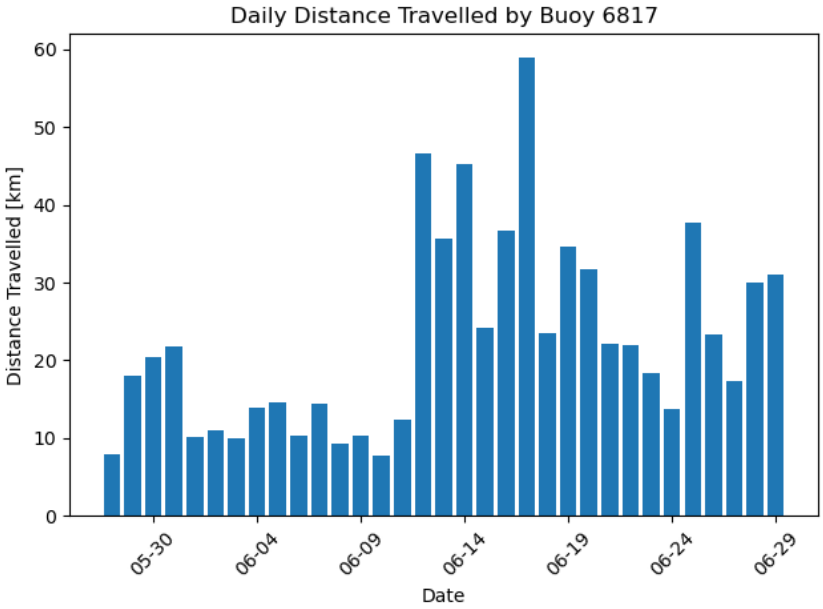

Figure B.3: Daily distance travelled by buoy 6817

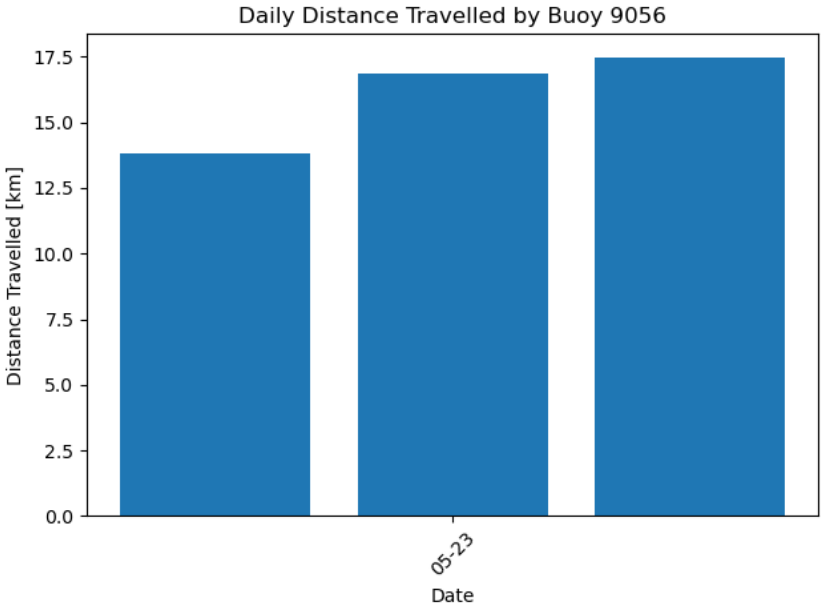

Figure B.4: Daily distance travelled by buoy 9056

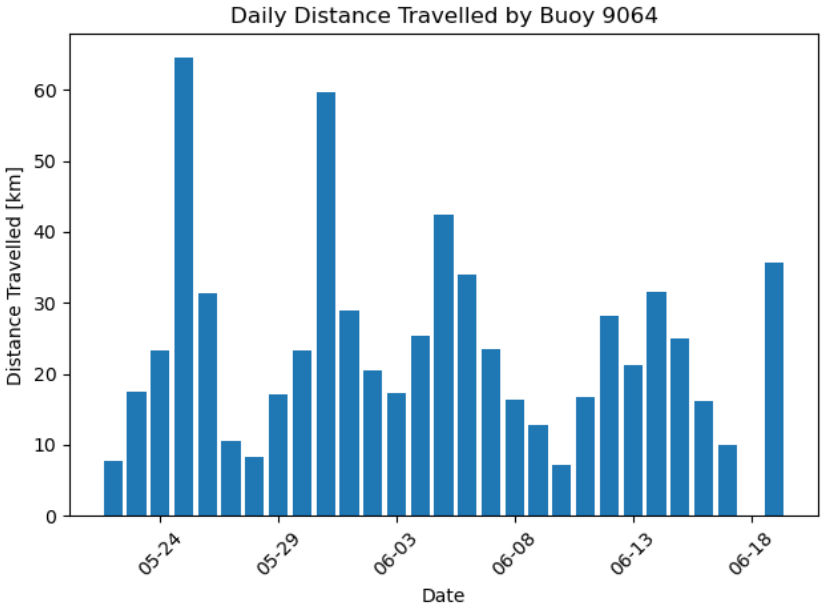

Figure B.5: Daily distance travelled by buoy 9064

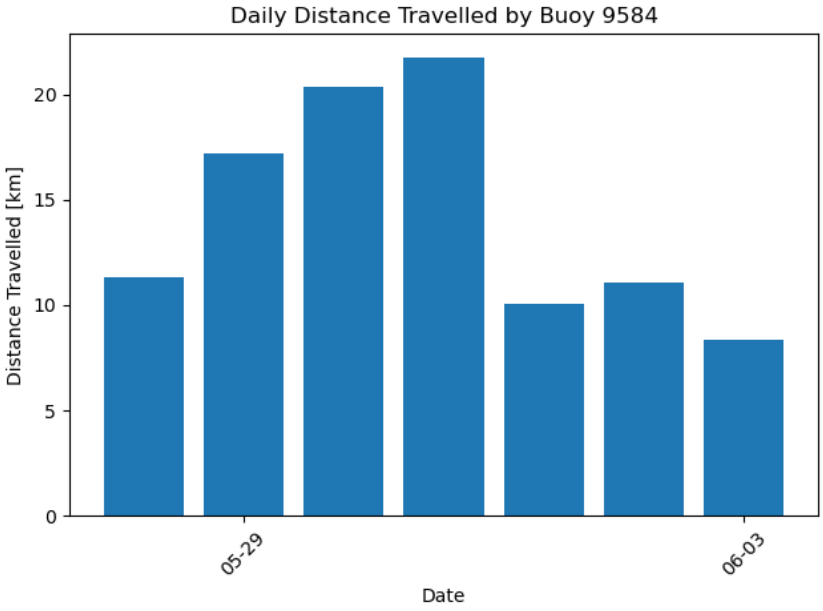

Figure B.6: Daily distance travelled by buoy 9584

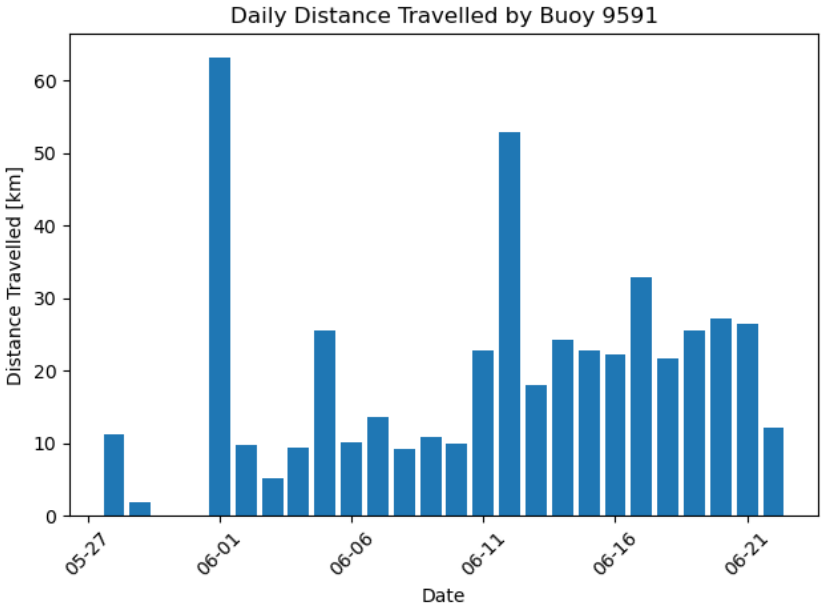

Figure B.7: Daily distance travelled by buoy 9591

C
Appendix 3

C.1 Waves Data - Floe 1

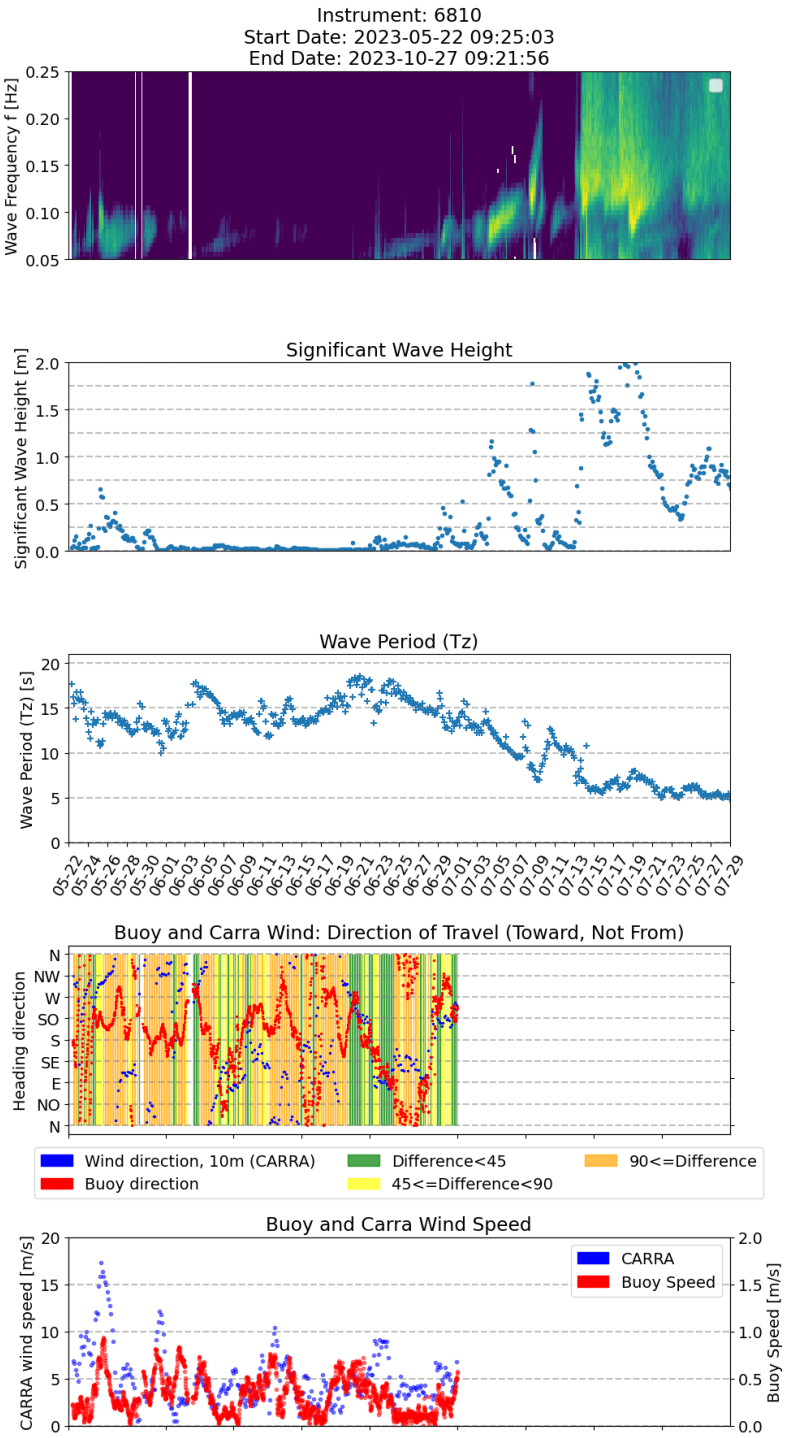

Figure C.1: Wave spectra of buoy 6810.

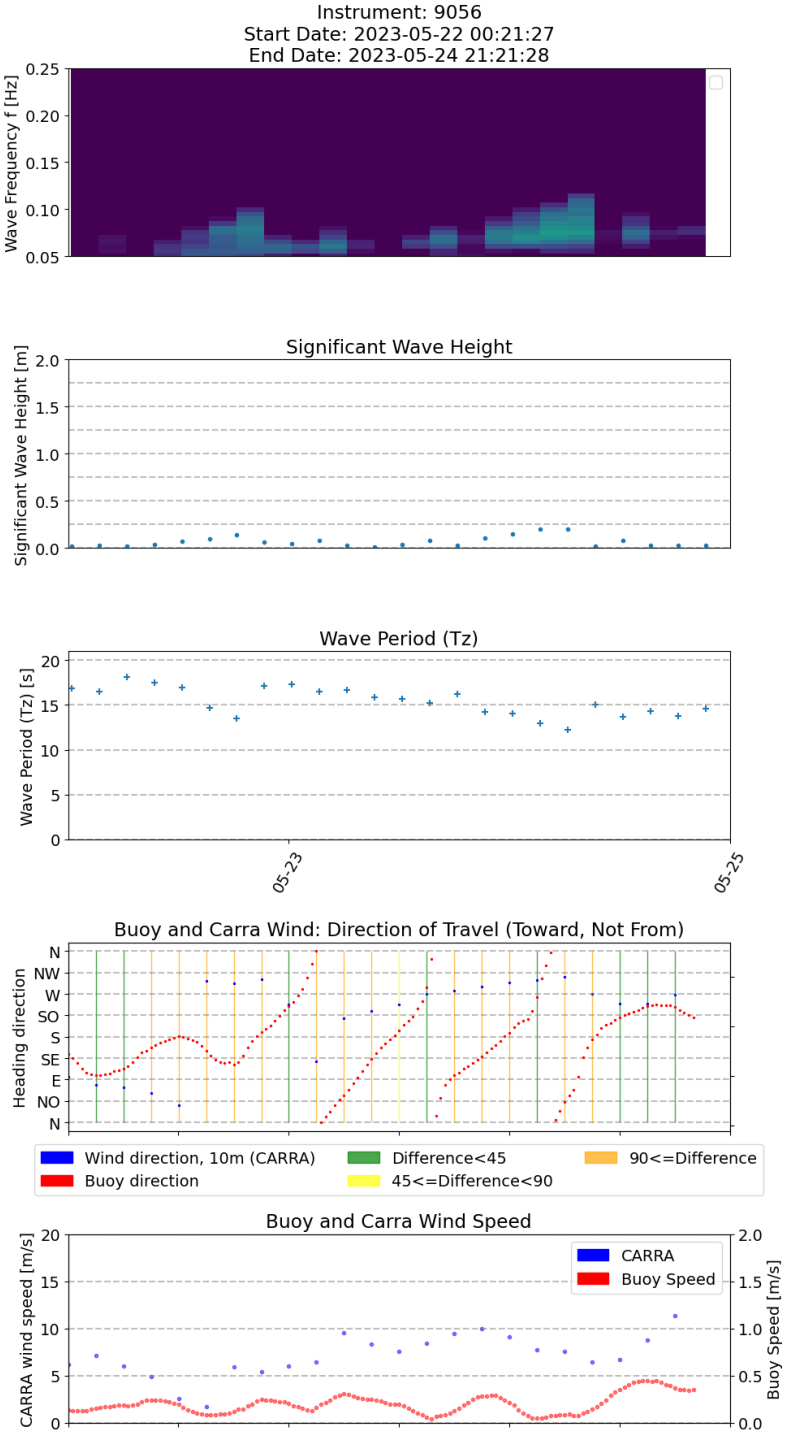

Figure C.2: Wave spectra of buoy 9056.

C.2 Waves Data - Floe 2

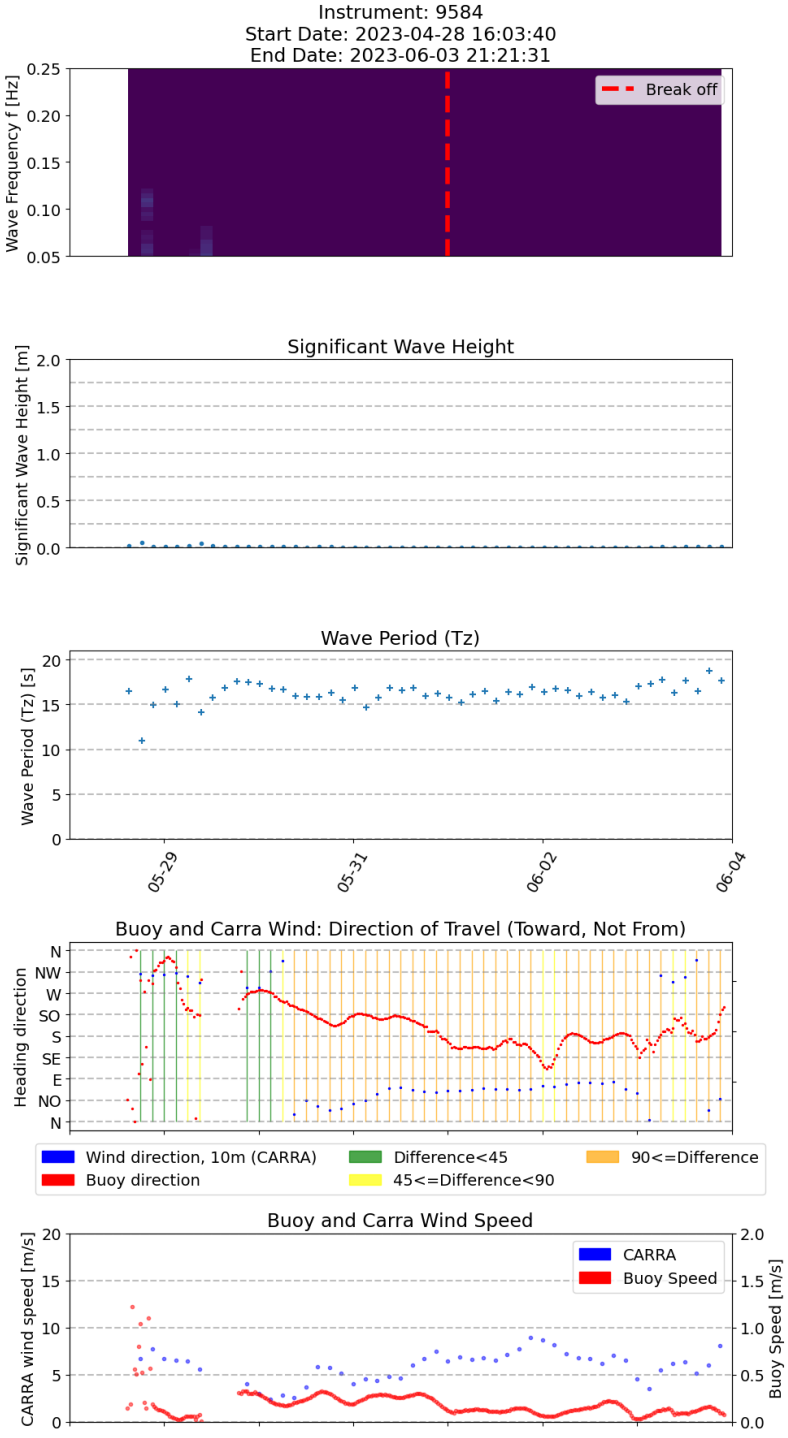

Figure C.3: Waves spectra of buoy 9584

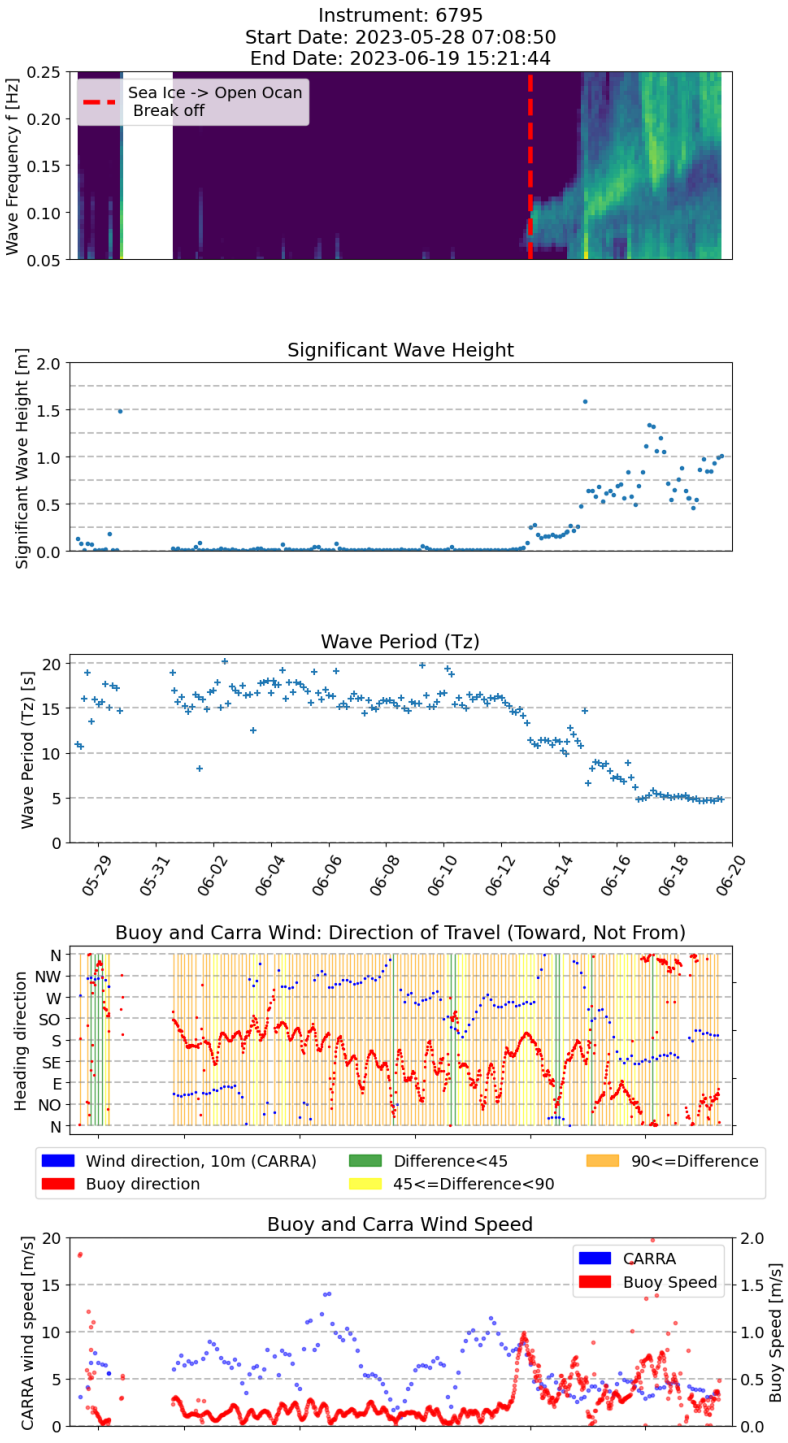

Figure C.4: Waves spectra of buoy 6795

C.3 Waves Data - Floe 4

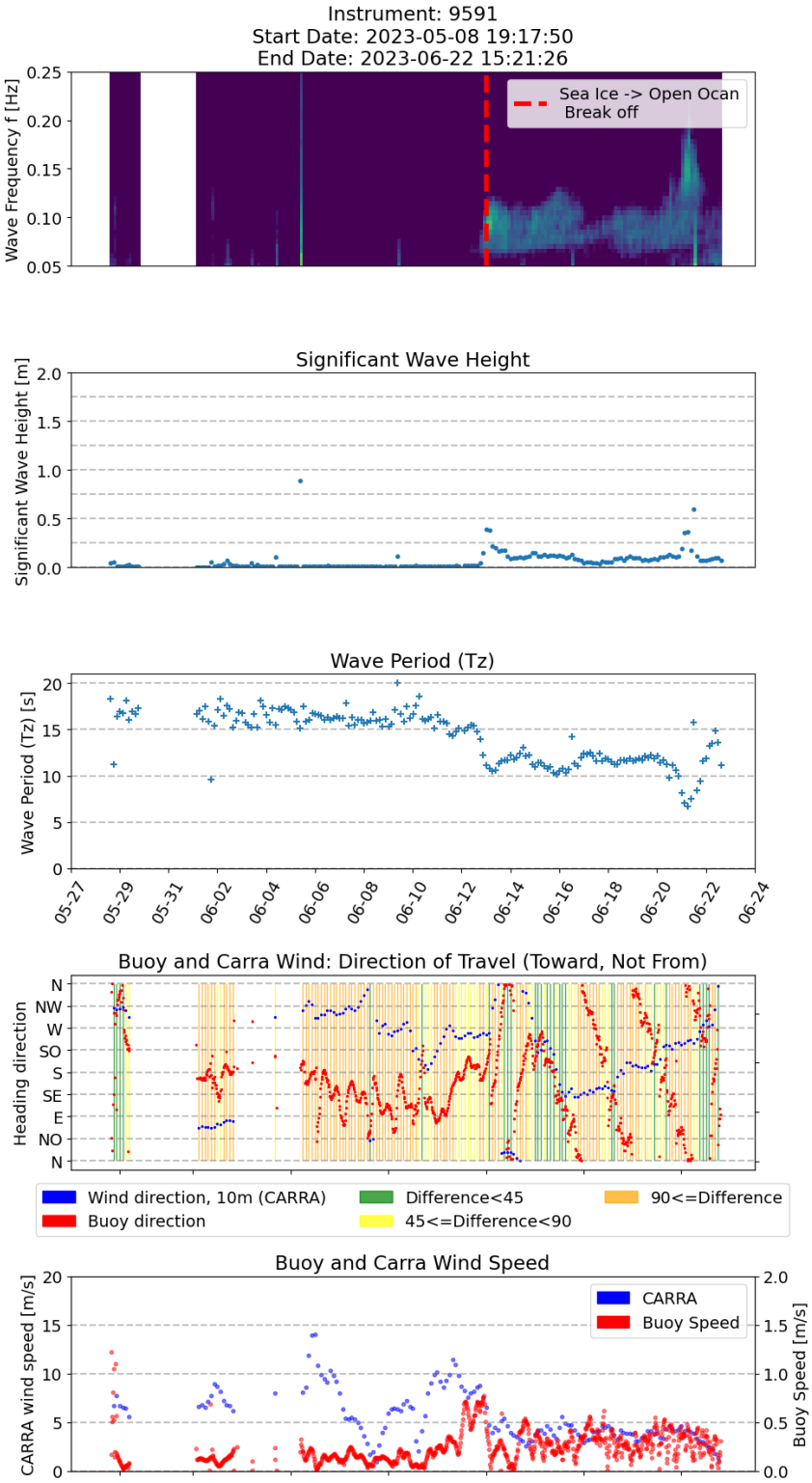

Figure C.5: Waves spectra of buoy 9591

D

Appendix 4

D.1 Chalmers algorithm - Statistics for Estimates No. 1 and 2

Table D.1: Comparison between the buoy drift and the estimated drift from the Chalmers algorithm between two RCM images (Estimate No.1: 2023-06-06 07:33:16 - 2023-06-06 16:02:53)

Buoy	**6795**	**6817**	**9591**
Distance travelled by the buoy [m]	3577	3543	3680
Azimuth of the buoy [°]	157	155	157
Closest drift vector			
Distance to the closest drift vector [m]	138	247	562
Drift distance of the closest drift vector [m]	3652	3644	3652
Difference between drift distance of the buoy and the vector [m]	75	101	29
Azimuth of the closest drift vector [°]	162	163	162
Difference between azimuth of the buoy and the vector [°]	5	8	5
Drift vector within 5 km radius			
Number of drift vectors	74	70	77
Mean drift distance [m]	4011	4016	3985
Standard deviation of drift distance [m]	281	290	250
Mean difference between drift distance of the buoy and the estimated drift distance [m]	434	472	326
Mean azimuth of vectors [°]	161	162	160
Standard deviation of azimuths [°]	2	1	3
Mean difference between buoy azimuth and estimates azimuths [m]	4	7	3

Table D.2: Comparison between the buoy drift and the estimated drift from the Chalmers algorithm between two RCM images (Estimate No.2: 2023-06-06 07:01:28 - 2023-06-06 16:02:53)

Buoy	**6795**	**6817**	**9591**
Distance travelled by the buoy [m]	3835	3796	3938
Azimuth of the buoy [°]	159	157	159
Closest drift vector			
Distance to the closest drift vector [m]	1922	2335	2950
Drift distance of the closest drift vector [m]	4487	4487	4487
Difference between drift distance of the buoy and the vector [m]	652	152	286
Azimuth of the closest drift vector [°]	163	163	163
Difference between azimuth of the buoy and the vector [°]	3	6	4
Drift vector within 5 km radius			
Number of drift vectors	40	37	21
Mean drift distance [m]	4508	4508	4504
Standard deviation of drift distance [m]	13	12	13
Mean difference between drift distance of the buoy and the estimated drift distance [m]	673	711	566
Mean azimuth of vectors [°]	162	162	163
Standard deviation of azimuths [°]	$1e^{-2}$	$1e^{-2}$	$1e^{-2}$
Mean difference between buoy azimuth and estimates azimuths [°]	3	6	4

DEPARTMENT OF SPACE, EARTH AND ENVIRONMENT
CHALMERS UNIVERSITY OF TECHNOLOGY
Gothenburg, Sweden
www.chalmers.se

CHALMERS
UNIVERSITY OF TECHNOLOGY